

August 2018

## Crystallographic Exploration of Fundamental Technetium Species at Nonambient Conditions

Daniel S. Mast  
daniel.mast@unlv.edu

Follow this and additional works at: <https://digitalscholarship.unlv.edu/thesesdissertations>

 Part of the [Condensed Matter Physics Commons](#), and the [Inorganic Chemistry Commons](#)

---

### Repository Citation

Mast, Daniel S., "Crystallographic Exploration of Fundamental Technetium Species at Nonambient Conditions" (2018). *UNLV Theses, Dissertations, Professional Papers, and Capstones*. 3368.  
<https://digitalscholarship.unlv.edu/thesesdissertations/3368>

This Dissertation is protected by copyright and/or related rights. It has been brought to you by Digital Scholarship@UNLV with permission from the rights-holder(s). You are free to use this Dissertation in any way that is permitted by the copyright and related rights legislation that applies to your use. For other uses you need to obtain permission from the rights-holder(s) directly, unless additional rights are indicated by a Creative Commons license in the record and/or on the work itself.

This Dissertation has been accepted for inclusion in UNLV Theses, Dissertations, Professional Papers, and Capstones by an authorized administrator of Digital Scholarship@UNLV. For more information, please contact [digitalscholarship@unlv.edu](mailto:digitalscholarship@unlv.edu).

CRYSTALLOGRAPHIC EXPLORATION OF FUNDAMENTAL TECHNETIUM SPECIES  
AT NONAMBIENT CONDITIONS

By

Daniel Steven Mast

Bachelor of Arts - Mathematics  
Bachelor of Science - Chemistry  
Saint Martin's University  
2013

A dissertation submitted in partial fulfillment  
of the requirements for the

Doctor of Philosophy – Radiochemistry

Department of Chemistry and Biochemistry  
College of Sciences  
The Graduate College

University of Nevada, Las Vegas

August 2018



## **Dissertation Approval**

The Graduate College  
The University of Nevada, Las Vegas

July 3, 2018

This dissertation prepared by

Daniel Steven Mast

entitled

Crystallographic Exploration of Fundamental Technetium Species at Nonambient Conditions

is approved in partial fulfillment of the requirements for the degree of

Doctor of Philosophy – Radiochemistry  
Department of Chemistry and Biochemistry

Paul Forster, Ph. D.  
*Examination Committee Chair*

Kathryn Hausbeck Korgan, Ph.D.  
*Graduate College Interim Dean*

Frederic Poineau, Ph. D.  
*Examination Committee Member*

Daniel Koury, Ph. D.  
*Examination Committee Member*

Barbara Lavina, Ph. D.  
*Examination Committee Member*

Pamela Burnley, Ph. D.  
*Graduate College Faculty Representative*

# Abstract

The study of matter under extreme conditions has yielded fascinating insight into the physical and chemical nature of materials that under more modest conditions are considered mundane but have quite unusual properties when under pressure. Examples of this are the lightest of elements found in the first two rows and in the heaviest elements of the lanthanide and actinide series. Pure elements, though the simplest possible chemical systems, have proven to be among the most complex and interesting. Technetium metal is a simple HCP transition metal that, due to its half-filled d-shell, has a rich chemistry and an important place at the turning point for periodic trends in the transition metals such as melting point, elastic moduli and strength.

The objective of my research is to understand the high pressure behavior of technetium metal and the two oxides,  $\text{TcO}_2$  and  $\text{Tc}_2\text{O}_7$ . The project is separated into three emphases: equation-of-state of elemental technetium, phase stability of transition metal oxides ( $\text{MO}_2$ ,  $\text{M} = \text{Tc, Re, Mo, W}$ ) and thermal motion of heptoxide species. Structural investigations are performed in diamond anvil cells (DACs) using synchrotron X-ray diffraction.

In the first portion, the goal is to define the ambient structure and the isothermal equation of state for technetium metal. This will be the basis for all other high pressure studies of technetium. The compression of technetium metal has been conducted using two pressure transmitting medium: MeOH-EtOH (67 GPa) and neon (153 GPa). In the second portion concerning the transition metal oxide, each dioxide was compressed. The compression data

revealed trends in the anisotropic compression behavior of the monoclinic phases. A novel phase of  $\text{MoO}_2$  in the  $\text{CaCl}_2$  structure type was observed while decompressing from 60 GPa. In the third portion of this work, single crystal X-ray diffraction experiments were conducted from 100K through 280K for  $\text{Tc}_2\text{O}_7$ . Unanticipated apparent contractions in bond lengths with increasing temperature were identified as being due to librational motion in the molecular solid, affecting both the terminal and the bridging oxygen atoms.

# Acknowledgments

This material is based upon work supported under an Integrated University Program Graduate Fellowship. This research was sponsored in part by the National Nuclear Security Administration under the Stewardship Science Academic Alliances program through DOE Cooperative Agreement #DE-NA0001982. Portions of this work were performed at HPCAT (Sector 16), Advanced Photon Source (APS), Argonne National Laboratory. HPCAT operations are supported by DOE-NNSA under Award no. DENA0001974 and DOE-BES under Award no. DE-FG02-99ER45775, with partial instrumentation funding by NSF. APS is supported by DOE-BES, under Contract no. DE-AC02-06CH11357. This research used resources of the Advanced Light Source, which is a DOE Office of Science User Facility under contract no. DE-AC02-05CH11231.

# Table of Contents

Abstract.....	iii
Acknowledgments.....	v
Table of Contents.....	vi
Table of Tables.....	x
Table of Figures.....	xi
Preface.....	xvi
<b>■</b> Introduction.....	1
<b>■</b> Technetium.....	1
<b>■</b> Discovery & Occurrence.....	1
<b>■</b> Technetium Chemistry/Tc in the Fuel Cycle.....	2
<b>■</b> Technetium Compounds.....	4
<b>■</b> Metals.....	5
<b>■</b> Transition Metal Dioxides.....	8
<b>■</b> Heptoxides.....	15
<b>■</b> High Pressure Generating Devices.....	16
<b>■</b> Equations of State.....	21

■	Conclusion.....	23
■	Methods.....	26
■	Synchrotron Facilities .....	26
■	Treatment of Synchrotron Data.....	26
■	Laboratory Single Crystal X-Ray Diffraction.....	28
■	Thermal Expansion of Technetium Metal .....	29
■	Introduction .....	29
■	Methods.....	31
■	Results & Discussion .....	32
■	Conclusion.....	36
■	Equation of state for technetium from X-ray diffraction and first-principle calculations <sup>103</sup> .....	37
■	Introduction .....	37
■	Methods.....	38
■	Results & Discussion .....	40
■	Conclusion.....	50
■	Equation of state of Technetium Metal up to 1.5 Mbar.....	51
■	Introduction .....	51



■	Methods .....	52
■	Results & Discussion .....	53
■	Conclusion.....	59
■	High Pressure Phase Diagram of Transition Metal Dioxides .....	61
■	Introduction of transition metal dioxides .....	61
■	Experimental Methods .....	62
■	Results & Discussion: .....	64
■	Molybdenum Dioxide .....	64
■	Rhenium Dioxide .....	70
■	Technetium Dioxide.....	77
■	Conclusion.....	79
■	An Atomistic Understanding of the Unexpectedly Low Volatility of the Molecular Oxide $Tc_2O_7$ 82	
■	Introduction .....	83
■	Methods .....	87
■	Results and Discussion.....	89
■	Conclusions .....	104

Conclusion .....	106
Appendix A.....	109
References.....	126
Curriculum Vita .....	141

# Table of Tables

<b>Table 1.</b> Metal-metal distances in transition metal dioxides.....	10
<b>Table 2.</b> Unit cell parameters for hcp technetium at ambient conditions. The sample analysed by Muller contained interstitial oxygen atoms.....	29
<b>Table 3.</b> Coefficients of thermal expansion .....	33
<b>Table 4.</b> Coefficient of thermal expansion of technetium metal. *A reference length of $L_0 = V_0/13$ , for $L = 323$ K was used for comparison. ....	36
<b>Table 5.</b> Summary of ambient pressure bulk moduli. The value determined by ultrasonic measurements is the adiabatic bulk modulus, $B_{us} = 2.81$ Mbar and is listed as the isothermal value. ....	38
<b>Table 6.</b> Summary of EoS parameters for experimental hydrostatic and nonhydrostatic pressure ranges, and the theoretical compression curve using the Vinet and Birch-Murnaghan equation of state with all parameters free and with the bulk modulus fixed at the ultrasonic result, $288 \text{ GPa}^{28}$ . ....	46
<b>Table 7.</b> Comparison of $B_0$ and $B'_0$ of technetium.....	48
<b>Table 8.</b> Vinet EOS Parameter summary .....	56
<b>Table 9.</b> Run 1 at 62 GPa the average difference in the measured d-spacing and calculated is 0.14%, which is 9 times greater than at 2 GPa. ....	58
<b>Table 10.</b> Run 2 at 92 GPa the average difference in the measured d-spacing and calculated is 0.11%, which is 6 times greater than at 0.8 GPa. ....	58
<b>Table 11.</b> Run 3 at 153 GPa the average difference in the measured d-spacing and calculated is 0.13%, which is 5 times greater than at 8 GPa. ....	58

<b>Table 12.</b> X-ray energies .....	64
<b>Table 13.</b> Equation of state parameter summary for monoclinic phases of the studied transition metal dioxides. The ranges used for fitting is indicated by low, high and full for individual data sets and the combined sets. Linear bulk moduli are indicated by subscripts of the respective axis. ....	80
<b>Table 14.</b> Bond lengths and angles for the bridging oxygen of $Tc_2O_7$ model in <i>Pbca</i> and <i>Pca2<sub>1</sub></i> . Standard uncertainties in last digit indicated by parenthesis. ....	95

## Table of Figures

<b>Figure 1.</b> $^{99}Tc$ decay scheme. <sup>162</sup> .....	2
<b>Figure 2.</b> Illustration of the three basic components of a diamond anvil cell: opposing anvils, a confining gasket, and the sample chamber. A beveled-anvil geometry is shown with the culet size A beveled to B at a bevel angle of $\theta$ . <sup>163</sup> .....	19
<b>Figure 3.</b> Three diamond/seal combinations are arranged starting from the left with two Diacell design diamond cuts paired with conventional WC and Be seats. <sup>76</sup> Then the conical diamond/seal pair is on the right. ....	20
<b>Figure 4.</b> One-hour XRD of technetium metal and magnesium oxide. ....	32
<b>Figure 5.</b> Thermal expansion of technetium metal as measured by percent change in length. The blue circles represent diffraction data reported in this work while the orange and black lines represent previously reported dilatometry and DFPT results. <sup>164</sup> .....	34

**Figure 6.** A representative series of diffraction patterns of technetium up to 67 GPa. Three low-angle peaks were contributed from the sample containment. .... 42

**Figure 7.** Pressure-volume data of Tc. a) A comparison of the Vinet equation of state of technetium up to 67 GPa with a fixed bulk modulus and refined. b) Comparison of compressibility from DFT calculations and experimentally determined EoS up to 300 GPa with the equation of state refined from hydrostatic and nonhydrostatic conditions extrapolated out to 300 GPa. Uncertainties are smaller than the symbol size c) Pressure difference between experimental pressure and the respective equations of state. Orange squares for fixed bulk modulus and red circles for the refined bulk modulus..... 43

**Figure 8.** Micro-stress in the technetium sample as a function of pressure, as determined following the procedure from Anzellini et al.<sup>23</sup> using the Young’s modulus determined by Love et al.<sup>28</sup>... 44

**Figure 9.** The bulk moduli of the transition metals are plotted with respect to their period as a function of d-electrons. Bulk moduli presented are from two computational studies looking at all of the transition metals with an unfilled d-shell.<sup>26,104</sup> ..... 49

**Figure 10.** Compression curves of technetium. Run 1, with a PTM of MeOH-EtOH is shown by blue circles; Run 2, with a PTM neon is shown in red circles; and Run 3, with a PTM of neon, is shown in green. .... 54

**Figure 11.** Axial ratio for the compression curves of technetium. Run 1, with a PTM of MeOH-EtOH is shown by blue circles; Run 2, with a PTM neon is shown in red circles; and Run 3, with a PTM of neon is shown in green. .... 55

**Figure 12.** Sample strain of technetium(red) and gold(blue) in Run 2 (circles) and Run 3 (squares). The percent difference between gold and technetium is shown in purple..... 57

<b>Figure 13.</b> Integrated X-ray diffraction pattern and Rietveld refinement of $\alpha$ -MoO <sub>2</sub> in a DAC at P =12.5 GPa. ....	64
<b>Figure 14.</b> Integrated X-ray diffraction patterns in the mixed phase region of MoO <sub>2</sub> .....	65
<b>Figure 15.</b> Integrated X-ray diffraction pattern and Rietveld refinement of the CaCl <sub>2</sub> phase of MoO <sub>2</sub> at P =18.7 GPa .....	66
<b>Figure 16.</b> Relative compression fraction for alpha (yellow) and beta (purple) MoO <sub>2</sub> . ....	67
<b>Figure 17.</b> Variation of lattice parameters of $\alpha$ -MoO <sub>2</sub> as a function of pressure for Run 1, triangles and Run 2, circles. The lattice parameter <i>a</i> is red, <i>b</i> is green and <i>c</i> is blue. ....	68
<b>Figure 18.</b> Relative lattice parameter variation as a function of pressure for MoO <sub>2</sub> . The unit cell directions are represented by blue, red and green circles for the <i>a</i> , <i>b</i> , and <i>c</i> , directions respectively. ....	69
<b>Figure 19.</b> Integrated X-ray diffraction pattern of alpha ReO <sub>2</sub> in DAC, P = 1.1 GPa. ....	71
<b>Figure 20.</b> The isothermal compression of $\alpha$ -ReO <sub>2</sub> from Run 1 (blue) and Run 2 (purple) .....	72
<b>Figure 21.</b> Relative lattice parameter variation of alpha ReO <sub>2</sub> for Run 1 (circles) and Run 2 (diamonds). Lattice parameter <i>a</i> is Red, <i>b</i> is green, and <i>c</i> is blue. ....	73
<b>Figure 22.</b> Integrated X-ray diffraction pattern of ReO <sub>2</sub> in a DAC at P = 30.3 GPa after laser heating. The $\alpha$ -phase is indicated with an “o” and the $\beta$ -phase is indicated by an “*”. ....	74
<b>Figure 23.</b> The variation of lattice parameter for $\beta$ -ReO <sub>2</sub> . The red, green and blue circles represent the unit cell lengths <i>a</i> , <i>b</i> , and <i>c</i> , respectively. ....	75
<b>Figure 24.</b> Relative volume compression of $\alpha$ - and $\beta$ -ReO <sub>2</sub> . The blue and purple circles represent data for the $\alpha$ -phase from Runs 1 & 2. The gray circles represent $\beta$ -ReO <sub>2</sub> . ....	76
<b>Figure 25.</b> Integrated X-ray diffraction pattern of TcO <sub>2</sub> in DAC. P = 2.3 GPa .....	77

**Figure 26.** Pressure-volume data for the isothermal compression  $\text{TcO}_2$  in MeOH-EtOH. The 2<sup>nd</sup> order Birch-Murnaghan equation of state is plotted. .... 78

**Figure 27.** Lattice parameter variation of  $\text{TcO}_2$  as a function of pressure. The  $a$ -axis length is represented by squares,  $b$  by circles and  $c$  by triangles. .... 79

**Figure 28.** (a) Melting points of transition metal compounds with molecular structures and mass.<sup>71,165-170</sup> Molecular oxides are represented by red squares, fluorides by blue circles, and oxyhalides by green diamonds. This table is limited to molecular solids where the nearest intermolecular distance is at least 40% greater than the average bond lengths found within the molecular species and where only weak additional van der Waals interactions such quadrupole-quadrupole interactions should exist. (b) Vapor pressure of transition metal compounds with molecular structures.<sup>70,139,141,167-181</sup> The extended structure of  $\text{Re}_2\text{O}_7$  creates a lower limit for the expected vapor pressure of  $\text{Tc}_2\text{O}_7$ . .... 86

**Figure 29.** Variation of lattice parameters with temperature. Error bars are smaller than data points. .... 90

**Figure 30.** Bond length variation of the metal to the bridging oxygen (top) and terminal oxygen atoms (bottom). Error bars represent standard uncertainty in SCXRD refinement. .... 91

**Figure 31.** Representation of correlated thermal motion which causes the apparent reduction in bond length. Recreated based off the work of Evans *et al.*<sup>155</sup> .... 92

**Figure 32.** TLS corrected bond lengths (squares) plotted with the SCXRD measured bond lengths (circles) for Tc-O distances. The solid lines are fits of the corrected data and dashed lines fits of the measured values. .... 94

**Figure 33.** Bond length variation in  $\text{Tc}_2\text{O}_7$  for a single MD snapshot and a 10-picosecond average. The temperature is the average temperature during the NpH simulation. .... 97

**Figure 34.** Snapshot of MD simulations every 150 fs at 50 K (a, b, c) and at 600 K (d, e, f). The bridging oxygen of the top right hand molecule for the 600 K series is highlighted to demonstrate transverse motion that develops at higher temperatures. .... 99

**Figure 35.** Partial radial distribution function for Tc-Tc. The first peak is identified as the intramolecular distances..... 101

**Figure 36.** Thermal expansion along each axis from molecular dynamics. Insets of the crystal packing along the respective axis. The [100] and [010] direction increase linearly over the samples temperature range. The [010] does not increase linearly and can roughly be fit by two linear regions with a discontinuity at 320 K. .... 102

**Figure 37.** Increasing molecular volume. Red squares represent SCXRD while blue circles represent MD results. The maximum increase observed from SCXRD at 280 K is 3.9%. For MD results going up to 600 K the molecular volume increased by 7.7%..... 103



# Preface

The elements of the periodic table form the building blocks of the chemical world. Testing the response of bulk material to external stimuli is the hallmark of early scientific exploration, i.e. flame test. One method of characterizing solid materials was developed by the work of the father and son pair, Sir William Henry and William Lawrence Bragg. Their work led to the identification of periodic lattices in crystalline solids and the subsequent ability to determine crystal structures. They were awarded the 1915 Nobel Prize in Physics for the analysis of crystal structures by means of X-ray diffraction. The capability to observe the structure of solids then enabled the investigation of structural responses to external stimuli. The effects of pressure and temperature on the volume or density of a closed system were well understood for gases and liquids, but the responses of solids were considerably less well understood. This being due to the need to look beyond physical dimensions to understand the materials response of solids. With the creation of the opposed anvil pressure device by Bridgman in 1946 and followed by the development of diamond anvil cell technology by the group at the National Bureau of Standards the idea of making *in situ* measurements of structure and materials properties at extreme conditions became a reality.

Experimentally determining the compressibility of materials, especially the elements, represented the most important initial avenues of research at high pressure. Compressibility is now routinely measured on new materials by collecting a series of diffraction images at several pressures along an isotherm, producing a set of pressure-volume data that are fit to an equation-of-state. It was quickly discovered that a single mathematical form for the equation of state for solids was not sufficient to describe all solids, nor was it possible to derive an equation from theory. In 1986

Hayward<sup>1</sup> emphasized that ‘*Many attempts have been made to derive a compressibility equation from molecular theory, but none of them has resulted in a convenient equation expressing the results of experiments with adequate accuracy. To meet this need it is necessary to employ some empirical equation, the sole justification for which is that it works*’—and this position remains unchanged to this day.

Since the inception of utilizing the diamond-anvil cell for the study of high-pressure physics and materials under extreme conditions, several elements have gone unstudied due to significant technical obstacles and safety concerns. Fluorine is exceptionally reactive in its elemental form. It is impractical to load elemental fluorine as a liquid or gas. Attempts to produce elemental fluorine *in situ* by chemical reactions provide a promising approach towards observing fluorine at high pressures. All of the other elements that lack an experimental determination of their compressibility are radioactive with alpha decay being the primary decay mode for a majority of the nuclides. Some, such as francium and astatine, are sufficiently rare as to have never been observed in the condensed state. Even if a sufficient quantity of these elements were available, the combination of short very half-lives and the large amount of heat produced from the decay would likely vaporize the solid material. Radon is a radioactive gas that has not been observed in the solid state. High pressure measurements of the condensed forms of liquids and gaseous starting material occur frequently. The difficulty with these materials is in preventing radioactive contamination and obtaining a sufficiently high purity sample. Radium, polonium, and actinium are also difficult to obtain due to reactivity and radioactivity. The effects of radiolysis on chemical bonds and self-heating would contribute additional technical difficulty in performing measurements on solids of most these materials.

While the radioelement technetium has no stable isotopes, the long half-life of available  $^{99}\text{Tc}$  allows it to be studied as a solid. Technetium is a long-lived beta emitter that does not present as large of a safety hazard as the short-lived alpha emitters or gases. Technetium is a solid at ambient conditions and chemically stable. Of the remaining elements without high pressure structural data, technetium is the most feasible for us to investigate at high pressure. There are a limited number of high-pressure studies have been conducted on technetium metal and technetium compounds that will be discussed in the following chapters.

The elements represent the ultimate collection for chemist. An extension of that collection is knowing how each behaves and fits within the trends that define the periodic table. The structure and the bulk modulus are two such examples of physical properties of solids where the community is close to completing our collection.

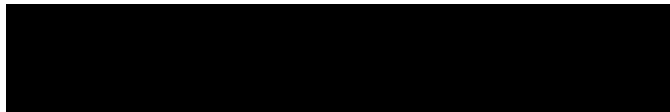
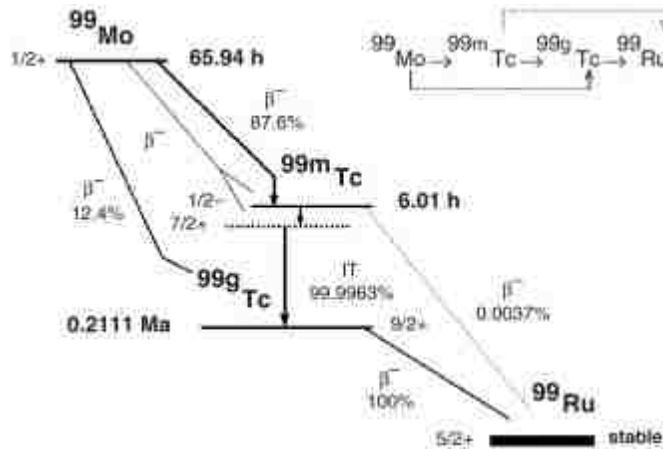
# Introduction

## Technetium

### Discovery & Occurrence

Although predicted to exist as ekamanganese by Mendeleev in 1869<sup>2</sup>, element 43 eluded chemist for many years. In 1937, Carlo Perrier and Emilio Segrè<sup>3,4</sup> isolated it from a radioactive molybdenum plate that had been acquired from Lawrence Ernest in Berkeley, California. The molybdenum metal plate had been used as a beam stop at the Berkeley Cyclotron. After a series of complex chemical separations to remove zirconium and molybdenum, it was concluded that the only remaining radioactivity species must be element 43. In 1946, element 43 was named after the Greek word for artificial, τεχνητόζ.<sup>5</sup> Now, thirty-five isotopes of technetium are known ranging from <sup>85</sup>Tc-<sup>120</sup>Tc.<sup>6</sup> The longest lived isotopes are <sup>98</sup>Tc ( $t_{1/2} = 4,200,000$  years), <sup>97</sup>Tc ( $t_{1/2} = 2,600,000$  years) and <sup>99</sup>Tc ( $t_{1/2} = 213,000$  years). Given that the half-lives are on the order of at most several millions of years; any primordial technetium present at the formation of the solar system has decayed away. There is, however, a rare natural sources of technetium. <sup>99</sup>Tc is a major fission product; it is expected to be found in uranium ore from the spontaneous fission of <sup>238</sup>U. <sup>99</sup>Mo is directly produced in fission and under goes beta decay with a 65.976-hour half-life to <sup>99m</sup>Tc. The meta stable nuclide <sup>99m</sup>Tc, subsequently decays to the ground state by emitting a 140.51 keV gamma with a 6.0058-hour half-life. One of the earliest identifications of naturally occurring technetium was via the separation of 1 pg of <sup>99</sup>Tc from 3.3 kg of pitchblende by Kenna and Kuroda in 1961. It was found later that up to 59 pg/Kg of technetium can be found in uranium ore. While

naturally occurring sources of technetium will never yield usable quantities of technetium, the element can be produced in an accelerator or nuclear reactor. After the dawning of the nuclear age,  $^{99}\text{Tc}$  has become available to research facilities on the gram scale.  $^{99}\text{Tc}$  is a pure beta emitter with an emission energy of  $\beta_{max}^- = 293 \text{ keV}$ , that decays to stable  $^{99}\text{Ru}$  with a half-life of 211,100 years.



## Technetium Chemistry/Tc in the Fuel Cycle

There are 99 licensed commercial nuclear power plants in the US, 65 pressurized water reactors and 34 boiling water reactors. In 2016, the US generated 805.3 billion kWh from nuclear power plants, approximately 19.7% of the total US electrical generation. This is the largest amount of energy produced by nuclear fission in the world.<sup>7</sup> In 2009, the Congressional Research Service reported that there is approximately 63,000 MT of spent fuel in the US with up to 2,400 metric tons added to the spent fuel storage annually. At typical burnup rates, approximately 1 kg of  $^{99}\text{Tc}$  is produced for one metric ton of uranium fuel.<sup>8</sup> In spent nuclear fuel, technetium can be found primarily in the uranium oxide matrix or in the “epsilon phase” The epsilon phase is a

heterogeneous metal alloy comprised of transition metals produced in fission including: Mo, Ru, Rh, Pd, and Tc. The separation occurring during the PUREX process leads to the oxidation of technetium to form the anionic species pertechnetate,  $\text{TcO}_4^-$ . In this form the technetium is very mobile in aqueous environments and presents a challenge for storage. At this time there are several proposed waste forms for the long term storage of technetium including metallic alloys, oxides, salt and glass composites. One of the principal areas of interest within technetium chemistry is developing a technetium waste form and predicting its long term behavior in various storage environments.

There are two stable oxides of technetium and they are both found at different stages of the nuclear fuel cycle. The dioxide can be formed after fission in oxide fuels and the heptoxide is a volatile species that is produced during vitrification of nuclear waste. An ideal waste form would be a technetium rich material that is chemically stable under a wide range of storage conditions. The ideal waste form would also be simple and inexpensive to make. There is a potential for stored material to be exposed to water, oxidizing/reducing conditions, corrosive materials over time. The chemical species of technetium stored needs to be able to withstand these conditions for hundreds of thousands of years without leaking material. Given the 213,000-year half-life, it will take 2 million years for the activity from today's technetium waste to decay to 0.2% of its original amount. Some proposed compounds that may be used as a technetium waste form include a metal alloy,  $\text{TcO}_2$ , and spinel or perovskites containing technetium.

# ■ Technetium Compounds

Cotton and Wilkinson<sup>9</sup> expanded on the IUPAC definition of transition metals which includes only elements with partially filled *d*-shells. Their definition explicitly includes scandium and yttrium which meet this criterion in the metallic state while excluding lanthanum and actinium as they are more appropriately classified as a subgroup of the transition metals known as the “inner transition metals” or the lanthanide and actinide series. In this work, the focus is on the behavior of Group 7 elements: manganese, technetium, and rhenium, within the context of periodic trends across the *d*-block. The electronic configuration of technetium is  $[\text{Kr}]4d^55s^2$ , the Group 7 elements are characterized by a full *s*-shell and half-filled *d*-shell. The known accessible oxidation states range from -1 to +7. Examples of rhenium and manganese exist for oxidation states up to -3, suggesting this should be achievable for technetium also. For technetium, the most stable oxidation states are +7 and +4. For manganese most stable are +7, +4 and then +2. The most stable for rhenium are +7, +6, and +4.

The metal-oxygen system represents some of the most fundamental compounds of an element, the binary oxides. In Group 7, there are oxides spanning a wide range of stoichiometries and crystal structures. Manganese has seven stoichiometric oxides:  $\text{MnO}$ ,  $\text{MnO}_2$ ,  $\text{Mn}_2\text{O}_3$ ,  $\text{Mn}_3\text{O}_4$ ,  $\text{Mn}_2\text{O}_7$ , and  $\text{Mn}_5\text{O}_8$ . Four rhenium oxides exist:  $\text{ReO}_2$ ,  $\text{ReO}_3$ ,  $\text{Re}_2\text{O}_7$ , and  $\text{Re}_3\text{O}_{10}$ . Nonstoichiometric compositions are known for several of the oxides in the lower oxidation states. Two known technetium oxides have been characterized in the solid state,  $\text{TcO}_2$  and  $\text{Tc}_2\text{O}_7$ . Evidence of additional binary oxide species have been reported in the gas phase including  $\text{Tc}_2\text{O}_5$  and  $\text{TcO}_3^{10-}$ <sup>12</sup>. Since both of these technetium oxides are present throughout the nuclear fuel cycle, it is

important to understand their physical and chemical behavior in order to design safe and reliable processes.

In each of the oxidation states (0, +4, +7) that technetium is likely to form a solid oxide or metal, there is a nonradioactive homolog that can be investigated. For many technetium species, the most chemically similar compound is a rhenium homolog where as it is rare for manganese to form a suitable homolog. This is the case for metallic technetium. Both technetium and rhenium form hexagonal metals with similar properties while manganese has a cubic structure and is much softer. Of the three dioxides that exist with Group 7 metals,  $\text{ReO}_2$  and  $\text{TcO}_2$ , crystallize in the same structure-type while  $\text{MnO}_2$  does not. However, molybdenum and tungsten are also known to share the same structure form as  $\text{TcO}_2$ . Binary metal heptoxides are only formed by Group 7 elements and each member of the group has a unique crystal structure. The lighter two metals form molecular solids while  $\text{Re}_2\text{O}_7$  crystallizes in an extended structure that can be approximated as a molecular species if two sets of bonds are disregarded. These three structures are unique to these materials. The closest related compounds are other transition metal molecular solids and ternary oxides that have the  $\text{M}_2\text{O}_7$  motif within their extended structure. The nonradioactive homologs provide a valuable opportunity to first work with a more accessible material as well as provide a broader context for studies of technetium.

## Metals

The transition metals predominantly crystallize as solids exhibiting high packing efficiency. Of the group 7 metals, technetium and rhenium both crystallize in a hexagonal close packed (HCP) lattice of the space group  $\text{P6}_3/\text{mmc}$ . These are high density solids (about  $11.5 \text{ g/cm}^3$ ,  $21.0 \text{ g/cm}^3$ ,



respectively) where the metal takes on a silver/gray color when machined as a foil or wire. The powder or polycrystalline aggregates appears as a dark gray or black color. The average of the reported ambient structure lattice parameters for technetium are  $a = 2.7409(5) \text{ \AA}$  and  $c = 4.3987(34) \text{ \AA}$  and  $a = 2.761 \text{ \AA}$  and  $c = 4.456 \text{ \AA}$  for rhenium.<sup>13,14</sup> Each metal is known to be stable in the hexagonal phase up to their melting points, 2430(30) K and 3453 K. The properties and structure of technetium remain mostly unexplored at non-ambient conditions while rhenium has been repeatedly compressed to the highest pressures achievable under static conditions.

In 1955, using an opposed anvil geometry, Bridgman observed the resistance and shear characteristics of technetium up to 10 GPa and found the hcp phase stable with no irregularities.<sup>15</sup> The hexagonal structure of rhenium has been confirmed up to 6 Mbar.<sup>16</sup> A discrepancy of three orders of magnitude in the pressure ranges explored for technetium and rhenium best exemplifies our lack of understanding of the high pressure behavior of technetium. At present, the phase diagrams of these metals consist of one single solid phase. A cubic structure of each metal has been suggested, but the reports do not indicate a reliable method for preparing phase pure samples appropriate for further characterization or study at non-ambient conditions. The melting temperature of a solid is typically elevated with the application of pressure although the magnitude of the variation is known to vary widely across the periodic table. The melting curve of rhenium was most recently determined by a flash heating method to increase from 3453 K to above 4000 K at 47 GPa.<sup>17</sup> The melting behavior of technetium has only been measured at ambient pressure.

Many thermodynamic quantities have been determined for these metals. The bulk modulus of rhenium has been determined multiple times with values ranging from 350 to 376 GPa and pressure derivative from 2.4 to 5.4.<sup>16,18-23</sup> While this is a considerably larger range of values than is

appropriate for a material that has been suggested for use as an *in situ* pressure calibrant, it is clear that rhenium is a relatively incompressible element. With a lack of high pressure structural data for technetium, there are no experimental equations-of-state for technetium. There have been several reports which determined the ambient pressure bulk modulus computationally.<sup>24–27</sup> The bulk modulus of technetium at ambient pressure has been determined from ultrasonic measurement as being,  $B_0 = 288$  GPa.<sup>28</sup> To a lesser degree than rhenium, technetium is an incompressible metal.

Technetium has always attracted attention as it has the second highest superconducting transition temperature for an element (7.4 K).<sup>29</sup> Solid solution alloys of technetium with the HCP structure have superconducting transitions of ranging from 1.77 K to 11.68 K for 60% ruthenium and 5% niobium, respectively.<sup>30</sup> Technetium, along with niobium and vanadium, are all elemental Type II superconductors.<sup>31</sup> The superconducting transition temperature for technetium smoothly decreases through 1.5 GPa (the maximum pressure measured experimentally) at a rate of  $-1.25(5) \times 10^{-1}$  K/GPa.<sup>32</sup> For rhenium, it is a curiosity that the effect of pressure is to lower the transition temperature and, upon reaching a minimum at 0.7 GPa, it then increases before plateauing between 1.3–1.8 GPa.<sup>33</sup> The investigation into the superconducting behavior of technetium has not been taken to sufficiently high pressures to determine if the superconducting transition can be squashed completely or if it reaches a minimum like rhenium.

An even more unique property of technetium is the effect of pressure on the rate of radioactive decay. For years it has been assumed that nuclear decay is invariant but at least three groups have challenged this belief by showing that the decay constant of  $^{99m}\text{Tc}$  can decrease by 0.023–0.046% at 10 GPa.<sup>34–36</sup> While equipment is now available to extend this study to higher pressures, the effect of pressure on the decay rate is small and no potential applications have made use of this

since the time that proof has been presented that it is possible. The change in decay rate is possible in this instance because the relaxation from  $^{99m}\text{Tc}$  to  $^{99}\text{Tc}$  is by internal conversion 99.996% of the time. Internal conversion is the transfer of energy from the nucleus to an atomic electron. This electron is ionized and then the empty shell is filled by another atomic electron, releasing an X-ray. De-excitation of the nucleus, radioactive decay, through internal conversion does not alter the composition of the nucleus. Since internal conversion is a process that takes place outside of the nucleus it is susceptible to the effects of external stimuli, like pressure.

For laboratory use, technetium is acquired as ammonium pertechnetate which is produced from the decay of  $[\text{}^{99}\text{MoO}_4]^{2-}$ . The metal can be prepared from the pertechnetate form by hydrogen reduction.

## Transition Metal Dioxides

Most transition metals (23 out of 30) form dioxides, as do a number of other non-transition metals. Fifteen of the dioxides have one or more polymorph with the rutile structure-type or a derivative of the rutile structure-type. Within the rutile-based structures, there are only four structure-types that these systems crystallize in at ambient conditions. Eleven transition metal dioxides and three non-transition metal dioxides crystallize in the space group  $P4_2/mnm$  which is known as the rutile structure type. The remaining structures can be described as distortions of the rutile structure-type. Transition metal dioxides have been extensively studied in recent years for their interesting physical properties associated with their electronic structure. Strong covalent bonds are formed between the metals and oxygen atoms due to the hybridization of the  $d$  and  $p$  orbitals contributed from the metal and oxygen atoms respectively.

The rutile structure of titanium dioxide consists of chains of symmetric edge-sharing octahedra that are connected by corner-sharing vertices. The metal-oxygen distances are 1.9808(10)Å and 1.9481(6)Å.<sup>37</sup> A large portion of the non-rutile structures, however, do not form symmetric octahedra and instead fall into a lower symmetry class. The degree of distortion has been described in a review looking at all of the topologically identical rutile-type structures.<sup>38</sup> It was found that some of those with the largest degree of distortion are found in the monoclinic crystal system with space group P2<sub>1</sub>/c. There are five compounds that take on the monoclinic structure, MO<sub>2</sub>, M = V, Mo, Tc, W, Re. In 1955, Magneli and Andersson first observed the MoO<sub>2</sub> structure-type, which describes the crystal structure of the dioxides of molybdenum, tungsten, vanadium, technetium and rhenium.<sup>39</sup> The nature of the octahedral distortion is such that the metal atoms along the chains of edge-sharing polyhedral occur in doublets with alternating metal-metal distances, **Table 1**. The metal-metal distance is correlated with the number of valence electrons and indicative of increasing metal-metal interactions. MoO<sub>2</sub> and those crystallizing in the MoO<sub>2</sub> structure-type were the first class of materials identified as having significant metal bonding characteristics. The nature of metal-metal bonding has drawn the attention of inorganic chemistry since Magneli's first description of this interaction.<sup>40</sup> It is common to probe metal-metal interactions by manipulating the chemical environment through changing the coordinated ligands to create different electronic/chemical environments for the metal-metal interaction to exist in. Complexes of molybdenum and tungsten has been identified as having quadruple metal-metal bonding with bond lengths as short as ~2.10 Å.<sup>41</sup>

**Table 1.** Metal-metal distances in transition metal dioxides

Compound	Valence electrons	Metal-Metal distance (Å)	References
TiO <sub>2</sub> (rutile)	4 + 0	2.9587	<sup>37</sup>
VO <sub>2</sub>	4 + 1	2.65, 3.12	<sup>42</sup>
MoO <sub>2</sub>	4 + 2	2.50, 3.20	<sup>43</sup>
WO <sub>2</sub>	4 + 2	2.49, 3.08	<sup>43</sup>
TcO <sub>2</sub>	4 + 3	2.48, 3.06	<sup>44</sup>
ReO <sub>2</sub>	4 + 3	2.49, 3.08	<sup>45</sup>

The behavior of the transition metal dioxide systems has in recent years generated new interest in the high pressure community. The energy landscape of transition metal dioxides is diverse as demonstrated by the large number of stable and meta-stable structures.

## ■ Molybdenum Dioxide

The MoO<sub>2</sub> phase reported by Magneli and Andersson in 1955 is in the monoclinic MoO<sub>2</sub> structure-type in the space group is P2<sub>1</sub>/c with lattice parameters of  $a = 5.584 \text{ \AA}$ ,  $b = 4.842 \text{ \AA}$ ,  $c = 5.608 \text{ \AA}$ , and  $\beta = 120.94^\circ$ .<sup>39</sup> A rutile phase of MoO<sub>2</sub> can be synthesized by the thermal decomposition of the methoxide complex MoO(OMe)<sub>4</sub>.<sup>46</sup> The lattice parameters for the rutile MoO<sub>2</sub> are  $a = 4.8473(3) \text{ \AA}$ ,  $c = 2.8136(3) \text{ \AA}$ . Five structures types have been calculated to be at most 0.2 eV less stable than the monoclinic phase, indicating that these are potential meta-stable phases accessible with pressure.<sup>47</sup> The potential meta-stable phase are SnO<sub>2</sub>-II, alpha-PbO<sub>2</sub>, alpha-MoS<sub>2</sub>, beta-MoS<sub>2</sub>, and rutile-TiO<sub>2</sub>. Both of the structure types of MoS<sub>2</sub> as well of the cotunnite, are predicted to be more

stable than  $\alpha$ -MoO<sub>2</sub> below 100 GPa while the orthorhombic phase of TiO<sub>2</sub> is found to be the most stable phase above about 25 GPa.<sup>47</sup>

A high pressure polymorph of MoO<sub>2</sub> was discovered at 18 GPa and 1073K.<sup>48</sup> The high pressure phases is in the orthorhombic crystal system in the space group *Pnma* with lattice parameters of  $a = 9.6921(3)$  Å,  $b = 8.4322(3)$  Å,  $c = 4.7188(2)$  Å. This structure type was previously reported as a high pressure phase of WO<sub>2</sub>.

Molybdenum dioxide has found uses in several reactions including the reduction of MoO<sub>3</sub> and in the production of metallic molybdenum. Atomic layers of MoO<sub>2</sub> have shown high electrocatalytic activity.<sup>49</sup> Molybdenum dioxide has electrochemical applications and has been shown to be a promising anode material for lithium ion batteries.<sup>50</sup> Nanoparticles of molybdenum dioxide has also been used for photothermal cancer therapy.<sup>51</sup>

## ■ Technetium Dioxide

The monoclinic phase is the only reported structure of technetium dioxide. No additional polymorphs have been reported at non-ambient conditions. The monoclinic phase is in the MoO<sub>2</sub> structure-type has lattice parameters of  $a = 5.6891(1)$  Å,  $b = 4.7546(1)$  Å,  $c = 5.5195(1)$  Å, and  $\beta = 121.453(1)^\circ$ . A meta-stable phase of TcO<sub>2</sub> has been predicted in the same space group with distorted TcO<sub>5</sub> hexadecahedrons.<sup>52</sup> Anomalous behavior of the lattice parameters is predicted at high pressure.<sup>53</sup> The compression of the [100] lattice spacing is predicted to decrease monotonically with pressure while the [001] lattice spacing is expected to increase in the range of 6 and 20 GPa while the [010] direction experiences a decrease up to 6 GPa, an increase from 6 – 20 GPa and then limited decrease up to 120 GPa. The  $\beta$  angle increase from  $\sim 121^\circ$  to saturate near  $\sim 123^\circ$ . TcO<sub>2</sub>

begins to sublime at 900 °C and will decompose into solid Tc metal and gaseous Tc<sub>2</sub>O<sub>7</sub> above 1100 °C.<sup>54</sup>

Ternary oxides, much like TcO<sub>2</sub>, are comprised of TcO<sub>6</sub> octahedra. The interaction between metal centers plays a significant role in the structure and properties of the dioxides and the degree of this interaction also impacts the properties of more complex systems. In Tc-based perovskites, like CaTcO<sub>3</sub> and SrTcO<sub>3</sub>, there is strong magnetism.

Technetium dioxide, being the most stable oxide of technetium, has received more attention for nuclear waste applications than Tc<sub>2</sub>O<sub>7</sub>. For instance, the oxidation of technetium metal was simulated in order to model the behavior of the technetium dioxide on the surface of the alloy systems with particular emphasis as to how the technetium oxide phase interactions with other alloy components.<sup>55</sup> Due to the similarities in structures, it has been proposed that a rutile TiO<sub>2</sub> matrix could be used to store or dispose of TcO<sub>2</sub> by transmutation using neutron irradiation. The solubility of RuO<sub>2</sub> and TcO<sub>2</sub> was determined to be between 14 - 18% for these materials at 1673 K. Ruthenium is less soluble than technetium even with the increased solubility of ruthenium at elevated temperatures.<sup>56</sup> In the laboratory TcO<sub>2</sub> is a common starting material for other synthesis routes of halides<sup>57</sup> and oxyhalides.<sup>58</sup>

## ■ Rhenium Dioxide

The  $\alpha$ -phase of rhenium dioxide is the MoO<sub>2</sub> structure-type with lattice parameters of  $a = 5.615(3)$  Å,  $b = 4.782(2)$  Å,  $c = 5.574(2)$  Å,  $\beta = 120.13(1)^\circ$ .<sup>45</sup> The  $\beta$ -ReO<sub>2</sub> is an orthorhombic phase in the alpha-PbO<sub>2</sub> structure type in the space group Pbcn with lattice parameters of  $a = 4.8094(5)$  Å,  $b = 5.6433(5)$  Å,  $c = 4.6007(5)$  Å.<sup>59</sup> The monoclinic  $\alpha$ -phase transforms completely into the

orthorhombic  $\beta$ -phase when heated above 300 °C.<sup>59</sup> The orthorhombic phase is stable up to at least 1050 °C and is recoverable to ambient conditions. The third phase, which we will refer to as the  $\gamma$ - $\text{ReO}_2$ , was obtained through a solid-state synthetic route by annealing a mixture of  $\text{NaReO}_4$  and  $\text{NH}_4\text{Cl}$  at 420 °C under argon for 4 hours.<sup>60</sup> This phase crystallizes in the rutile structure-type with lattice parameters of  $a = 4.79825(5) \text{ \AA}$  and  $c = 2.80770(4) \text{ \AA}$ .<sup>60</sup> The gamma and alpha phases have very similar energies with less than 0.02 eV difference while the beta phase is the more stable by about 0.38 eV at zero pressure.<sup>61</sup> The calculated bulk moduli of  $\text{ReO}_2$  are 345 GPa, 322 GPa, and 353 GPa for the monoclinic, orthorhombic and tetragonal phases respectively.<sup>61</sup>

Like molybdenum dioxide, rhenium dioxide has been used in electrochemical applications<sup>62</sup> as well as a catalyst for the dehydrogenation of alcohols,<sup>63</sup> and selective oxidation of hydrocarbon catalysts.<sup>64</sup> In the synthesis of the ceramic superconductor  $\text{Hg}_{1-x}\text{Re}_x \text{Ba}_2\text{Ca}_2\text{Cu}_3\text{O}_{8+\delta}$ ,  $\text{ReO}_2$  is used to limit the formation of  $\text{HgCaO}_2$  by reacting with  $\text{CaO}$  to form  $\text{Ca}_5\text{Re}_2\text{O}_{12}$ .<sup>65,66</sup>

## ■ Tungsten Dioxide

The three known phases of tungsten dioxides are the monoclinic phase in the  $\text{MoO}_2$  structure-type, the tetragonal phase in the rutile structure-type, and the high pressure phases in the space group  $Pnma$ . The tungsten dioxide phase in  $\text{MoO}_2$  structure-type has lattice parameters of  $a = 5.650(5) \text{ \AA}$ ,  $b = 4.892(5) \text{ \AA}$ ,  $c = 5.550(5) \text{ \AA}$ ,  $\beta = 120.42(7)^\circ$ . Tungsten dioxide can be synthesized from tungsten metal and the trioxide being heated together in a sealed tube at 950 °C for 40 hours. The dioxide will disassociate to the metal and  $\text{W}_{18}\text{O}_{49}$  above 1530(5) °C but can be stabilized up to 1700 °C with small amounts of Ca, Co or Sm. (Philips 1964). The high pressure phase was synthesized at 80 kbar and 1120 K and identified as a twinned structure using powder X-ray diffraction. (Sundberg1994). The monoclinic phase is the stable phase at ambient conditions as are



several solid solutions of  $\text{WO}_2$  with  $\text{VO}_2$  or  $\text{CrO}_2$  in the monoclinic or rutile structures.<sup>67,68</sup> Tungsten dioxide is also used in thin films and semiconductor devices.<sup>69</sup>

## ■ Vanadium Dioxide

Vanadium is a group 5 element and unlike the group 6 and 7 elements is known to form many dioxide polymorphs including a monoclinic phase in the  $\text{MoO}_2$  structure-type and a rutile phase. There are at least four other polymorphs that are found at high temperature/pressure conditions, associated with chromium doping or due to the metal-insulator transition. The monoclinic variant has lattice parameters of  $a = 5.743 \text{ \AA}$ ,  $b = 4.517 \text{ \AA}$ ,  $c = 5.375 \text{ \AA}$ , and  $\beta = 122.61^\circ$ .<sup>42</sup> This phase can be synthesized using hydrothermal techniques at  $500^\circ\text{C}$ .

## ■ Summary

The phase diagrams of transition metal oxides are rich with many structures and stoichiometries. Within the transition metal dioxides there are numerous structures stable at ambient conditions in addition to the structures accessed at non-ambient environments. Starting with the monoclinic phases known as the  $\text{MoO}_2$  structure-type, a family of chemical systems is created to include:  $\text{MoO}_2$ ,  $\text{WO}_2$ ,  $\text{TcO}_2$ ,  $\text{ReO}_2$  and  $\text{VO}_2$ . The second structure-type common to this family is the rutile phase. Each of the phase diagrams for the other chemical systems in the family include other phases that have been found through manipulating chemical pressure or external stimuli. The only common non-ambient phases are that of the high pressure orthorhombic phases of  $\text{WO}_2$  and  $\text{MoO}_2$  in the  $Pnma$  space group. The high temperature orthorhombic phase of  $\text{ReO}_2$  in the space group  $Pbcn$  is unique in this series of compounds but is the same structure-type as  $\alpha\text{-PbO}_2$ . To this date, no rutile phase nor any other polymorph has been characterized for  $\text{TcO}_2$ . The predicted distortion

of  $\text{TcO}_2$  octahedra with external pressure worth examining experimentally. Finally, it remains unknown whether  $\text{TcO}_2$  persists in its ambient structure or whether new and potentially recoverable structure types occur under non-ambient conditions.

Due to the closeness in atomic radii of molybdenum to technetium and the isoelectronic relationship of rhenium, only these two homologues will be investigated alongside technetium dioxide. For the purpose of this discussion, the scope will be restricted to the oxides most closely related to technetium: rhenium and molybdenum.

## ■ Heptoxides

Technetium(VII) heptoxide was first synthesized in 1952 by burning technetium metal in a dry oxygen atmosphere above 400 °C.<sup>70</sup> Light yellow crystals were formed and purified by sublimation within the reaction tube. Using Ce(IV) titration and UV-Vis spectroscopy the oxidation state was confirmed as being in the highest state available, +7. It was first noted in 1953 that, while  $\text{Tc}_2\text{O}_7$  is volatile at ambient conditions, the solid has an unexpectedly low vapor pressure.<sup>71</sup> It was also observed that the liquid stability range of  $\text{Re}_2\text{O}_7$  spans a 60 K range while  $\text{Tc}_2\text{O}_7$  spans a 190 K range. This presents challenges for engineering industrial processes when testing with non-radionuclides and assuming analogous behavior by corresponding states, as is common course of action.

The crystal structure was not reported for over a decade until 1969 by Krebs<sup>72</sup> who solved the structure in the space group *Pbca* with  $a = 13.756(7) \text{ \AA}$ ,  $b = 7.4394(4) \text{ \AA}$ ,  $c = 5.617(3) \text{ \AA}$ . The

chemical connectivity is the same as  $\text{Re}_2\text{O}_7$  and  $\text{Mn}_2\text{O}_7$  where each molecular unit consist of corner sharing tetrahedra resulting in a single bridging oxygen between the metal atoms. However, unlike the rhenium(VII) oxide, for technetium(VII) oxide packing structure is comprised of isolated molecules of  $\text{Tc}_2\text{O}_7$ . The molecular geometry of  $\text{Tc}_2\text{O}_7$  is unique in that there is a  $180^\circ$  bond angle between the two metal atoms and the bridging oxygen. In our recent report on the electronic structure of  $\text{M}_2\text{O}_7$  compounds, the nature of the bond with the bridging atom was identified as a nonclassical three center, four-electron covalent bond. Across the Group 7 heptoxides there are three centered bonds, but in the case of  $\text{Mn}_2\text{O}_7$  where there is a smaller angle between the subunits, there is more covalent nature to the bond.

The crystal structure of  $\text{Tc}_2\text{O}_7$  was recently solved at 100 K, and when compared to the original structure determined at ambient conditions, it was observed that the bond lengths reported at room temperature were shorter than at low temperature.<sup>10,72</sup>

## ■ High Pressure Generating Devices

In this section, the background for high pressure experiments is discuss with an emphasis on the methods for controlling temperature and pressure in synchrotron diffraction experiments and the framework for determining the equation of state.

Structural investigations of these materials are carried out using laboratory and synchrotron X-ray diffraction. High pressure is achieved using Diamond Anvil Cells, (DACs). High temperature is obtained using laser heating systems coupled with diamond anvil cells while low temperatures are

achieved using an Oxford Cryostream. Using the structural data collected under non-ambient conditions, elastic moduli can be defined using an equation of state, (EOS).

Crystallography in every environment has the same goal, to gather structural information. In addition to knowing the structure at any specific set of conditions we are looking for the relationship that takes the material from point A to point B. In this case these are pressure points.

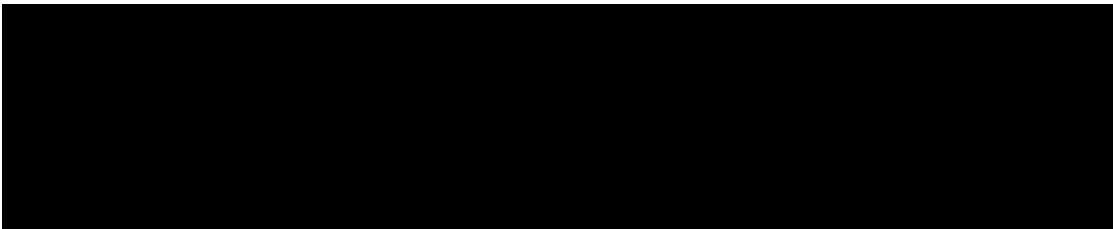
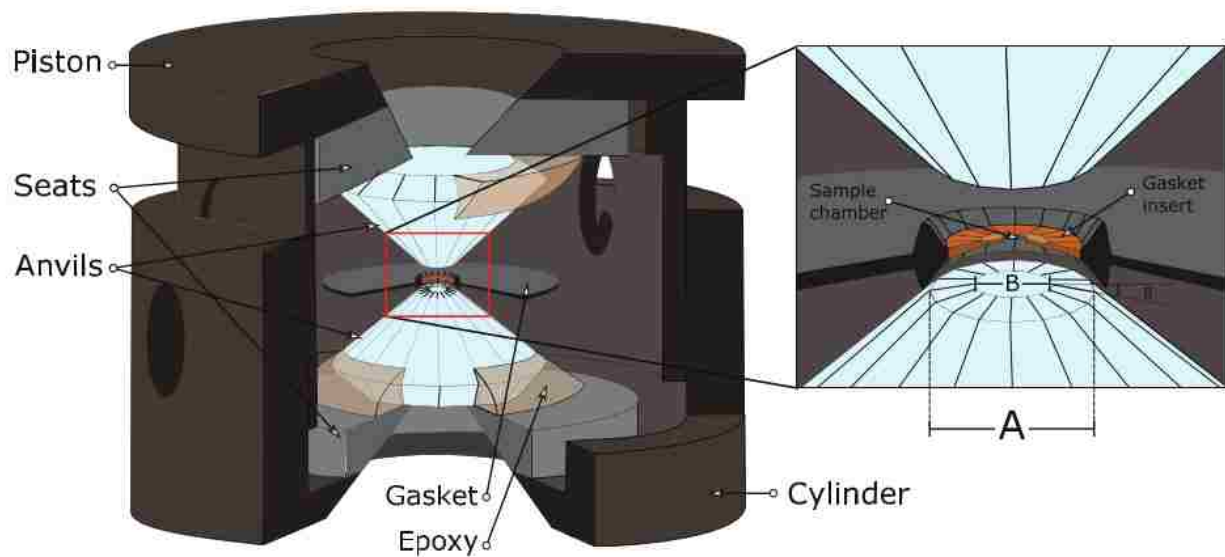
All static pressure devices operate under the same basic principle,  $P = F/A$  which can also be expressed as the three dimensional tensor of pressure. Two main approaches are taken to high pressure: large volume press (LVP) requiring a large force, or small volume requiring modest forces. The diamond-anvil cell is the leading device for the small volume high pressure devices. It is based off the opposed anvils developed by Bridgman but using diamonds in place of tungsten carbide. A variety of materials are now in use as anvil in the DAC design including single crystal diamond, sapphire, moissanite, and zirconia as well polycrystalline and nanocrystalline diamond. New materials and anvil designs are developed for use in the DAC to extend the accessible pressure range or make the DAC more compatible to a specific experimental need. In this work only single crystal type Ia diamonds are used for diffraction experiments.

The first compression experiments deformed material between two opposed diamonds. This allowed for visual observation of compressed material. It quickly became clear that the pressure was not homogenous in the sample and that there was a severe pressure gradient from the center radiating outwards. A thin metal foil used as a gasket allowed for the use of a pressure transmitting medium by providing a confined environment. This created a pseudo-hydrostatic environment as previous compression was only possible with a uniaxial load. The addition of the gasket and pressure medium lead to an increase in the pressure range that was readily achievable for study.

As higher pressures were reached the effects of nonhydrostatic pressures were explored and the necessity of soft pressure media became clear. The most widely used pressure media for high pressure studies beyond 10 GPa are ideal gasses, argon, neon, and helium. The hydrostatic limit of these gases decreases with size.

Two primary means of determining pressure are relied upon in a DAC: ruby fluorescence and measuring the diffraction from a material with a well-known EOS. The first has the obvious advantage of only requiring a laser and spectrometer. Ruby fluorescence has also been used to estimate the degree of nonhydrostaticity across the gasket hole. The ruby scale has been developed for use up to 160 GPa but the fluorescence signal can be suppressed at high pressure due to strain which restricts the use of the ruby scale.<sup>73</sup> Using a well-known EOS of a material with a simple structure that is relatively compressible at the target pressure range it is possible to determine the pressure accurately pressure less than 10 GPa and in excess of a Mbar. Common metals used for pressure determination include gold, copper, and platinum. It is also possible to estimate the pressure using diffraction of the pressure medium or gasket as well as the shift in the Raman signal of diamond. These methods are less reliable due to pressure gradients in the system.

Since diamonds have the advantage of being transparent to visible light, optical techniques are possible in the DAC in addition to X-ray and neutron scattering. X-ray diffraction is the primary technique for many structural studies and especially equation of state measurements. This is largely due to the quick data collection possible at synchrotron sources, the minimal amount of material necessary to perform X-Ray Diffraction, (XRD), and general accessibility of synchrotron facilities.

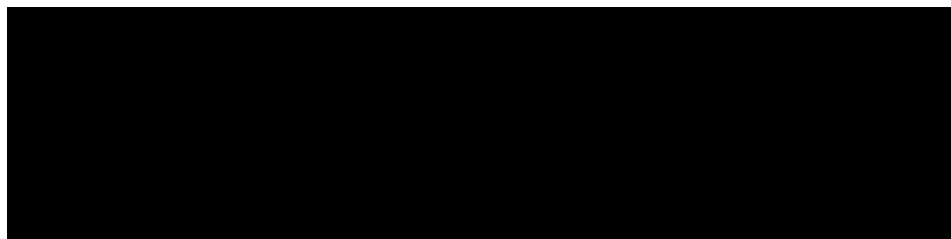


A loaded DAC is shown in **Figure 3** with the sample in the center of the gasket hole and a small ruby sphere placed next to it. The diamond culet is approximately 300  $\mu\text{m}$  in diameter, the gasket hole 150  $\mu\text{m}$  and the sample less than 30  $\mu\text{m}$ . The X-ray beam is transmitted through the diamond and scatters off the sample. When the diamonds are pushed together the sample chamber is compressed by the uniaxial load applied from the diamond as well as the confining pressure from the gasket material. The gasket deforms from the applied load of the diamond which causes the radial force on the sample chamber. This combination allows for a hydrostatic pressure to be felt by the sample for as long as the medium is sufficiently soft.

There are several obstacles that face crystallographic determinations from inside a diamond anvil cell. Primarily centered around the fact that the sample is inside of the cell. There is 4-5 mm of diamond that the beam must penetrate which reduces the signal and increases the background. The

angular access is reduced by the DAC body, which limits the availability of high angle peaks useful in structure determination. This also reduces the redundancy and completeness of single crystal data sets. Speaking directly of the conditions that are of interests, pressure, specifically non-hydrostatic pressures results in broadened peaks. Each diffraction experiment performed in a DAC is already a multiphase experiment in addition to having strained samples. Experiment design can reduce the effect of these factors on data quality and pressure as required for each experiment.

The diamond anvil cells used in this work included a modified Mao-Bell type cell and Membrane DAC designed at LLNL<sup>74</sup>, a four post cell, and a modified BX-90<sup>75</sup>. All of the DACs utilize the same opposed anvil configuration with a sample confined by a gasket and diagnostic performed using an angular dispersive geometry for monochromatic X-rays. Each DAC has a different opening that determines the angular access for downstream data collection or upstream which affects rotational ranges. The Triple Seal DAC was originally designed for powder XRD and Raman, in which the upstream side has  $\sim 5^\circ$  opening due to the long piston-cylinder design that increases the stability. The downstream side is designed for a slot opening seat with a high angles



accessible over a narrow  $\chi$ -range. This allows for greater support of the diamond while accessing the high angle  $2\theta$  range, but with lower statistics than those obtained at lower angles. The Membrane DAC also utilizes the large slot opening, however without the cylinder on the upstream side, it is compatible with laser heating techniques. The membrane DAC is a symmetric design and like the Triple Seal is used with standard or brilliant cut diamonds, or any diamond with a flat table. The four post cells consist of two plates, one with four large post and one with holes. The plates have large openings that access the entire  $\chi$ -range with  $2\theta$  openings up to  $35^\circ$ . In order to improve on this large opening, conical diamonds<sup>76</sup> are used. The two types of diamonds are shown in **Figure 3**. The conical diamonds are shorter, bringing the sample closer to the opening and improving the accessible angular range for diffraction/rotation. These DACs are suitable for powder and single crystal diffraction. A BX-90 DAC is shown in **Figure 2** equipped with standard cut diamonds.

## ■ Equations of State

An equation of state is a thermodynamic relationship of state variables such as pressure, volume, temperature and energy that is used to define the state of matter under a set of physical conditions. Using the relation between pressure, volume and temperature it is possible to define the elastic constant describing the compressibility and thermal expansion of a material. The bulk modulus is the instantaneous change in volume with pressure,  $K = -V(\partial P/\partial V)$ . The bulk modulus of transition metals ranges from 40 kbar to 4 Mbar.<sup>26</sup> There is no absolute thermodynamic basis for the variation of the bulk modulus with pressure so all equations of state have been developed based



upon a collection of assumptions.<sup>77-80</sup> The ability of these equations to reproduce experimental data accurately for different classes of materials is validation of the assumptions made.

The two equations of state that are commonly used in high pressure research are the Birch-Murnaghan and Vinet. The first follows the assumption that a Taylor series expansion that the finite Eulerian strain models the strain energy of a material under compression.

$$P = 3K_{0T}f_E(1 + 2f_E)^{5/2} \left( 1 + \frac{3}{2}(K'_{0T} - 4)f_E + \frac{3}{2}(K_{0T}K''_{0T} + (K'_{0T} - 4)(K'_{0T} - 3) + \frac{35}{9})f_E^2 \right)$$

$$f_E = \left[ (V_{0T}/V_{PT})^{2/3} - 1 \right] / 2$$

Where  $K_{0T}$  is the ambient pressure bulk modulus at a given temperature T,  $K'_{0T}$  is the first derivative with respect to pressure of the bulk modulus at a given temperature T,  $K''_{0T}$  is the second derivative of the ambient pressure bulk moduli at a given temperature T,  $V_{PT}$  is the unit cell volume at a given pressure and temperature P and T, respectively and  $V_{0T}$  is the unit cell volume at ambient pressure and a given temperature T.

The Vinet equation of state is derived from a generalized inter-atomic potential and more accurately describes the compression of material at very high compression,  $V_{PT}/V_{0T} < 0.6$ .

$$P = 3K_{0T} \frac{3f_V}{(1-f_V)^2} \exp\left(\frac{3}{2}(K'_{0T}-1)f_V\right)$$

$$f_V = 1 - (V_{PT}/V_{0T})^{1/3}$$

The bulk modulus and pressure derivatives can therefore be determined by measuring the applied pressure and the sample volume over a range of pressures. Both are typically determined by

diffraction methods. In a similar fashion, the thermal expansion of a material can be determined by measuring the volume of the sample as a function of temperature. The thermal expansion is defined by  $\alpha(T) = \frac{1}{V} (\partial V / \partial T)$ , which becomes,  $V_{0T} = V_{00} \exp \int_{T_{ref}}^T \alpha(T) dT$ , where  $V_{00}$  is the unit cell volume at room temperature and ambient pressure,  $V_{0T}$  is the unit cell volume at ambient pressure and a given temperature T, and  $T_{ref}$  is the reference temperature for room temperature. The coefficient of thermal expansion is a function of temperature and constrained to  $\alpha(T) = \partial \alpha / \partial T = 0$  at  $T = 0K$ . The expression  $\alpha(T) = \alpha_0 + \alpha_1 T + \alpha_2 T^{-2}$  was proposed by Fei (1995) where the coefficients correspond to the 0 K curve and are independent of the reference temperature. However the  $T^{-2}$  term diverges to infinity as T approaches 0 K.

One of the goals of our exploration of the high pressure structure of technetium metal is to create a definitive set of data defining the behavior of technetium metal under extreme conditions. Reliable elastic constants are necessary for method validation and for understanding periodic trends.

## ■ Conclusion

The lightest radioelement, technetium, wasn't discovered until 1936. With no natural source of gram-quantities of technetium we rely on reactor or accelerator produced material. The short history and scarcity has led to there being relatively few investigations into the physical properties and chemistry of technetium in comparison to rhenium. This gap in knowledge is exemplified by the difference between the two elements in the extent of exploration into their respective high-pressure phase diagrams and equations of states. The bulk modulus of technetium has been

measured at ambient conditions once. For rhenium there are more than 10 high pressure structural studies which include the highest of static pressures achieved.<sup>16,81</sup> This trend is seen across all technetium compounds but in particular we will focus on the non-ambient behavior of technetium oxides.

The dissertation consists of the introduction (Chapter 1), experimental methods (Chapter 2), results (Chapters 3 to 7) and a conclusion. In the methods, pressure generating devices, X-ray diffraction, and data analysis will be discussed. A theoretical framework for high pressure science will be given including a discussion of equations of state for solids, solid state phase transitions, pressure determination and pressure transmitting mediums.

In Chapter 3, the structure of technetium metal are studied at variable temperature using high resolution synchrotron powder diffraction. The coefficient of thermal expansion of technetium metal is determined at ambient pressure and the ambient structure of technetium is determined with higher precision.

In Chapter 4, the ambient temperature equation of state (EoS) of technetium metal was measured by powder X-ray diffraction. The metal was compressed using a diamond anvil cell and using a 4:1 methanol-ethanol pressure transmitting medium. The maximum pressure achieved, as determined from the gold pressure scale, was 67 GPa.

In Chapter 5, the equation of state of technetium metal is revisited using a neon pressure transmitting medium. Powder X-ray diffraction was collected up to 151 GPa in a neon medium with a copper pressure marker. Using this and the data from the previous two chapters a final recommendation for the equation of state for technetium metal is made.

In Chapter 6, the high pressure phase diagram of transition metal dioxides ( $\text{ReO}_2$ ,  $\text{MoO}_2$ ,  $\text{TcO}_2$ ) is studied. The compression of  $\alpha\text{-ReO}_2$  and subsequent decompression after conversion to  $\beta\text{-ReO}_2$  is studied. The isothermal compression of  $\text{MoO}_2$  led to the observation of a multi-phase region and the identification of a new high-pressure phase of  $\text{MoO}_2$ . The compression of  $\text{TcO}_2$  demonstrates the stability of the monoclinic phase up to the highest pressure achieved. An equation of state is determined for each system.

In Chapter 7, the structure of  $\text{Tc}_2\text{O}_7$  is revisited at low temperatures. The thermal expansion behavior is determined by single-crystal X-ray diffraction. Using *ab initio* molecular dynamics alongside crystallographic results the thermal motion in the molecular systems is described and insight into the mechanism of melting is provided.

# Methods

## Synchrotron Facilities

Most of the X-ray diffraction data presented in this dissertation were collected at two third-generation synchrotron sources; the Advanced Photon Source (APS), at Argonne National Laboratory, near Chicago, IL, USA or at the Advanced Photon Source (ALS) at Lawrence Berkeley National Laboratory. Four different beamlines were used: 16-BM-D (high pressure pXRD), 16-ID-B (high pressure pXRD) and 11-BM-B (variable-temperature pXRD with a nitrogen cryostream) and 12.2.2 (high pressure pXRD and laser heating).

A synchrotron operates under a principle similar to Bremsstrahlung or “braking radiation”. When the path of a high energy particle such as an electron is changed, then radiation is released due to the change in acceleration. A storage ring is used to maintain a current of electrons traveling at relativistic speeds. The path of the electron is manipulated using several configurations of electromagnets such as bending magnets (BM), wigglers, and undulators. These are the foundation of the experimental stations where radiation is emitted from the beamlines to experimental stations called hutches.

## Treatment of Synchrotron Data

Diffraction data gathered using laboratory diffraction instruments are standardized in their collection setup, strategies, and reduction. Synchrotron data is a product of the experiment goals

and can vary. For diamond anvil cell experiments the most common diffraction experiment is angular dispersive, a transmission geometry where the monochromatic X-rays travel through the table of the diamond, and then the sample where they are diffracted out the second diamond to be collected by an area detector. An area detector with known pixel size is calibrated for distance, center position, pitch, tilt, and rotation using a diffraction standard such as CeO<sub>2</sub> or LaB<sub>6</sub>. If multiple sample to detector distances or center positions are used, they are individually calibrated. The raw data is an image file with Debye-Scherrer rings. Since X-rays are passing through the diamonds, and pressure transmitting medium, it is probable that there is scattering due to other sources in addition to the sample. In cases where single crystal diamond or pressure medium peaks are present it is necessary to mask regions of the image before the integration is performed. Azimuthal integration of the rings is performed in Fit2D<sup>82</sup> or Dioptase using the calibration file. The integrated 1-D powder diffraction pattern can then be analyzed using standard software available for indexing, Le Bail or Pawling fitting and Rietveld Refinement.

Using the refinement results from the unit cell parameters for the pressure standard, the pressure is calculated using the known values for the bulk modulus. Standard uncertainties from the structure refinement are propagated through the equation of state to determine the uncertainty in the pressure. The uncertainty stated here is commonly understood within the crystallographic community to be a low estimate. The pressure gradients in the DAC gives rise to the possibility that the pressure standard and the sample experience different pressure conditions. This is particularly true for nonhydrostatic pressure environments. Using an analysis of the sample stress and strain, a more detailed description of the sample environment can be generated to assist in interrupting the experimental uncertainties. The paired data of pressure and sample volume are then used to create a data set that can be fit by an equation of state. The software package, EOSFit,<sup>83</sup>

can be used to perform fits for several standard equation of state forms as well as linear compressibility.

## ■ Laboratory Single Crystal X-Ray Diffraction

Single Crystal X-ray diffraction was performed using a laboratory source at UNLV, the Bruker D8 Venture with an APEX II detector. This instrument is configured with a fixed-chi goniometer and an Oxford N<sub>2</sub> Cryostream. In the APEX II suite,<sup>84</sup> data reduction was performed using SAINT, the structure was solved with SHELXT,<sup>85</sup> and an absorption correction was performed with SADABS.<sup>86</sup> Structure solutions were conducted independently at each temperature. Structure refinements against  $F^2$  were carried out using the SHELXL refinement package in OLEX2-1.2.<sup>87</sup>

# Thermal Expansion of

## Techneium Metal

### Introduction

The crystal structure was first determined by Mooney in 1948 as a hexagonally closed packed structure with  $Z = 2$  in the space group  $P6_3/mmc$ .<sup>88</sup> A survey of lattice parameters determined for technetium metal at ambient conditions are summarized in **Table 2**. The values attributed to Rard *et al.*<sup>99</sup> result from a weighted average of the values reported before 1999. The thermal expansion of technetium and its alloys have been studied at low temperatures, starting with Marples *et al.* investigating the Tc-Mo system. The lattice parameters and coefficient of thermal expansion was

**Table 2.** Unit cell parameters for hcp technetium at ambient conditions. The sample analysed by Muller contained interstitial oxygen atoms.

a (Å)	c(Å)	c/a	Vol (Å <sup>3</sup> /Z)	Method	Reference
2.735(2)	4.388(2)	1.6044	14.2129	XRD	Mooney <sup>88</sup>
2.7407(2)	4.3980(2)	1.6047	14.3047	XRD	Marples <sup>89</sup>
2.756	4.398	1.5958	14.4649	DFT	Weck <sup>90</sup>
2.743(2)	4.400(2)	1.6041	14.3352	XRD	Lam <sup>91</sup>
2.742(2)	4.400(2)	1.6047	14.3248	XRD	Muller <sup>92</sup>
2.7414	4.3997	1.6049	14.3175	XRD	Baker <sup>93</sup>
2.740	4.398	1.6051	14.2974	DFT	Trzebiatowski <sup>94</sup>
2.743	4.400	1.6041	14.3352	XRD	Koch <sup>95</sup>
2.74(1)	4.39(1)	1.606	14.271	XRD	Spitsyn <sup>96</sup>
2.740(2)	4.399(4)	1.6055	14.3006	XRD	Giorgi <sup>97</sup>
2.7375	4.395	1.6055	14.2616	-	Haines <sup>98</sup>
<b>2.7409(35)</b>	<b>4.3987(34)</b>	<b>1.6048</b>	<b>14.3091</b>	<b>Average</b>	<b>Rard<sup>99</sup></b>



reported to decrease smoothly from 298K to 4.2K. The coefficients of thermal expansion were reported to be  $\alpha_a = 7.04 \times 10^{-6} \text{ K}^{-1}$  and  $\alpha_c = 7.06 \times 10^{-6} \text{ K}^{-1}$  between 150 and 298 K.<sup>89</sup> It was noted that the axial ratio only decreased by 0.002Å at 4.2K.

A second study used push-rod dilatometry to measure the bulk polycrystalline thermal expansion of Tc-Ru alloys. The pure metals and alloys of 3:1, 1:1, and 1:3 were measured. The thermal expansion of technetium metal was fit by a polynomial as  $\Delta L/L_{323\text{K}} = -0.268 + 8.550 \times 10^{-4} T - 1.048 \times 10^{-7} T^2 + 9.204 \times 10^{-11} T^3$ , where L is the length of the sample and  $\Delta L$  is the change in length.<sup>100</sup> They found that, while the 3:1 and 1:1 samples had thermal expansion coefficients between the two metals, that the 1:3 sample had a smaller rate of expansion than ruthenium metal. This behavior was attributed to preferred orientation in the ruthenium metal sample where the *c*-axis preferred to be arranged along the longitudinal direction of the rod. The predicted thermal expansion for technetium is in good agreement with the dilatometry data with at most ~6% discrepancy at high temperatures.<sup>90</sup> It can be misleading to directly compare dilatometry to diffraction thermal expansion. The atomistic model determined by diffraction techniques defines the linear thermal expansion along each crystallographic axis as well as the volumetric change. In dilatometry measurements the measured thermal expansion is an average of the expansion in the three crystallographic directions and therefore is susceptible to preferred orientation of the bulk material (i.e. from pressing or rolling metal). The predicted thermal expansion of HCP technetium metal is in excellent agreement, deviating less than 0.1%, with the experimental dilatometer data. In the present work, the thermal expansion of technetium metal has been studied from 100-450 K at ambient pressure by *in situ* synchrotron X-ray diffraction.

## ■ Methods

*Caution:* Technetium-99 is a weak beta emitter ( $E_{\text{max}} = 293 \text{ keV}$ ). All manipulations were performed in a radiochemistry laboratory at UNLV designed for chemical synthesis using efficient HEPA-filtered fume hoods, and following locally approved radioisotope handling and monitoring procedures.

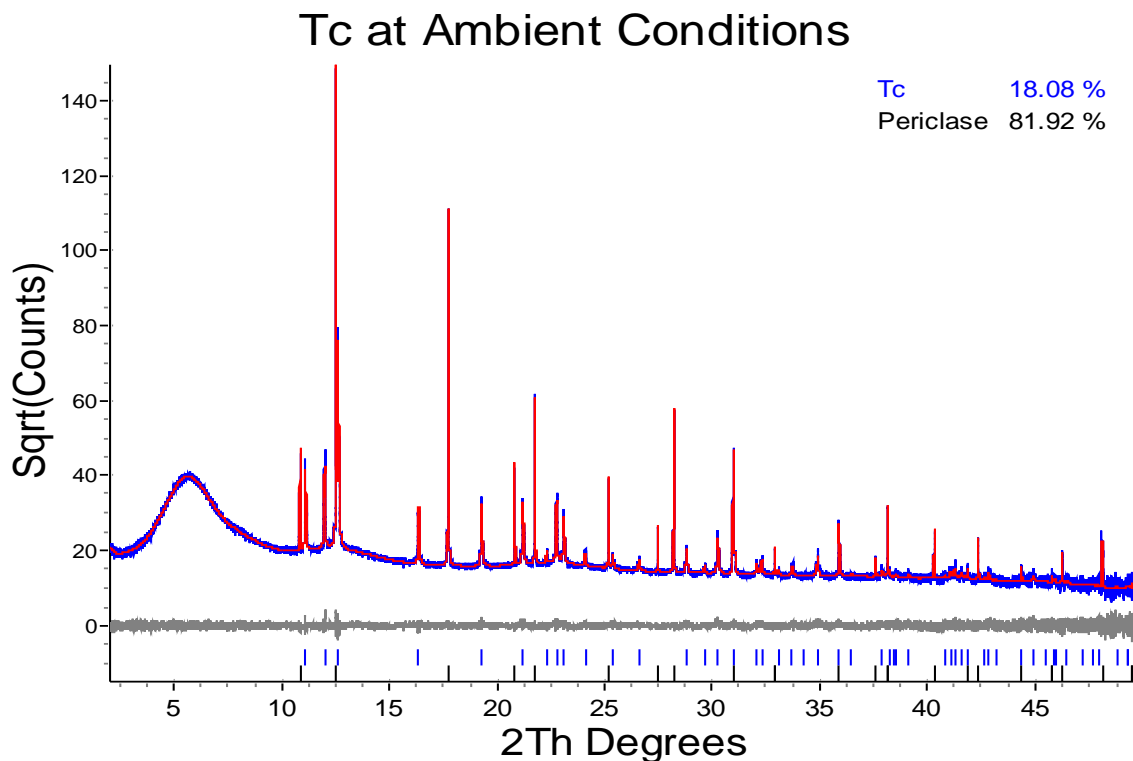
Technetium powder was mixed with MgO in a ratio of 1:4 to reduce the absorbance. The sample powder was loaded in a 0.8 mm diameter, double-walled kapton capillary. High-resolution synchrotron powder diffraction data was collected using beamline 11-BM at the Advanced Photon Source (APS), Argonne National Laboratory, Illinois, USA. A mixture of NIST standard reference materials Si (SRM 640c) and  $\text{Al}_2\text{O}_3$  (SRM 676) was used to calibrate the instrument, where the Si lattice constant determined the wavelength for each detector. An average wavelength of  $0.459001\text{\AA}^{101}$  was determined and data was collected over the  $0.5 - 50^\circ 2\theta$  range using a step size of  $0.001^\circ$ . The Oxford Instruments Cryostream 700 Plus  $\text{N}_2$  gas blower was used to provide the sample environment. Data was collected continuously from 100K to 450K with a ramp rate of 0.2K/min. Each diffraction pattern was collected for 10 minutes covering a change of 2 degrees Kelvin. The temperature at the start of each scan was recorded by the instrument for comparison. A long scan of 60 minutes was collected at room temperature ( $T = 287 \text{ K}$ ).

The program suite TOPAS4.2 was used for the Rietveld analysis of this powder X-ray diffraction data. The lattice constants, two Pseudo-Voigt profile coefficients and scale factors were refined. The HCP technetium metal structure reported by Mooney<sup>88</sup> and MgO structure reported by Schiebold<sup>102</sup> were used as a starting models. The background was fitted with a 13 term Chebyshev

polynomial. Peak profiles were modeled using a pseudo-Voigt function. The effects of absorption were modeled within TOPAZ4.2 assuming a 60% packing density for the capillary and a computed linear absorption coefficient of  $26.32 \text{ cm}^{-1}$ .

## ■ Results & Discussion

The ambient crystal structure of technetium metal was determined without altering the sample temperature using the cryostream. The ambient temperature was measured to be  $T_0 = 287 \text{ K}$ . A two-phase Rietveld refinement was performed using TOPAS4.2 as shown in **Figure 4**. The amorphous scattering from the double-walled kapton capillary contributed to a broad peak at  $6^\circ$ . The background was fit using a 5<sup>th</sup>-order chebychevs polynomial. The peaks shapes were modeled using a pseudo-Voigt function. The quantitative refinement showed that the mixture was just under

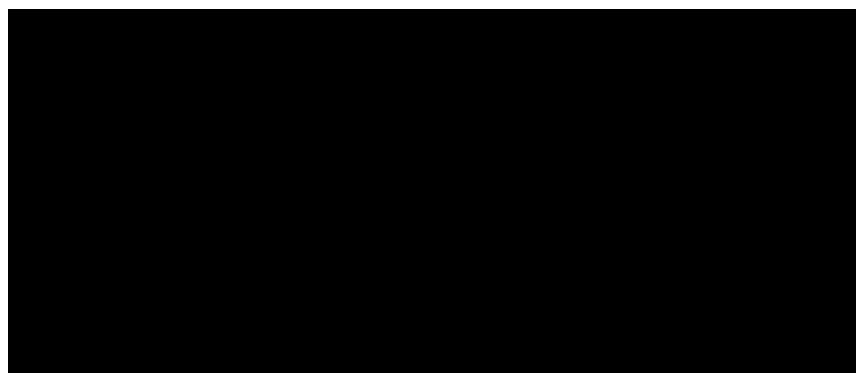
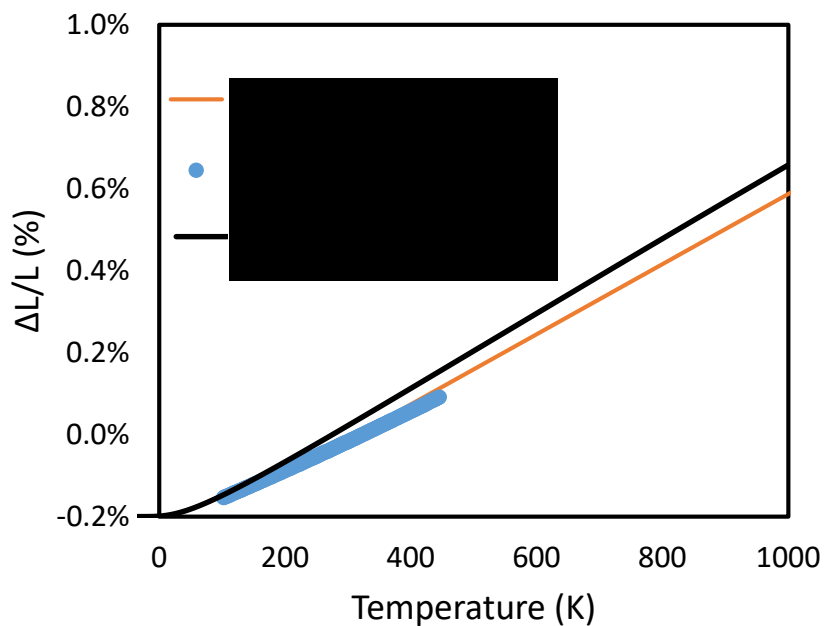


the intended 1:4 ratio for technetium metal to magnesium oxide. All atoms are on special positions. The unit cell parameters determined for technetium are  $a = 2.74109(1) \text{ \AA}$ ,  $c = 4.39898(3) \text{ \AA}$  and  $V = 28.6239(3) \text{ \AA}^3$ , and for MgO  $a = 4.21186(1) \text{ \AA}$ . This is in excellent agreement with the weighted average from the NEA Thermodynamics Databases.<sup>99</sup>

The lattice parameters increase smoothly from 100 K to 450 K with no indication of a phase transition. The axial ratio of 1.6048 remains constant over the entire temperature range. The temperature dependence of the lattice parameters can be categorized as quasi-linear. In an effort to better fit the nonlinearity of the thermal expansion the Fei equation for thermal expansion was tested using 1, 2 and 3 parameters. The coefficient of thermal expansion is defined by the three-parameter function,  $\alpha(T) = \alpha_0 + \alpha_1 T + \alpha_2 \frac{1}{T}$ . The integral of this can be used to define the change in volume or in each crystallographic axis,  $V_{0T} = V_{00} \exp(\alpha_0(T - T_{ref}) + \frac{1}{2}\alpha_1(T^2 - T_{ref}^2))$ . In this way the volumetric and linear thermal expansion coefficients can be defined from crystallographic datasets. Fitting results are listed in **Table 3** for the 1 and 2 parameter equations. Fitting with 3 parameters did not improve any of the fits.

**Table 3.** Coefficients of thermal expansion

	1 <sup>st</sup> order			2 <sup>nd</sup> order		
	Volume ( $\text{\AA}^3/\text{atom}$ )	a ( $\text{\AA}$ )	c ( $\text{\AA}$ )	Volume ( $\text{\AA}^3/\text{atom}$ )	a ( $\text{\AA}$ )	c ( $\text{\AA}$ )
	14.2546(9)	2.73739(1)	4.39894(2)	14.2560(4)	2.7375(1)	4.39326(1)
$\alpha_0$	2.145(3)	0.725(2)	0.697(3)	1.890(5)	0.606(5)	0.699(5)
$\alpha_1$				0.93(2)	0.43(2)	0.06(2)



The quality of the fit improved for the 2-parameter equation for the volumetric and *a*-axis directions but did not change significantly for the refinement of the data in the *c*-axis direction. The single parameter equation is more routinely reported for representing the linear thermal expansion and so is included here for ease of comparison with other findings. These results are in fair agreement with the diffraction results from Marples *et al.*,<sup>89</sup> which were measured from 150 to 298 K. Only two data points were reported along with the thermal expansion in Marples *et al.*<sup>89</sup> The uncertainties accompanying the lattice parameters were an order of magnitude larger than the results reported here so it is then reasonable to conclude that a similar degree of uncertainty applies to the coefficients of thermal expansion. Their reported values for the coefficients of thermal

expansion are nearly the same but with the  $c$ -axis being slightly more responsive to temperature change than the  $a$ -axis. This is the opposite of the results of this study with the  $a$ -axis being approximately 4% more sensitive to temperature. It is probable that the difference in expansion rate between the different directions is too small to have been seen in the original measurements. To compare with results from push-rod dilatometer which are reported in  $\Delta L/L(Tc)$ , an estimated equivalence of  $L_o = V_o^{1/3}$  is used to calculate temperature-volume data. This data was fit to determine the linear thermal expansion to compare with microscopic techniques. At the highest temperature measured in the diffraction experiment the relative percent difference is 23.3 % lower than the dilatometry results. Similar to the difference that was seen between the alloys due to averaging of the crystallographic directions over the polycrystalline bulk sample the difference between our measurements show that while there is fair agreement, the microscopic measurement of thermal expansion accounts for behavior that cannot be deconvoluted by dilatometry. The computed thermal expansion which was determined by density functional perturbation theory (DFPT) has also been reported and is compared as  $\Delta L/L(Tc)$  in **Figure 5**. The linear coefficient of thermal expansion was determined for the DFPT data and compared to the other techniques in **Table 4**. There are two distinct categories of coefficients of thermal expansion shown here. The two XRD experiments and then the dilatometry/DFPT. The XRD measurements while taken using different sampling profiles with a different number of data points, agree well with a smaller coefficient of thermal expansion than reported from dilatometry or DFPT. It is noteworthy that the DFPT data has more nonlinear behavior than observed in the diffraction results and is not modelled as well by the linear thermal expansion description. Another difference between the reports is that a lower temperature range is probed in the diffraction experiments.

**Table 4.** Coefficient of thermal expansion of technetium metal. \*A reference length of  $L_o = V_o^{1/3}$ , for L = 323 K was used for comarision.

$\alpha_0$ ( $10^{-5} \text{ K}^{-1}$ )	Method	Temperature Range	Reference
2.145(3)	XRD	100 - 450 K	This Work
2.11	XRD	150 - 298 K	89
2.56	Dilatometer*	300 - 1250 K	100
2.62	DFPT	0 - 2000 K	90

## ■ Conclusion

The high-resolution X-ray diffraction data presented in this chapter provides new microscopic measurement of the thermal expansion and ambient structure of technetium metal. The data is in excellent agreement with the limited diffraction results while varying more than 20% at the highest temperature achieved from results measured using push-rod dilatometry. The use of diffraction data to describe the structural response of technetium metal to temperature allows for a more detailed and reliable model for predicting real world behavior. This data creates a benchmark crsytallographic description of the thermal expansion.

# Equation of state for technetium from X-ray diffraction and first-principle calculations<sup>103</sup>

## Introduction

The known phase diagram of metallic technetium is simple and remains one of the least explored for any transition metal with few investigations establishing the structure and properties of technetium metal at high pressures. Accordingly, understanding the pressure and temperature dependence of the thermal, mechanical, and electronic properties of technetium is of significance to nuclear waste storage and condensed-matter physics.

The ambient pressure bulk modulus and other elastic moduli have been determined multiple times by experiments and calculations, summarized in **Table 5**, with no understanding of how these values or other properties vary under high pressures. In 1989, Guillermet<sup>25</sup> published an extensive review of the thermodynamic properties of technetium and then in 1999 the Nuclear Energy Agency published a report for the Thermodynamic Data Base project on the Chemical Thermodynamics of Technetium,<sup>99</sup> both of which both demonstrate a lack of data on the materials properties of elemental technetium at extreme conditions.



**Table 5.** Summary of ambient pressure bulk moduli. The value determined by ultrasonic measurements is the adiabatic bulk modulus,  $B_{us} = 2.81$  Mbar and is listed as the isothermal value.

$B_o$ (Mbar)	Method	Reference
2.88	Ultrasonic Velocity Measurements	Love <i>et al.</i> (Ref. <sup>28</sup> )
3.70	Waser Approximation	Porter(Ref. <sup>34</sup> )
2.963	Pseudopotentials	Baria <i>et al.</i> (Ref. <sup>104</sup> )
2.97	Muffin-tin Orbital Theory	Walzer (Ref. <sup>24</sup> )
2.95	Metallic Electron-Gas Model	Wojciechowski (Ref. <sup>26</sup> )
2.98	GGA/PW91	Weck <i>et al.</i> (Ref. <sup>27</sup> )

Here, we report room-temperature synchrotron diffraction measurements up to 67 GPa and establish an EOS derived from non-hydrostatic high-pressure diffraction experiments. In addition, first-principles total-energy calculations have been carried out to determine the structural properties and compressibility of bulk technetium up to 273 GPa. Our objective is to determine an EOS of technetium and create a baseline for further high pressure studies of technetium metal and relevant systems.

## Methods

*Caution:* Technetium-99 is a weak beta emitter ( $E_{max} = 293$  keV). All manipulations were performed in a radiochemistry laboratory at UNLV designed for chemical synthesis using efficient HEPA-filtered fume hoods, and following locally approved radioisotope handling and monitoring procedures.

Techneium-99 metal was synthesized as polycrystalline aggregates in the radiochemistry laboratory at UNLV as previously described.<sup>105</sup> A modified Mao-Bell cell with a slot opening and a four-post cell with a wide aperture were used. The Mao-Bell type cell was configured with two standard brilliant cut diamonds, with 300  $\mu\text{m}$  culets. The four-post cell was equipped with one standard and one Boehler-Almax<sup>76</sup> diamond. A grain of technetium no more than 15  $\mu\text{m}$  thick was loaded into a 100-150  $\mu\text{m}$  diameter hole in a rhenium gasket with a 10  $\mu\text{m}$  thick flake of gold (Alfa Aesar 99.8% pure) and then filled with a 4:1 mixture of methanol-ethanol as the pressure transmitting medium. The sample and pressure standard were placed approximately 15  $\mu\text{m}$  apart. Using a micro-focused beam of less than 10  $\mu\text{m}$  in width or height, diffraction patterns of the standard were collected independently of the sample. The choice in pressure medium is not ideal for hydrostatic measurements beyond 10 GPa<sup>106</sup> but can yield valuable information since the choice of confining media is limited by safety concerns for handling radioactive material.

Angular-dispersive X-ray powder diffraction data of technetium and gold in a diamond-anvil cell was obtained at beamlines 16-ID-B and 16-BM-D of the High Pressure Collaborative Access Team (HPCAT) at the Advanced Photon Source (APS). In order to prevent dispersal of radioactive material in the case of diamond failure, mylar windows were added to the DAC containment. At each beamline, diffraction patterns were collected with a MAR345 image plate with incident monochromatic beams of 29.200 keV and 33.169 keV X-rays. The sample to detector distances were calibrated with CeO<sub>2</sub> (SRM 674b), then the two-dimensional images were integrated and corrected for distortions using FIT2D.<sup>82</sup> Rietveld refinements were performed using TOPAS4.

First-principles total-energy calculations were performed using spin-polarized density functional theory, as implemented in the Vienna Ab initio Simulation Package (VASP).<sup>107</sup> The exchange-

correlation energy was calculated using the generalized gradient approximation<sup>108</sup> (GGA) with the parametrization of Perdew and Wang<sup>109</sup> (PW91). This functional was found to correctly describe the geometric parameters and properties of technetium bulk and cluster structures.<sup>110,27</sup>

The interaction between valence electrons and ionic cores was described by the Projector Augmented Wave (PAW) method.<sup>111,112</sup> The Tc  $4p^6 5s^2 4d^5$  electrons were treated explicitly as valence electrons in the Kohn-Sham (KS) equations and the remaining cores were represented by PAW pseudopotentials. The core radii of the PAW potential for Tc is 2.75. The KS equations were solved using the blocked Davidson iterative matrix diagonalization scheme followed by the residual vector minimization method. The plane-wave cutoff energy for the electronic wave functions was set to 500 eV. The technetium HCP crystal structure was optimized with periodic boundary conditions applied using the conjugate gradient method, accelerated using the Methfessel-Paxton Fermi-level smearing<sup>113</sup> with a Gaussian width of 0.1 eV. The total energy of the molecular system and Hellmann-Feynman forces acting on atoms were calculated with convergence tolerances set to  $10^{-3}$  eV and  $0.01$  eV/Å, respectively. Structural optimization was carried out using the Monkhorst-Pack special  $k$ -point scheme<sup>114</sup> with a  $11 \times 11 \times 11$  mesh for integration in the Brillouin zone (BZ). For each compression state, the  $c/a$  ratio optimization of the lattice parameters was performed at constant volume.

## ■ Results & Discussion

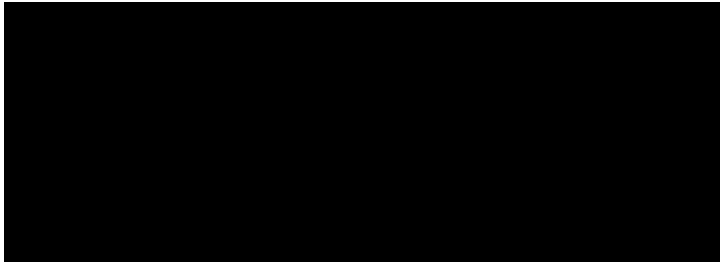
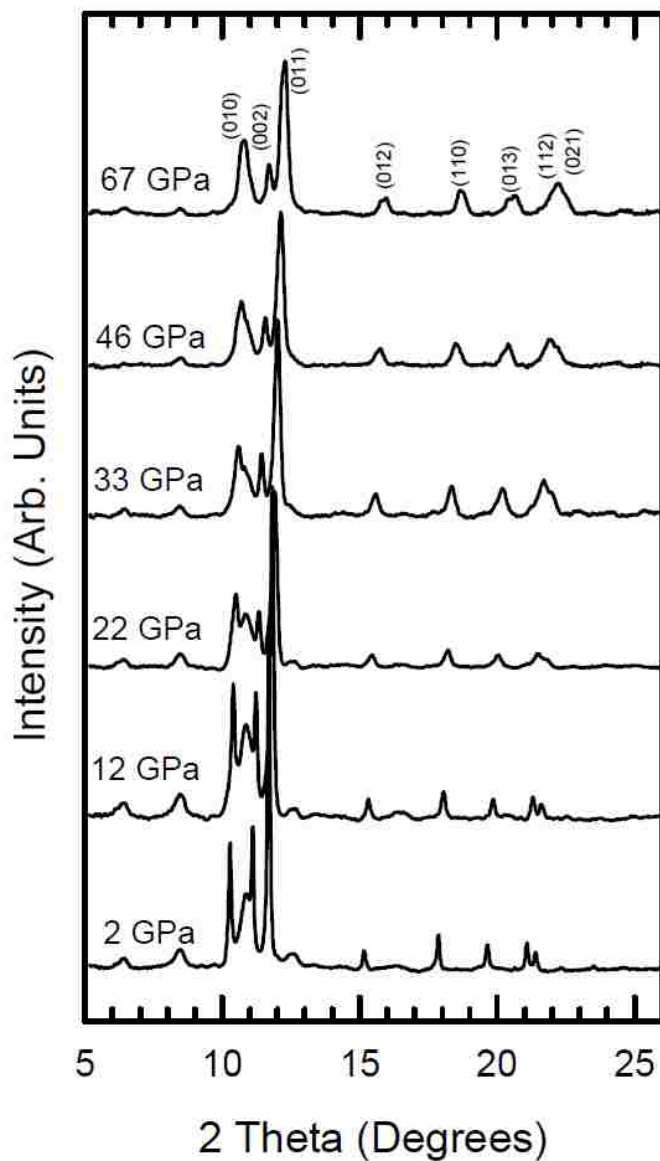
Representative diffraction patterns measured over the pressure range of this work are shown in **Figure 6**. The mylar windows contributed three reflections to each diffraction pattern at  $2\theta = 6.4^\circ$ ,  $8.6^\circ$ ,  $10.9^\circ$ ; these reflections were excluded from the final refinements. Eight reflections belonging

to the sample were identified in the region of  $2\theta = 10^\circ - 30^\circ$ . At each pressure, seven peaks were observed which index to gold. The sample pressure was determined using the EoS parameters recommended by Takemura and Dewaele,<sup>115</sup>  $B_o = 167$  GPa, and  $B'_o = 5.9(1)$ . No correction was applied to the pressure. Uncertainty in the pressure was estimated to be less than 2% over this pressure range.<sup>116</sup> The measured P-V data points are presented in **Appendix A:** and plotted in **Figure 7.**

A 4:1 mixture of methanol-ethanol is commonly used as a quasi-hydrostatic medium and is reported to provide hydrostatic conditions up to 10.5 GPa.<sup>106,117</sup> In a nonhydrostatic environment each crystallite experiences different stress conditions. The micro-stress may be estimated from the broadening of the diffraction peaks<sup>23</sup> and the Young's modulus.<sup>25</sup> **Figure 8** shows the evolution of the micro-stress as a function of pressure. Below 9 GPa, when the medium is a fluid, there is no significant change in micro-stress. Once the medium is solid, the stress profile displays three domains: strongly increasing up to 22 GPa, invariant from 22 to 40 GPa and then gradually increasing beyond 40 GPa. The considerable amount of micro-stress at these pressures introduces uncertainty into lattice parameters and consequently, to the equation of state.

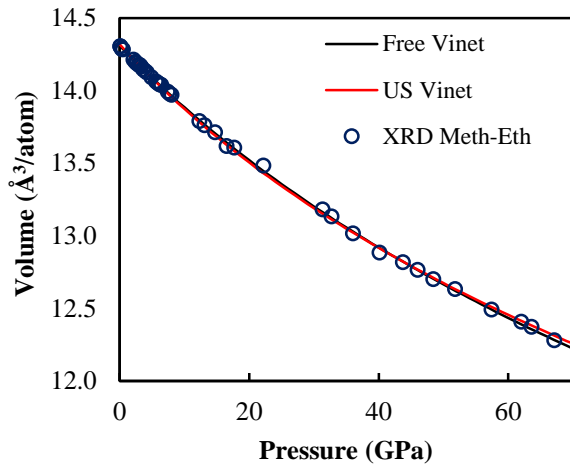
In light of the variation of micro-stress with pressure, two pressure ranges were considered in determining the EoS, 0-10 GPa and 0-67 GPa. The first range is in the hydrostatic regime for this pressure medium and the second is the full pressure range of this study. Using the software package EoSfit7GUI<sup>83</sup> the data was fit to a third-order Birch-Murnaghan and Vinet EoS at each step in the analysis. For the low pressure range the 2<sup>nd</sup> and 3<sup>rd</sup> order equations are used, while only the 3<sup>rd</sup> order equations are considered for the full pressure range. Given the strong correlation between the bulk modulus and its pressure derivative it would be preferable to independently determine the

bulk modulus and its pressure derivative. In a recent study of the gold pressure standard<sup>115</sup>, the ambient-pressure bulk modulus was fixed to a value that the literature agreed upon from several experimental methods, and then the pressure derivative was refined against the high pressure

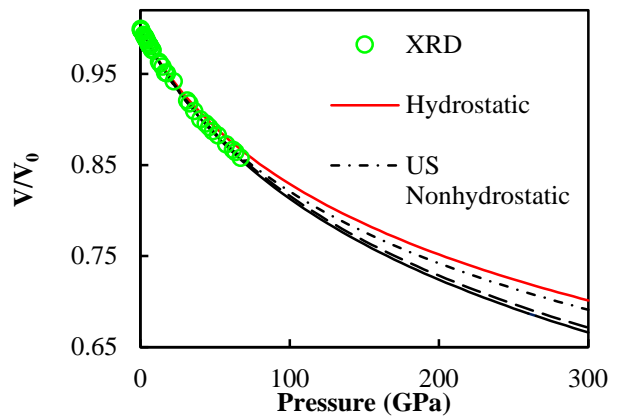


diffraction data. Without a surplus of values to compare from multiple experimental techniques we used the sole published value determined from ultrasonic data. The estimated uncertainties reported in parenthesis include contributions from the pressure determination, lattice parameters determination and the quality of the fitting of the PV data. Fitting errors are defined at the 95% confidence level.<sup>83</sup>

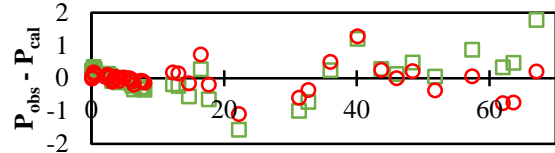
**a) EOS of technetium**

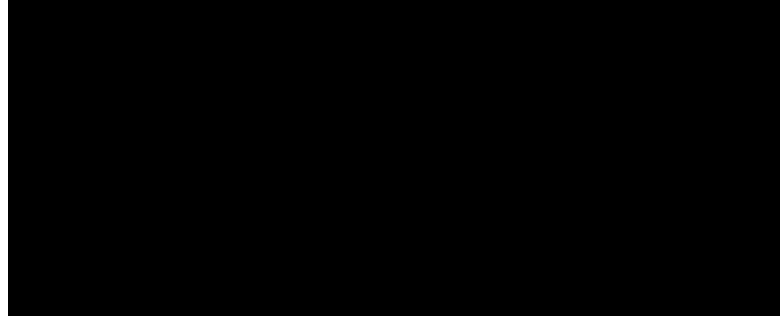
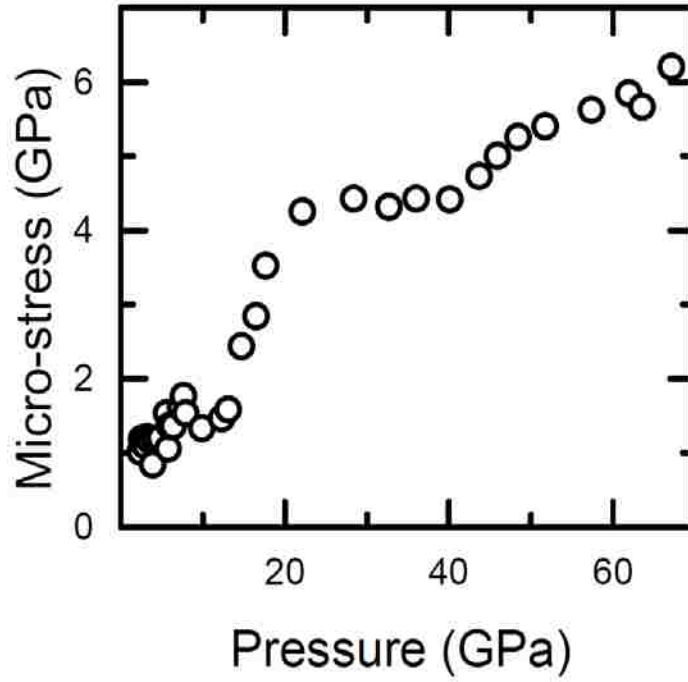


**b) EOS of technetium**



**c) Pressure Difference**





The EoS parameters for the hydrostatic pressure range refined using the second order Vinet equation are  $V_0 = 14.301(4) \text{ \AA}^3/\text{atom}$ ,  $B_0 = 333(8) \text{ GPa}$ , and for Birch-Murnaghan equation are  $V_0 = 14.305(4) \text{ \AA}^3/\text{atom}$ ,  $B_0 = 321(8) \text{ GPa}$ . The refined EoS parameters are  $V_0 = 14.307(7) \text{ \AA}^3/\text{atom}$ ,  $B_0 = 310(20) \text{ GPa}$ ,  $B'_0 = 6(6)$  for both the third order Vinet and Birch-Murnaghan equations. The data from the full pressure range was fit with all parameters free obtaining  $V_0 = 14.310(4) \text{ \AA}^3/\text{atom}$ ,  $B_0 = 309(7) \text{ GPa}$  and  $B'_0 = 4.7(4)$  for the Vinet equation and  $V_0 = 14.309(4) \text{ \AA}^3/\text{atom}$ ,  $B_0 = 309(7) \text{ GPa}$  and  $B'_0 = 4.6(4)$  for the Birch-Murnaghan equation. For the combined X-ray and Ultrasonic analysis, the isothermal bulk modulus was fixed at  $B_0 = 288 \text{ GPa}$ , which is the converted value from the adiabatic bulk moduli determined from the ultrasonic measurement.<sup>28,118</sup> For the Vinet

equation this yielded values of  $V_0 = 14.320(2) \text{ \AA}^3/\text{atom}$ ,  $B_0 = 288 \text{ GPa}$  and  $B'_0 = 5.9(2)$  for the Birch-Murnaghan equation  $V_0 = 14.320(2) \text{ \AA}^3/\text{atom}$ ,  $B_0 = 288 \text{ GPa}$  and  $B'_0 = 5.8(2)$ .

The calculated volumes of technetium in hcp packing show a continuous decrease up to 273 GPa. The choice in functional has been previously demonstrated to work reliably for technetium-containing structures.<sup>27</sup> While the volumes are systematically overestimated by about 1.3%, the compressibility is in good agreement with the experimental data. A similar fitting method was applied here as for the XRD data. The refined values from the Vinet EoS are  $V_0 = 14.49(2) \text{ \AA}^3/\text{atom}$ ,  $B_0 = 304(1) \text{ GPa}$  and  $B'_0 = 4.6(2)$ .

EoS parameters are compared by pressure range, and EoS type in **Table 6**. There is no appreciable difference between the quality of the fit or the resulting parameters between the two EoS forms, except in the case of the 2<sup>nd</sup> order equations in the hydrostatic domain. Hydrostatic data is preferred for EoS determination, but the total compression in this range is only ~3%, which is inadequate to define the parameters of a 3<sup>rd</sup> order EoS. The hydrostatic data fits an unreasonably stiff model at high pressures, **Figure 7a**. Finally, the difference between observed and predicted pressure shows a random distribution as can be seen in the difference plot of **Figure 7b**. As expected the spread in the data under hydrostatic conditions is considerably lower than that at higher pressures. At low pressures the difference is less than 0.4 GPa, while over the entire pressure range the spread is four times greater.



**Table 6.** Summary of EoS parameters for experimental hydrostatic and nonhydrostatic pressure ranges, and the theoretical compression curve using the Vinet and Birch-Murnaghan equation of state with all parameters free and with the bulk modulus fixed at the ultrasonic result, 288 GPa<sup>28</sup>.

EoS Type	Vinet 2	BM 2	Vinet 3	BM 3	Vinet 3	BM 3	Vinet 3	BM 3	Vinet 3	BM 3
Max Pressure	10 GPa (XRD)		10 GPa (XRD)		67 GPa (XRD)		67 GPa (US+XRD)		273 GPa (DFT)	
$V_0$	14.301(4)	14.305(4)	14.307(7)	14.307(7)	14.310(4)	14.309(4)	14.320(2)	14.320(2)	14.49(1)	14.48(2)
$B_0$	333(8)	321(8)	310(30)	310(30)	309(7)	309(7)	288	288	304(1)	314(2)
$B'_0$	-	-	6(6)	6(6)	4.7(4)	4.6(4)	5.9(2)	5.8(2)	4.57(2)	4.18(3)

1 There are a number of factors that need to be taken into consideration when evaluating our equation  
2 of state for technetium. First, analysis of the two pressure ranges offers different interpretations  
3 for the compressibility of technetium with the hydrostatic range indicating that the bulk modulus  
4 is greater than 320 GPa, while the nonhydrostatic data suggest that it is less than 310 GPa. While  
5 a larger pressure range alone does not automatically improve the equation of state, it is necessary  
6 to achieve a sufficiently large compression in order to estimate the bulk modulus and begin to  
7 refine higher order parameters. The pressure range achieved in the diffraction experiment under  
8 hydrostatic conditions resulted in a compression of ~3%, while the maximum compression for the  
9 experiment was ~15%. The conflict between the need for larger compression and hydrostatic  
10 conditions is a challenge for incompressible material such as technetium.

11 Over the years, bulk moduli of most elements, including technetium, have been repeatedly revised,  
12 reflecting the challenges associated with these measurements. The selection listed in **Table 7** is  
13 representative of recent work on technetium. The consensus is that the bulk modulus is just under  
14 300 GPa. In this study a compression curve was produced from DFT methods, which when fit to  
15 an equation of state agrees well with the diffraction data. Previously, using the same GGA/PW91  
16 methodology, the bulk modulus was reported to be 298 GPa<sup>27</sup>. The difference between these is due  
17 to the previous work making a determination via elastic constants, while the more recent is a fitting  
18 of the structural evolution.

**Table 7.** Comparison of  $B_o$  and  $B'_o$  of technetium

$B_o$ (GPa)	$B'_o$	Method <sup>c</sup>	Reference
288		Ultrasonic (E)	Love <i>et al.</i> (Ref. <sup>28</sup> )
281		Phonon Dispersion Curves (E)	Guillermet and Grimvall (Ref. <sup>25</sup> )
296.3		Pseudopotentials (C)	Baria <i>et al.</i> (Ref. <sup>104</sup> )
297		Muffin-tin Orbital Theory (C)	Walzer (Ref. <sup>24</sup> )
295		Metallic Electron-Gas Model (C)	Wojciechowski (Ref. <sup>26</sup> )
298		GGA/PW91 (C)	Weck <i>et al.</i> (Ref. <sup>27</sup> )
304(1) <sup>a</sup>	4.6(2) <sup>a</sup>	GGA/PW9 (273 GPa) <sup>b</sup> (C)	Current Work
309(7) <sup>a</sup>	4.7(4) <sup>a</sup>	XRD (67 GPa) <sup>b</sup> (E)	Current Work
288 <sup>d</sup>	5.9(2) <sup>a</sup>	US+XRD (67 GPa) <sup>b</sup> (E)	Current Work

<sup>a</sup> The value in parenthesis presents the uncertainty.

<sup>b</sup> The value in parenthesis represents the maximum pressure

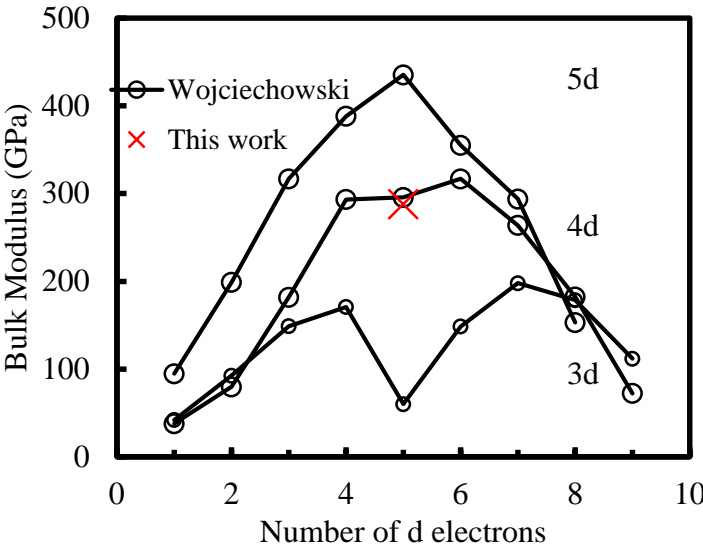
<sup>c</sup> The letters (E) and (C) denote experimental and computational methods

<sup>d</sup> Fixed to value determined by ultrasonic measurement

19 At ambient conditions, rhenium and technetium are isostructural and rhenium is commonly used  
20 as a nonradioactive technetium homolog that can provide valuable insights on the behavior of  
21 technetium. The equation of state of rhenium has been extensively studied by X-ray diffraction up  
22 to the highest achievable static pressures<sup>16</sup> and nevertheless disagreement in the EoS parameters  
23 persists.<sup>23</sup> The effects of non-hydrostatic compression on EoS parameters are widely debated in  
24 the high pressure community and the need for an accurate description of the stress state of the  
25 sample and pressure gauge is paramount to reliable pressure determination. Experimental results  
26 for rhenium from ultrasonic, Hugoniot, and isothermal data agree that the room temperature bulk  
27 modulus is 350-376 GPa,<sup>14,16,18,19,21,23,119–121</sup> with a greater spread in the first pressure derivative  
28 values. For both metals, a range of values has been established without an unambiguous solution.  
29 It is clear that the similarities between rhenium and technetium hold true at extreme conditions and

30 that their compression behaviors are sensitive to stress conditions, sample preparation, and  
31 diagnostic technique. The differences seen in EoS parameters for technetium are therefore not  
32 surprising and within expectation.

33 An accurate determination of the bulk modulus of technetium will solidify our understanding of  
34 the trends describing the 4d transition metals. The bulk moduli of the transition metals are plotted  
35 against the number of d electrons in **Figure 9**. Manganese,  $3d^5$ , represents a minimum in the bulk  
36 moduli. This minimum is not seen in rhenium for the 5d metals and is suggested to be at technetium  
37 for the 4d metals. Theoretical studies of the transition metals<sup>24,26,104</sup> suggest that the half-filled d-  
38 shell corresponds to a softening for the 4d to a smaller degree than what is seen in the 3d metals.



39 The nonhydrostatic X-ray data suggest that this effect is smaller than previously estimated, while  
40 the combined data suggest the opposite, that the effect is stronger.

## 41 Conclusion

42 In this chapter, the analysis of the equation-of-state for technetium has been performed by  
43 combining our X-ray diffraction data and DFT calculations with previously reported ultrasonic  
44 measurements. Using a variety of fitting procedures, three equations of state were compared for  
45 technetium. The EOS refined from only the diffraction data yielded the best match to theory but  
46 the fit using the ultrasonic bulk moduli and refining the pressure derivative gives the best  
47 representation of the physical behavior of technetium metal,  $B_{us} = 288$  GPa and  $B'_o = 5.9(2)$ . We  
48 have confirmed that the HCP phase is stable up to 67 GPa. Nonhydrostatic behavior is observed  
49 at high pressures, but did not prevent a quality fit from being obtained for the equation of state, as  
50 is evident from the low average difference in the calculated pressure. This equation of state is  
51 considered a reliable description of technetium compression behavior within the bounds reported  
52 here. To further our understanding of the pressure-dependent behavior of technetium and periodic  
53 trends of transition metals it would be beneficial to investigate the effects of temperature and  
54 pressure on the structural properties of technetium under hydrostatic conditions up to higher  
55 pressures.

# Equation of state of

## Technetium Metal up to 1.5 Mbar

### Introduction

The sample environment in a DAC experiment is nearly impossible to reproduce. Researchers have developed laboratory procedures to ensure the highest level of reproducibility between experiments. Due to the extreme nature of high pressure experiments, it can be seen in numerous reports of equations of state for simple metals that the community has not overcome this challenge. For example, in the case of rhenium metal, reports of the bulk moduli range from 342 – 372 GPa with the pressure derivative ranging from 3.9 to 6.2.<sup>16,23,122</sup> It is unlikely that these discrepancies are due to sample purity or systematic deviation of experimental methods. Instead, the most probable explanation is that the pressure environment experienced by our sample is complex in nature and cannot be reliably described by a single experiment. The variance of pressure scales is a known source of deviation between experiments. Rigorous experimental treatment of pressure standards has been conducted for ruby<sup>73,123,124</sup> and several metals including gold,<sup>125–127</sup> copper<sup>128,129</sup> and platinum.<sup>126</sup> The use of the same pressure standards between experiments can help guarantee that the pressure is reliably determined.

In order to better compare the results from two DAC experiments, the sample strain can be analyzed as a function of pressure. This is particularly useful when deliberately altering the stress state of the sample by making measurement in different pressure mediums. To improve upon the

initial determination of the equation of state for technetium metal, compression data was obtained using a neon pressure transmitting medium. Neon, with a bulk modulus of  $B = 9.7$  GPa, solidifies at 12 GPa and remains quasi hydrostatic until 40 GPa. This is a considerable improvement over MeOH-EtOH which has a hydrostatic limit of 11 GPa. Two compression experiments were performed achieving maximum pressures of 92 GPa and 153 GPa. Six reflections belonging to the sample were identified in the region of  $2\theta = 8^\circ - 24^\circ$ . At each pressure, seven peaks were observed which index to gold. The sample pressure was determined using the EoS parameters recommended by Takemura and Dewaele's,<sup>115</sup>  $B_o = 167$  GPa, and  $B'_o = 5.9(1)$ . The pressure-volume data for Runs 1-3 are included in **Figure 10**. Run 1 is the compression data described in the previous section and Runs 2 and 3 correspond to the compressions in neon with maximum pressures of 92 and 153 GPa respectively.

## ■ Methods

Technetium-99 metal was synthesized as polycrystalline aggregates in the radiochemistry laboratory at UNLV as previously described.<sup>105</sup> LLNL membrane DACs configured with rhenium gaskets and loaded with neon gas were used in each run. Tungsten carbide seats with slot openings were used for each side with standard brilliant cut diamonds having 300/150  $\mu\text{m}$  culets. A grain of technetium approximately 8  $\mu\text{m}$  thick was loaded into a 50  $\mu\text{m}$  diameter hole in a rhenium gasket with copper (Alfa Aesar 99.8% pure). A high pressure gas loading system was used to load compressed neon as the pressure transmitting medium. The sample and pressure standard were placed approximately 10  $\mu\text{m}$  apart. Using a micro-focused beam of less than 10  $\mu\text{m}$ , diffraction patterns of the standard were collected independently of the sample.

Angular-dispersive X-ray powder diffraction data of technetium and gold in a diamond-anvil cell was obtained at beamlines 16-ID-B of the High Pressure Collaborative Access Team (HPCAT) at the Advanced Photon Source (APS). In order to prevent dispersal of radioactive material in the case of diamond failure, mylar windows were added to the DAC containment. Diffraction patterns were collected with a MAR345 image plate with incident monochromatic beam of 29.200 keV X-rays. The sample to detector distances were calibrated with CeO<sub>2</sub> (SRM 674b), then the two-dimensional images were integrated and corrected for distortions using FIT2D.<sup>82</sup> Rietveld refinements were performed using Topaz4.2.

## ■ Results & Discussion

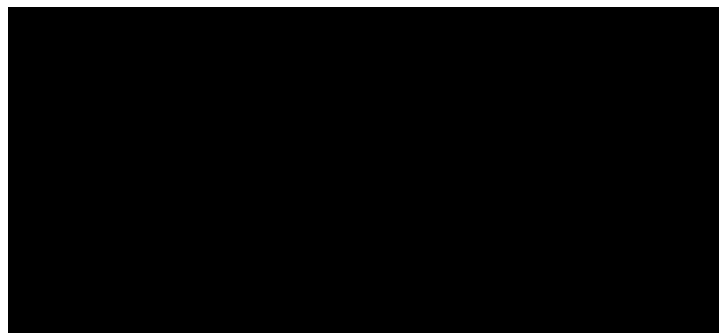
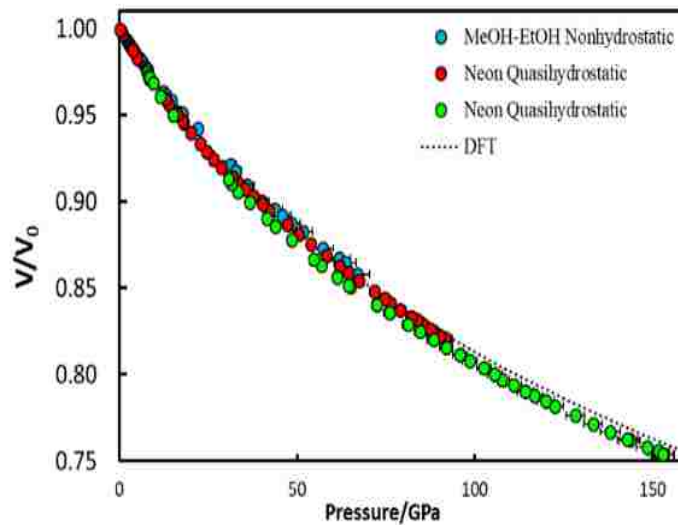
The pressure-volume data is shown in **Figure 10** and the axial ratio,  $c/a$ , is shown in **Figure 11**. In the first run a maximum compression of 0.83 was reached at 92 GPa, and 0.75 was achieved at 151 GPa. The axial ratio of  $c/a$  decreases in each run while in Run 2 the distortion grows at a more rapid rate than seen in Runs 1 and 3. Multiple approaches are used in the equation of state fitting are used to compare each experiment in order to address previous data and varied experimental conditions.

Using the 3<sup>rd</sup> order Birch-Murnaghan and Vinet equations of state the data from run 2 and 3 are fit. Due to incompleteness at low pressure it is not appropriate to compare fits of the low pressure range to the full range, as was done for the first experiment described in the first section of this chapter. Therefore, the full range was used for each fitting. Fixing the bulk modulus to the value determined from ultrasonic measurements was considered in the refinement. In the case of runs 2 and 3 this did not yield a quality fit. In all the fitting procedures, the initial volume was fixed using

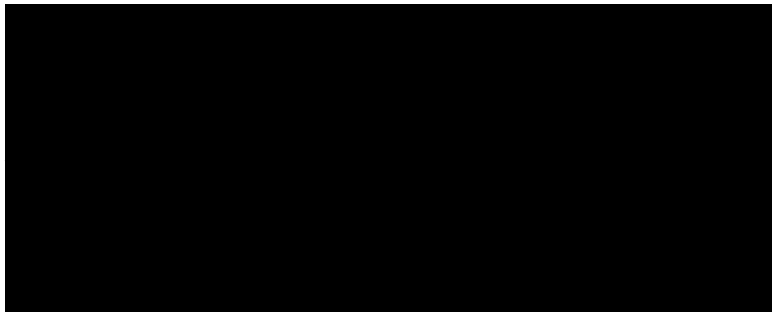
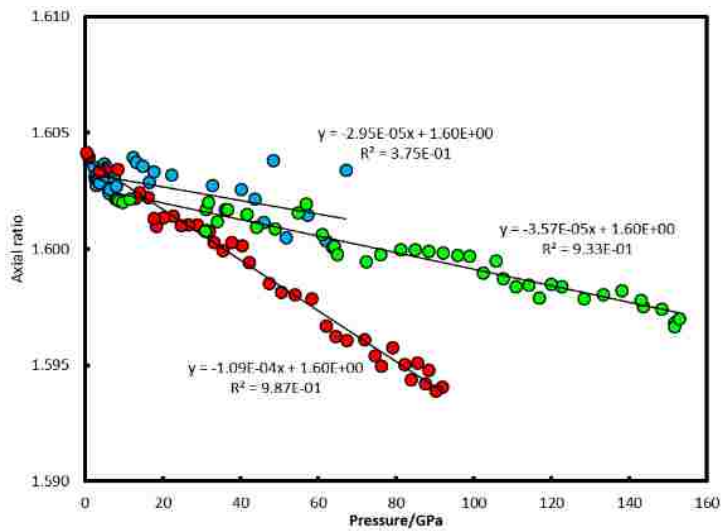


the reported value from Chapter 3,  $V_0 = 14.3119(3) \text{ \AA}^3/\text{atom}$ . For Run 2 this resulted in  $B_0 = 281(3)$  GPa and  $B'_0 = 5.3(2)$  for the Birch-Murnaghan equation, and  $B_0 = 279(3)$  GPa and  $B'_0 = 5.5(2)$  for the Vinet equation, with  $\chi^2$  values of 0.53 and 0.50 respectively. For run 3 this resulted in  $B_0 = 268(3)$  GPa and  $B'_0 = 5.0(1)$  for the Birch- Murnaghan, equation and  $B_0 = 266(4)$  GPa and  $B'_0 = 5.3(1)$  for the Vinet equation. with  $\chi^2$  values of 0.30 and 0.29 respectively. The results of the fitting the Vinet EOS consistently gave better results, and these are compared in **Table 8**.

The effects of non-hydrostatic pressure was discussed in the previous section regarding a pressure transmitting medium of MeOH:EtOH. Using an inert gas such as neon delays the onset on these deviatoric stresses on the sample and can suppress the effects observed in the resulting diffraction patterns. With increasing pressure, the diffraction peaks broaden, which is a symptom of increasing



micro-stress. The effects of the macroscopic non-hydrostatic stresses are different from micro-stress and will both be qualitatively described for each run. While neon is a superior at reducing the effects of this behavior it is impossible to eliminate this behavior when in excess of the hydrostatic limit of the pressure transmitting medium.

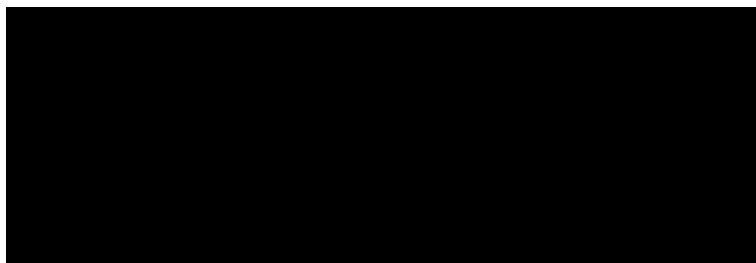
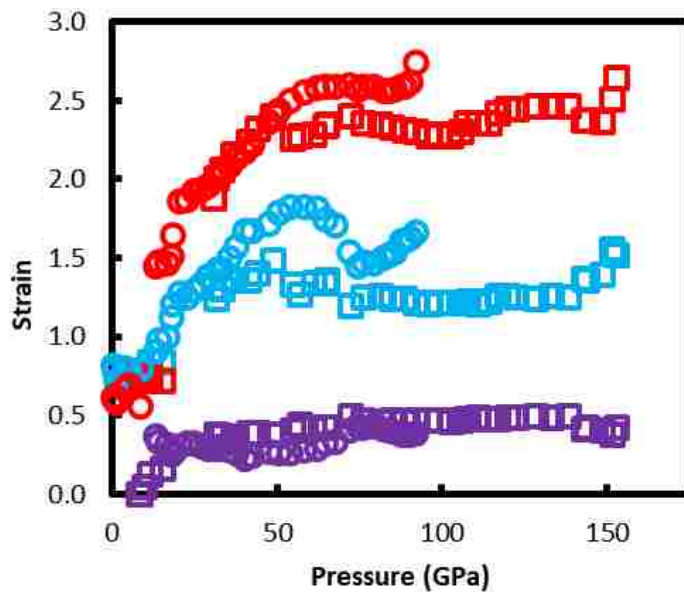


The macroscopic stress due to non-hydrostatic pressure affects the d-spacing of each specific *hkl* as related to the directional distribution of the forces. The difference in the d-spacing calculated from whole pattern fitting and from individual peak fitting provides information about the relative degree the effect of non-hydrostatic pressures has on the compression of the material. In **Tables 9-11** the difference in d-spacing at the highest pressure is calculated for each *hkl* from Runs 1-3 respectively. The change in the average deviation from the lowest pressure obtained in each run is

**Table 8.** Vinet EOS Parameter summary

Run	1	2	3
PMT	MeOH-EtOH	Neon	Neon
$P_{\max}$ (GPa)	67	92	153
$K_0$ (GPa)	308 (4)	279 (3)	266 (3)
$\partial K/\partial P$	4.8 (3)	5.5 (2)	5.3 (1)
Chi <sup>2</sup>	0.310	0.525	0.294
Max Delta P	1.3 GPa	1.5 GPa	1.5 GPa

reported in these tables. For run 1, the difference was 0.14% at 62 GPa which was 9 times larger than at 2 GPa. Compared to Run 3, which had a difference of 0.13% at 153 GPa, there is a comparable amount of deviation due to non-hydrostatic pressure at their maximum pressures, respectively. However, in Run 2 the difference is already 0.11% at 92 GPa.



In the Rietveld refinement, the fundamental parameter approach is used to determine the sample strain from the peak shape, refer to the TOPAS technical manual for details of the microstructure convolutions. In **Figure 12**, the refined strain parameter for technetium and gold, as well as the difference between the two is plotted. Three important strain domains are 0 - 15 GPa, 15 – 40 GPa and above 50 GPa. Below 20 GPa there is little measurable strain as expected in neon. As pressure increases from ~15 - 40 GPa the strain parameters increase. Above 50 GPa the strain remains mostly constant at ~2.3 GPa for technetium and ~1.3 GPa for gold. If only the difference between technetium and gold is considered, the strain parameter for Run 2 is constant and for Run 3 is constant after 30 GPa. The amount of strain present in Run 2 suggests that it is less precise than Run 3 and that a nonhydrostatic correction may be applicable.

**Table 9.** Run 1 at 62 GPa the average difference in the measured d-spacing and calculated is 0.14%, which is 9 times greater than at 2 GPa.

hkl	$d_m$ (Å)	$d_{calc}$ (Å)	$d_m - d_{calc}$
103	1.1854	1.1827	0.0028
110	1.3036	1.3038	-0.0002
102	1.5334	1.5309	0.0025
101	1.9860	1.9852	0.0008
002	2.0795	2.0824	-0.0029
100	2.2520	2.2583	-0.0063

**Table 11.** Run 2 at 92 GPa the average difference in the measured d-spacing and calculated is 0.11%, which is 6 times greater than at 0.8 GPa.

hkl	$d_m$ (Å)	$d_{calc}$ (Å)	$d_m - d_{calc}$
103	1.1653	1.1650	0.0003
110	1.2831	1.2861	-0.0030
102	1.5064	1.5085	-0.0022
101	1.9567	1.9573	-0.0006
002	2.0521	2.0502	0.0019
100	2.2242	2.2276	-0.0033

**Table 10.** Run 3 at 153 GPa the average difference in the measured d-spacing and calculated is 0.13%, which is 5 times greater than at 8 GPa.

hkl	$d_m$ (Å)	$d_{calc}$ (Å)	$d_m - d_{calc}$
103	1.1309	1.1332	-0.0023
110	1.2455	1.2496	-0.0041
102	1.4662	1.4670	-0.0008
101	1.9016	1.9025	-0.0009
002	1.9971	1.9952	0.0019
100	2.1635	2.1643	-0.0008

## ■ Conclusion

The work in the chapter expands our understanding of the behavior of technetium by increasing the maximum achieved pressure at room temperature, resulting in a new determination of the equation of state. Diffraction data at high pressure of technetium metal has been collected up to 151 GPa using neon as the pressure transmitting medium. The single hexagonal phase is stable up to the highest achieved pressure. Like rhenium metal, when compressed, the axial ratio for technetium decreases slightly. The equation of state has been determined from each of the three available data sets taking into consideration independent sample conditions due to the unique strain environment achieved in diamond anvil cell experiments. Multiple pressure ranges were fit to best reflect the strain profile of the compression experiments. Based on the strain analysis, quality of fit, and maximum pressure reached, it is determined that the most representative equation of state for technetium metal is  $V_0 = 14.3119(3) \text{ \AA}^3/\text{atom}$ ,  $B_0 = 266(4) \text{ GPa}$  and  $B' = 5.3(1)$ .

By combining the individual equation of state parameters for the structural response to high pressure and high temperature, it is possible to estimate the behavior of technetium metal under high pressure/high temperature conditions. This lays the ground work for probing the effect of pressure on the melting behavior of technetium metal and determination of the full high pressure-thermal equation of state.

The exploration of novel synthesis at high pressure utilizing laser heating techniques starting from technetium metal is accessible from this foundation of knowledge. Considering the work from several sources<sup>27,130–132</sup> predicting stable phases of  $\text{Tc}_x\text{N}_y$  and the lack of reproducible experimental evidence for the existence of any technetium nitride<sup>94</sup>, it is plausible that high

pressures are necessary for the synthesis of these materials. In addition to nitrides, high pressure synthesis is also likely to lead to the discovery of new compounds or phases of previously confirmed technetium containing materials. Of particular interest to the nuclear/materials science community would be the borides and carbides for their potential as superhard materials with superior mechanical and thermal properties.

Further exploration of the high pressure behavior of technetium metal could lead to revisiting the pressure dependence of the superconducting transition temperature that was previously reported up to a maximum pressure of 2.5 GPa.<sup>30</sup>

# High Pressure Phase

## Diagram of Transition Metal Dioxides

In this chapter the high-pressure phase diagrams of several transition metal dioxides are explored including molybdenum dioxide, rhenium dioxide and technetium dioxide. The equation of state is determined for each of the known phases that are stable at ambient conditions. A new phase of molybdenum dioxide is identified at high pressure and recovered to ambient conditions.

### Introduction of transition metal dioxides

The elements belonging to the sixth and seventh group of the periodic table form compounds in many oxidation states. In the +IV oxidation state the second and third row elements of these groups form oxides with the same structure type. The MoO<sub>2</sub> structure-type was identified by Magneli in the P2<sub>1</sub>/c space group. The structure consists of chains distorted metal centered octahedral along the *a*-axis. The chains are connected by corner sharing sites at each octahedral. metal-metal distances in the octahedral chain alternate long and short. Magneli identified this as metal-metal bonding.

It has been calculated that for five structures previously reported to form in other dioxide systems that there is less than 0.2 meV difference between the MoO<sub>2</sub> ambient structure and the suggested structures.<sup>47</sup> These five structures are candidate structures for meta-stable phases of MoO<sub>2</sub> that could be obtained with the application of pressure/temperature. In the year following this report, a



high pressure phase of MoO<sub>2</sub> was synthesized at 18 GPa and 1073 K.<sup>48</sup> A structure solution from single crystal diffraction on the recovered sample matched a structure previously found at high pressure for WO<sub>2</sub> in the space group *Pnma*. This phase will be referred to as  $\beta$ -MoO<sub>2</sub> throughout this chapter. Density functional theory was used to calculate enthalpies for the  $\alpha$ - and  $\beta$ -phases determined that the  $\beta$ -phase is stable above 6 GPa and slightly meta-stable at ambient pressure. It was also determined that the rutile structure of MoO<sub>2</sub> is the most stable above 28 GPa. At ambient conditions the MoO<sub>2</sub> structure-type is the most commonly found phase of ReO<sub>2</sub>. This phase will undergo an irreversible phase transition to the  $\alpha$ -PbO<sub>2</sub> structure-type above 300 °C and is stable up to 1050°C. There is a third phase of ReO<sub>2</sub> that crystallizes in the rutile structure-type and was first discovered via an alternative synthetic route.<sup>60</sup> Technetium dioxide is the sole remaining dioxide in this grouping where the MoO<sub>2</sub>-phase is the only known phase. For all the metals the MoO<sub>2</sub>-phase is the ambient structure.

In order to expand the known phase space of transition metal dioxides the three dioxides of molybdenum, technetium and rhenium are compressed.

## ■ Experimental Methods

*Caution:* Technetium-99 is a weak beta emitter ( $E_{\text{max}} = 293$  keV). All manipulations were performed in a radiochemistry laboratory at UNLV designed for chemical synthesis using efficient HEPA-filtered fume hoods, and following locally approved radioisotope handling and monitoring procedures.

Tchnetium-99 dioxide was prepared in the radiochemistry laboratory at UNLV as previously described<sup>44</sup>

Modified BX-90<sup>75</sup> cells and four-post cells were used in these experiments. Matched pairs of conical Boehler-Almax<sup>76</sup> and standard cut diamonds were chosen. Typical diamond culets measured 300  $\mu\text{m}$ , while 450  $\mu\text{m}$  culets were used for the lower pressure experiments. In each case sample powder was loaded in the center of a 100–200  $\mu\text{m}$  diameter hole in a rhenium gasket with a 10  $\mu\text{m}$  thick flake of gold (Alfa Aesar 99.8% pure). For  $\text{MoO}_2$  and  $\text{ReO}_2$  neon was used for a pressure-transmitting medium<sup>133</sup>, while 4:1 MeOH-EtOH was used with  $\text{TcO}_2$  in consideration of safety. The sample and pressure standard were placed at least 15  $\mu\text{m}$  apart. Ruby sphere of less than 20  $\mu\text{m}$  were used with all nonradioactive samples as a secondary pressure standard. Using a microfocused X-ray beam of less than 15  $\mu\text{m}$ , diffraction patterns of the standard were collected independently of the sample. The first experiment, Run 1 for  $\text{ReO}_2$ , was collected at beamline 12.2.2 of the Advanced Light Source, (ALS). All other angular-dispersive X-ray powder diffraction data were obtained at beamlines 16-IDB and 16-BM-D of the High Pressure Collaborative Access Team (HPCAT) at the Advanced Photon Source (APS). At each beamline, diffraction patterns were collected with a MAR345 image plate with incident monochromatic beams whose wavelength are indicated in **Table 12**. The sample to detector distances were calibrated with  $\text{CeO}_2$  (SRM 674b) or  $\text{LaB}_6$  (SRM 660), then the two-dimensional images were integrated and corrected for distortions using FIT2D.<sup>82</sup> Rietveld refinements were performed using TOPAS4.

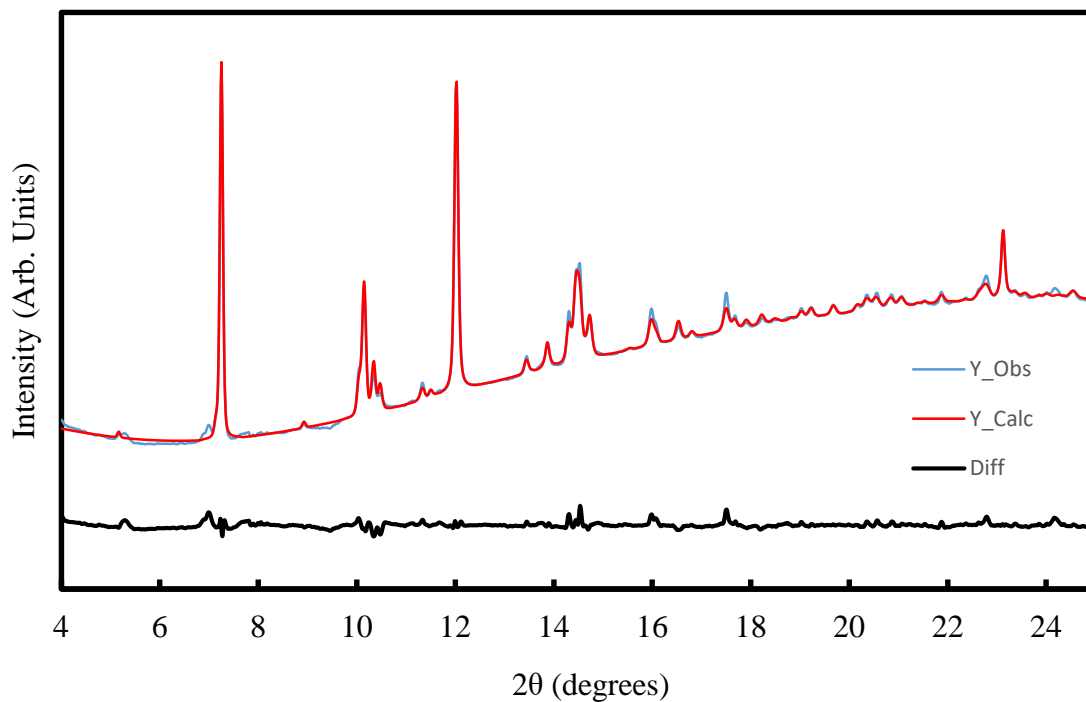
**Table 12.** X-ray energies

TcO <sub>2</sub> Run 1	MoO <sub>2</sub> Run 1	MoO <sub>2</sub> Run 2	MoO <sub>2</sub> Run 3	ReO <sub>2</sub> Run 1	ReO <sub>2</sub> Run 2	ReO <sub>2</sub> Run 3
0.406626 Å	0.413267 Å	0.424000 Å	0.373795 Å	0.413267 Å	0.424000 Å	0.373795 Å

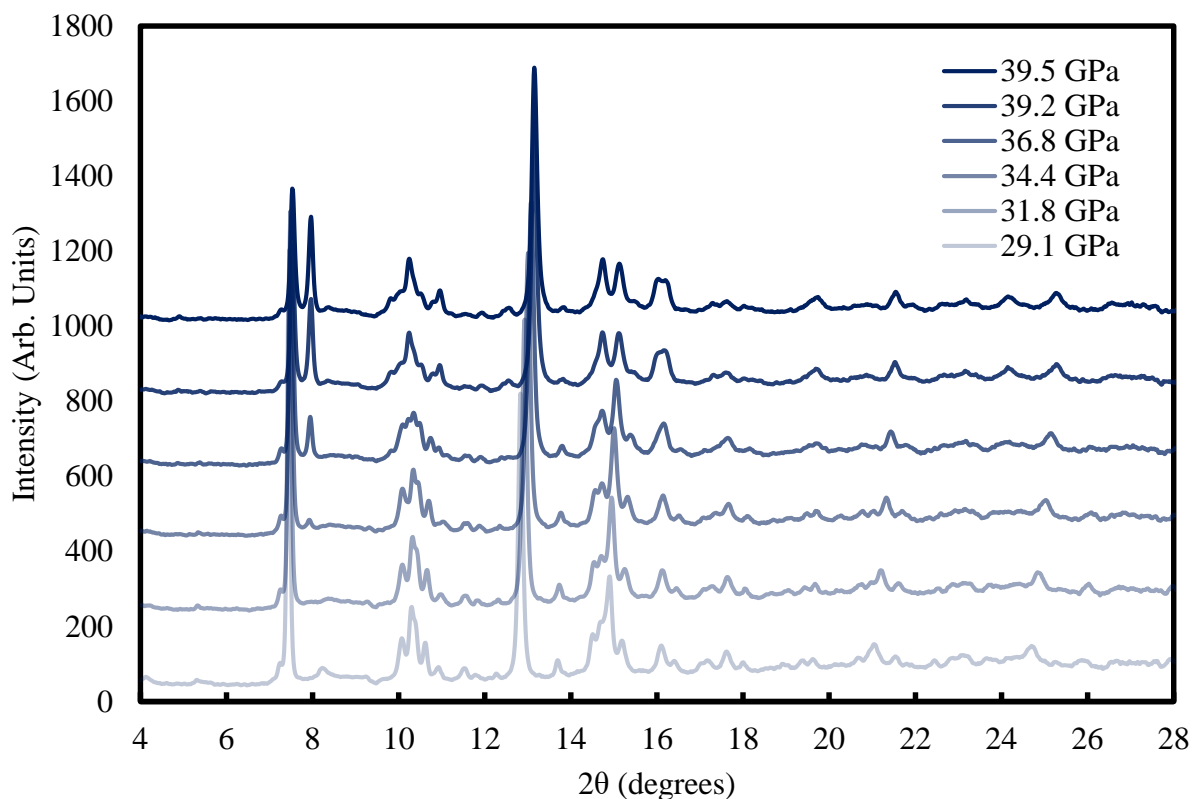
## Results & Discussion:

### Molybdenum Dioxide

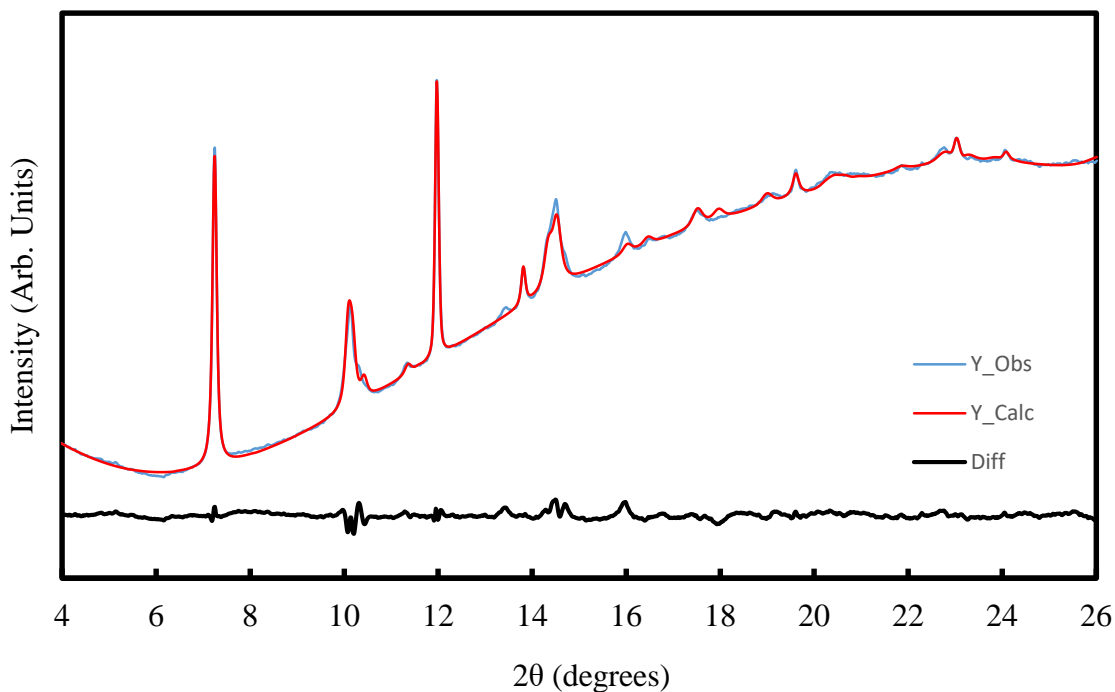
In three experimental trials, molybdenum dioxide was compressed at room temperature. Use of a neon pressure transmitting medium provided pseudohydrostatic pressure environment for



preserving quality diffraction patterns with minimal interference due to strain. In the first experiment named Run 1, a maximum pressure of 17.8 GPa was achieved which is plotted in **Figure 13**. A smooth decrease in lattice parameters was observed with the beta angle increasing slightly from  $120.78^\circ$  to  $121.64^\circ$  at 17.8 GPa. In the second experiment labeled Run 2, molybdenum dioxide was compressed to 60 GPa. The appearance of new peaks and peak splitting is observed starting at 29 GPa. Between 29 GPa and 60 GPa, there is a mixed phase system with the monoclinic and an unknown phase shown in **Figure 14**. The monoclinic phase remains present up to 32.4 GPa. Upon decompression, at 26 GPa there is an abrupt transition in which no peaks from the alpha phase or the unknown high-pressure phase remain. The new diffraction pattern can be indexed as orthorhombic. Using the  $\text{CaCl}_2$  structure-type as a starting point for the Rietveld

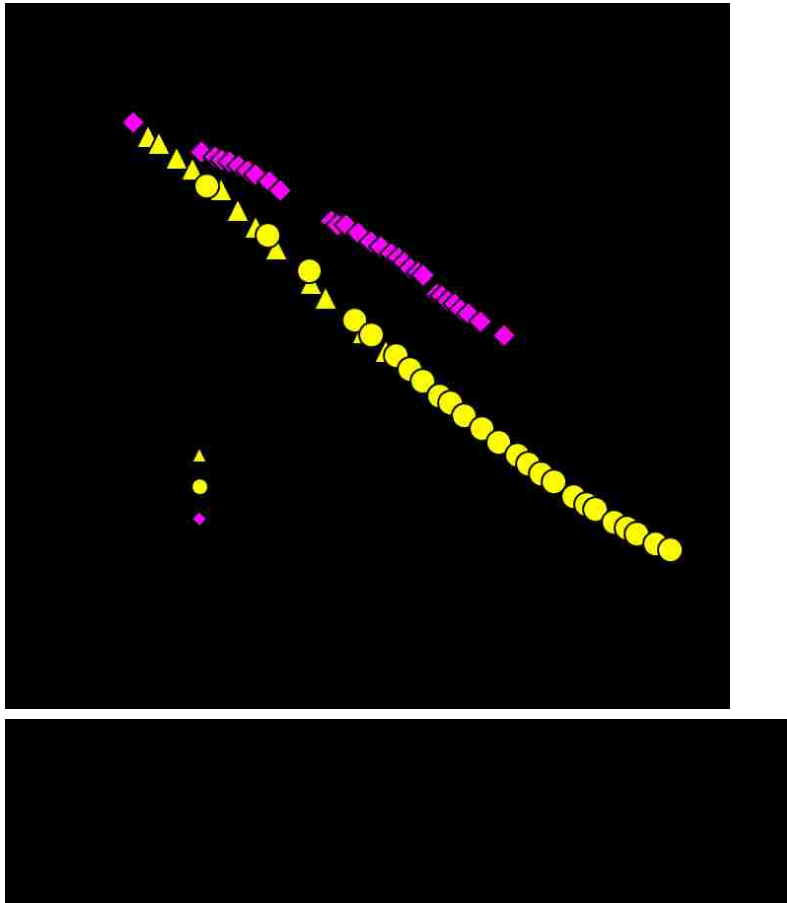


refinement there is a good match with no unidentified peaks, as seen in **Figure 15**. The  $\text{CaCl}_2$  phase (Pnm, No. 58) was recoverable to ambient pressure and compressed to 26 GPa in the same DAC using neon. The ambient pressure unit cell parameters were determined to be  $a = 4.8343(6)$  Å  $b = 4.6140(5)$  Å and  $c = 2.7763(3)$  Å with atom positions for molybdenum and oxygen of Mo: (0, 0, 0), O: (0.3237, 0.30427, 0). While decompressing to ambient pressure, sufficient contact was maintained between the diamond and the gasket to retain the pressure transmitting medium. The new phase was compressed in the same DAC to a maximum pressure of 26.1 GPa.



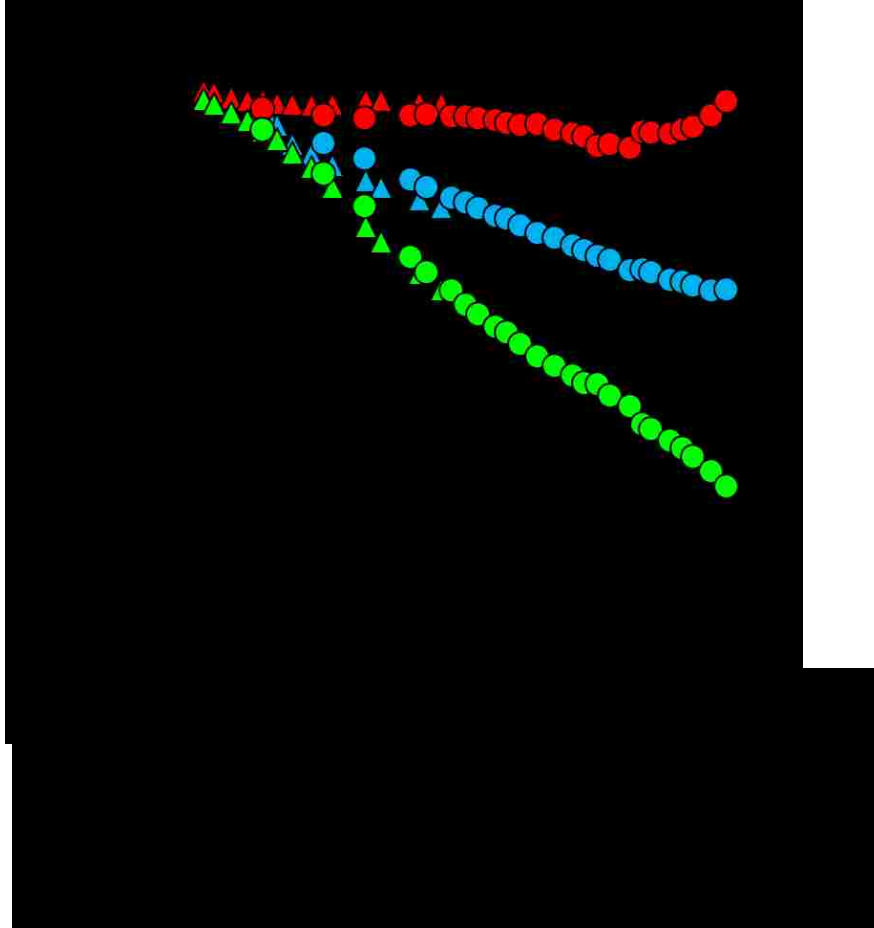
The pressure-volume data recorded in **Appendix A** was used to fit the second-order Birch-Murnaghan equation of state. A bulk modulus of 205(8) GPa was determined for  $\alpha\text{-MoO}_2$  from Run 1. For Run 2, the same fitting resulted in a bulk modulus of 180(10) GPa. By combining the data sets, a single equation of state was determined for the monoclinic phase of  $\text{MoO}_2$  where  $B_0 =$

189(3) GPa and  $B' = 4$ . The  $\text{CaCl}_2$ -phase is fitted using the same second-order Birch-Murnaghan equation of state where  $B_0 = 272(8)$  GPa. This new high-pressure phase is 43% stiffer than the ambient phase. Additionally, the new phase has a ambient pressure density of  $6.76 \text{ g/cm}^3$  compared to the monoclinic phase that has a density of  $6.46 \text{ g/cm}^3$ . The compression data is



compared by relative change in volume in **Figure 16**.

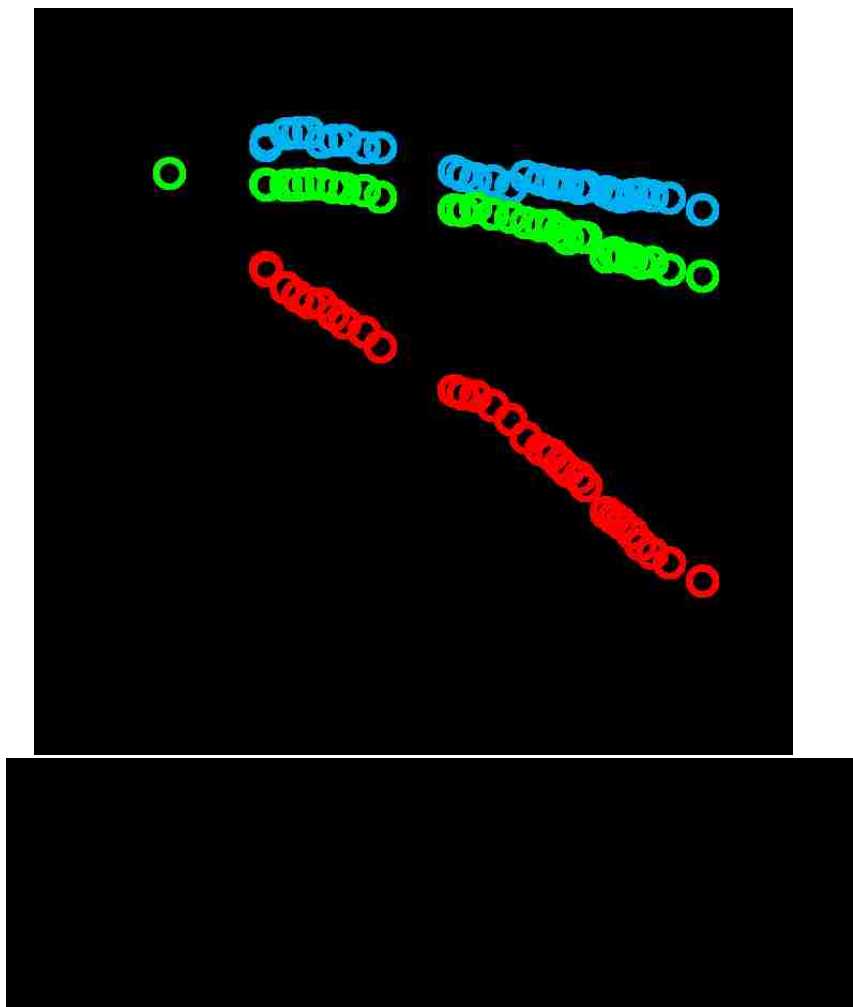
Both phases display highly anisotropic compression behavior. The change in relative lattice parameters lengths for the monoclinic phase is presented in **Figure 17**, and the  $\text{CaCl}_2$ -phase is shown in **Figure 18**. The first figure shows that the  $a$ -axis remains extremely incompressible with



a change of 0.3% at 25 GPa while the other two lattice parameters decrease by up to 5% at 25 GPa. However, even though the  $a$  lattice parameter did not decrease significantly compared to the other directions, the metal-metal distances both decreased by approximately 2.5%. The metal-metal chain is a zigzag with angles starting at 172.65 degrees and increasing to 172.84 degrees. The chain becomes straighter as pressure increases. The degree of distortion in the metal-centered octahedral decreases by approximately 0.004% over the pressure range. The internal octahedral angles, measured from O-Mo-O, can be categorized into three groups: constant, increasing and decreasing. The four angles with rates of change less than 0.03 degrees per GPa are considered to be constant. The four angles that remain constant are in the metal-metal chain. The remaining angles all have rates of change near  $\pm 0.1$  degrees per GPa. The increasing and decreasing angles are paired within the octahedral such that they become less distorted. Pressure reduces the total

degree of distortion in the octahedral but since the angles are not all approaching  $90^\circ$ , this will not lead to a symmetric octahedral.

The  $\text{CaCl}_2$  phase of  $\text{MoO}_2$  has two incompressible directions compared to the single incompressible direction in the monoclinic phase. In the O-phase the metal-metal distance decreases at approximately half the rate as that in the monoclinic phase. The initial metal-metal distance for the  $\text{CaCl}_2$ -phase is in between that of the two metal-metal distances for the monoclinic phase so the decreased compressibility could be due to an average increase in metal-metal interactions given that the metals are now close enough to two other metal atoms where as in the



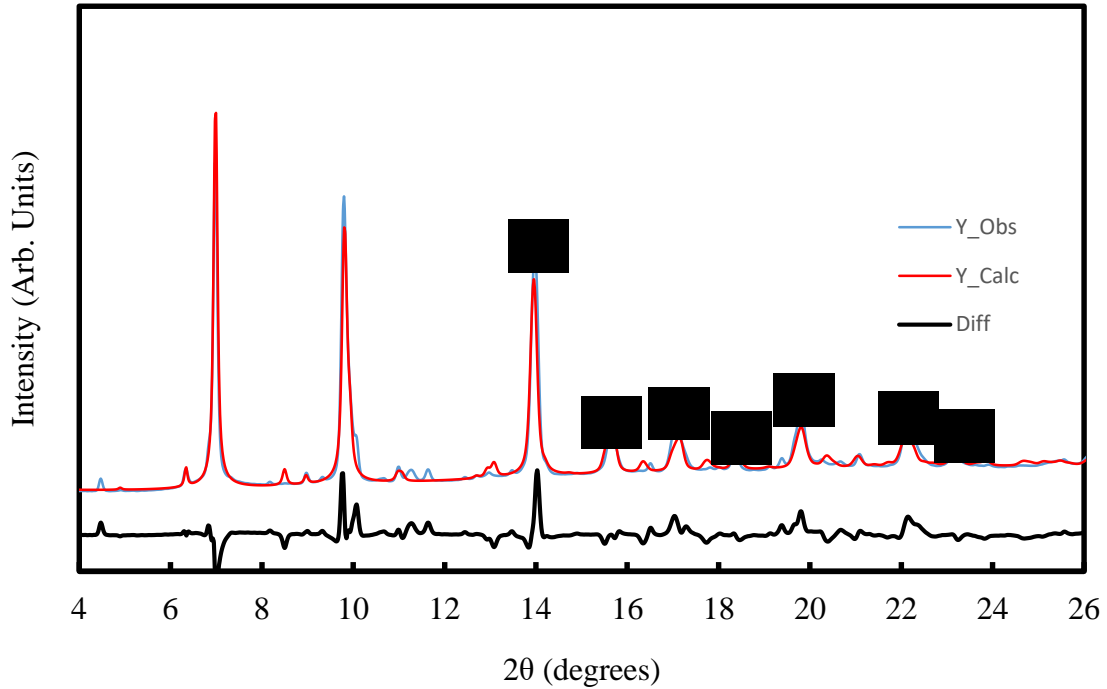


monoclinic structure there is clearly only one other metal atom that each metal atom could experience interactions with.

## ■ Rhenium Dioxide

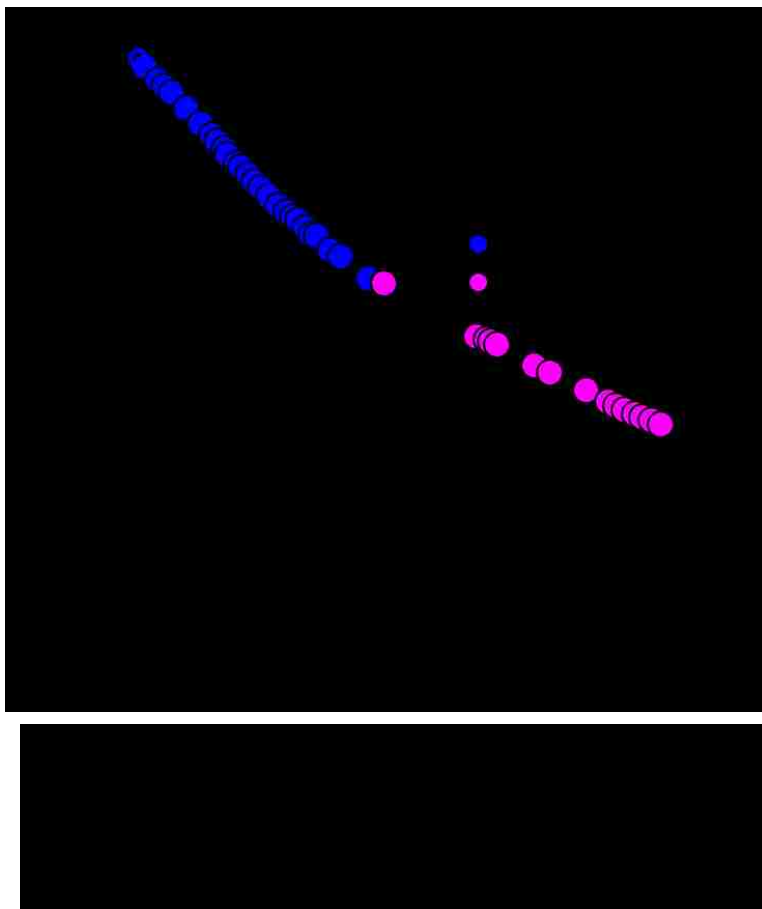
Rhenium dioxide was compressed in two experiments that had pressure ranges of 0 – 33.2 GPa and 35.5 – 75.1 GPa. Each run was performed using a neon pressure transmitting medium and gold pressure standard. As seen in the diffraction pattern from the ReO<sub>2</sub> sample **Figure 19**, there is a second minor phase present. Some of the additional peaks present can be attributed to ReO<sub>3</sub>. The  $\alpha$ -ReO<sub>2</sub> phase is stable over the entire pressure range with no peak splitting and only the expected peak broadening due to nonhydrostatic effects at higher pressures. The quality of the entire data series for ReO<sub>2</sub> suffers since the pressure ranges are not overlapping and the first pressure of the higher pressure is above 30 GPa. This was due to technical difficulties regarding the initial gas loading of the DAC and while not favorable towards collecting a fully overlapping data set it is not considered to reduce the usefulness of including the additional high-pressure data in our determination of the equation of state.

Fitting procedures were performed utilizing EOSFit7c, consistent with previously descriptions in this work. The pressure-volume data was fit using the Birch-Murnaghan 2<sup>nd</sup> order equation of state for each of the pressure ranges independently, and then fit with a 3<sup>rd</sup> order equation for the



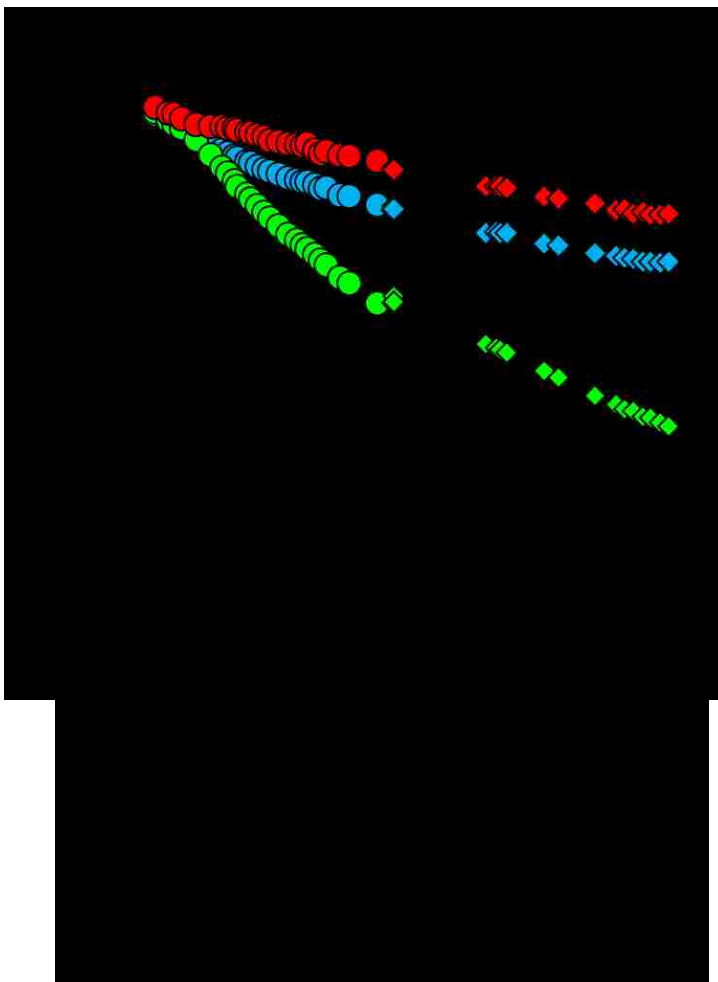
combined data set. A bulk modulus of 196(3) GPa was determined for Run 1. For Run 2, the same fit resulted in a bulk modulus of 220(20) GPa. By combining the data sets, a single equation of state was determined for the monoclinic phase of ReO<sub>2</sub> where  $B_o = 193(5)$  GPa and  $B' = 4.4(3)$ . The PV data, with the EOS fit of the combined data set is shown in **Figure 20**.

The compression behavior of  $\alpha$ -ReO<sub>2</sub> is anisotropic, but with a different response of that of when  $\alpha$ -MoO<sub>2</sub> is compressed. For  $\alpha$ -ReO<sub>2</sub>, the  $b$ -axis is the most compressible with the  $a$ -axis compressing at a rate less than twice that and the  $c$ -axis compressing less than three times that of the  $b$ -axis. The relative compression rates for each lattice direction is shown **Figure 21**. This is different from the behavior of  $\alpha$ -MoO<sub>2</sub> although we anticipated the two compounds to behave similarly.

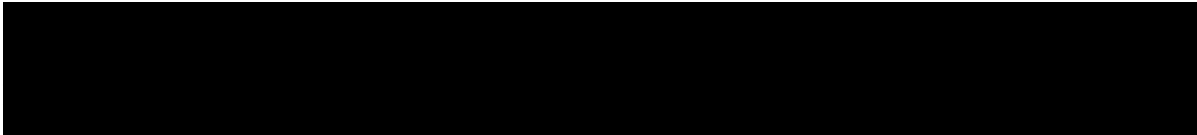
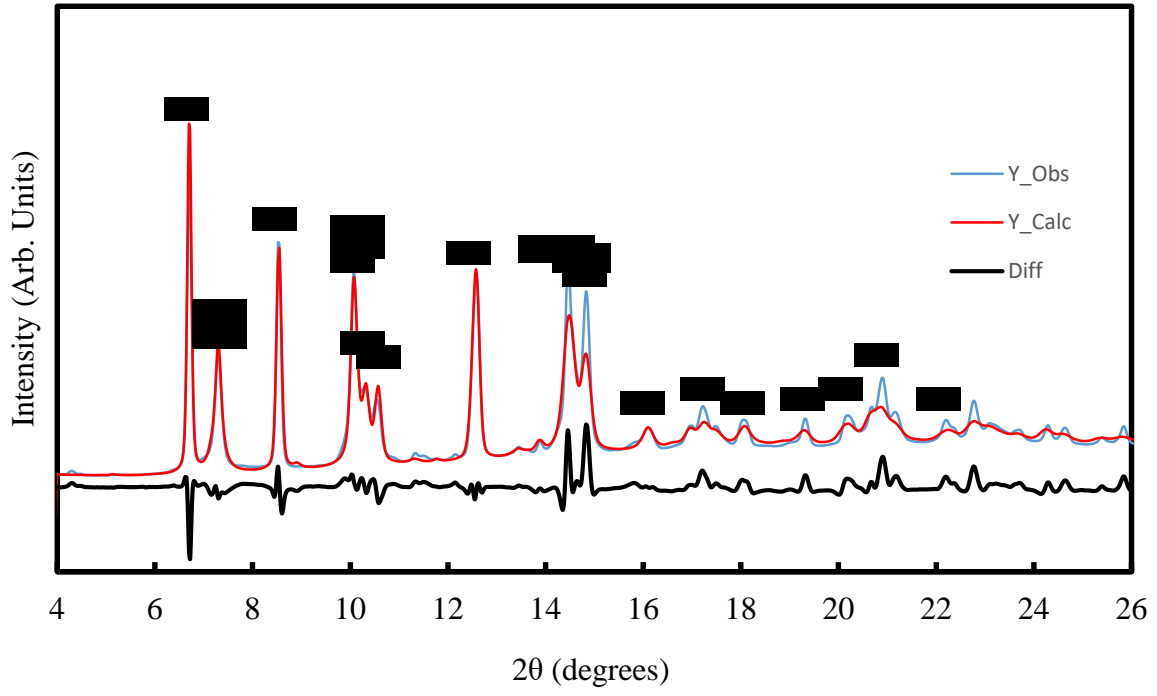


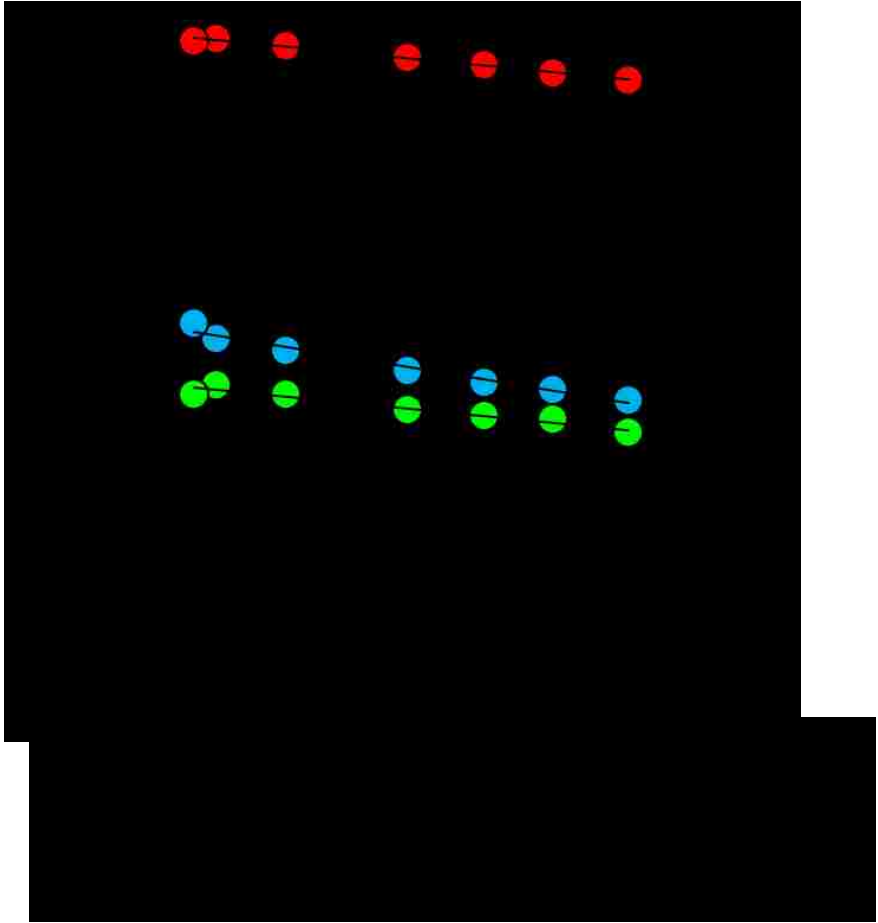
At the maximum pressure of Run 1, which was 33 GPa, the sample was heated above 1500 K using a laser heating system. This allowed for the complete conversion of the  $\alpha$ -phase into the thermodynamic ground state  $\beta$ -ReO<sub>2</sub>, **Figure 22**.

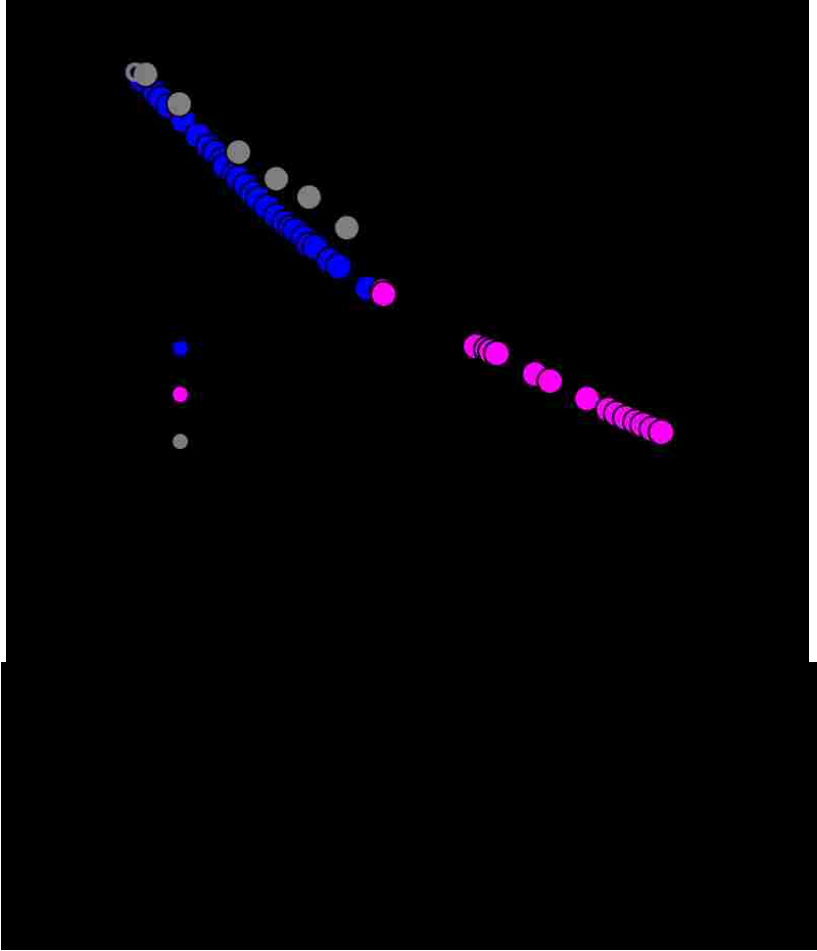
The decompression series of  $\beta$ -ReO<sub>2</sub> was completed with seven pressure points, including one at ambient pressure after releasing the pressure medium. The unit cell for the recovered sample is 0.2% larger than previously reported structure refinements. This could be due to sample strain introduced into the sample while under compression. In the orthorhombic structure, the *a*-axis is the most compressible, followed by the *c*-axis and then the *b*-axis. The change in lattice parameters observed below 30 GPa is shown in **Figure 23**



The ground state of ReO<sub>2</sub> was fit using the 2<sup>nd</sup> order Birch-Murnaghan equation of state with a bulk modulus of 260(10) GPa over the pressure range observed for the two phases, the orthorhombic phase is stiffer than the monoclinic variant. The relative compression data for each ReO<sub>2</sub> phase is plotted in **Figure 24**.

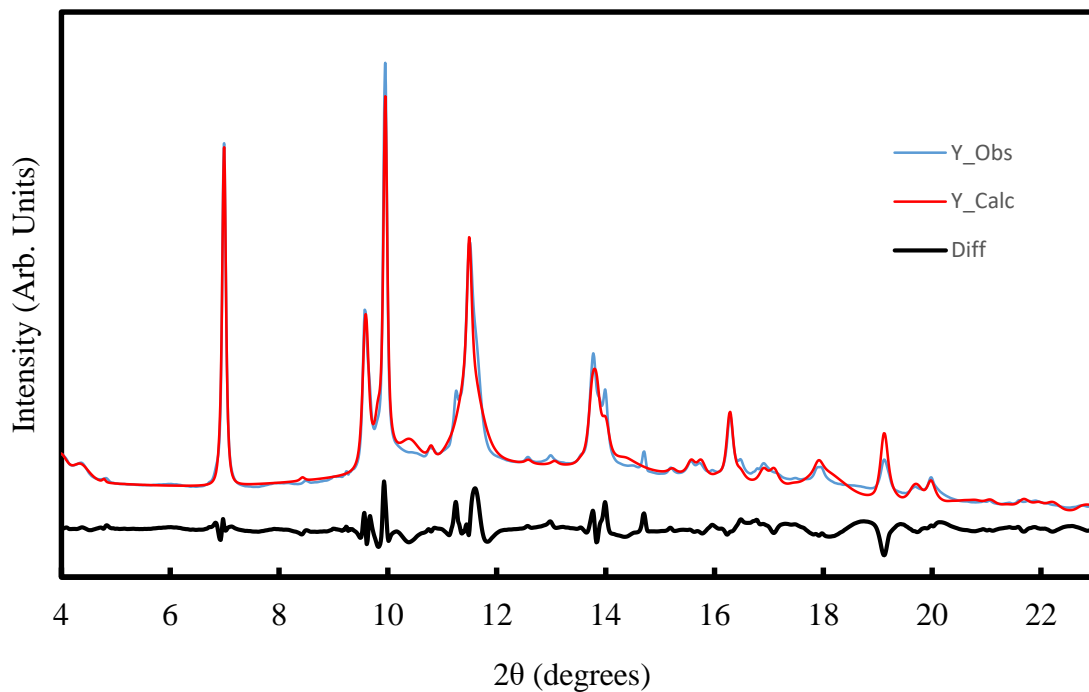




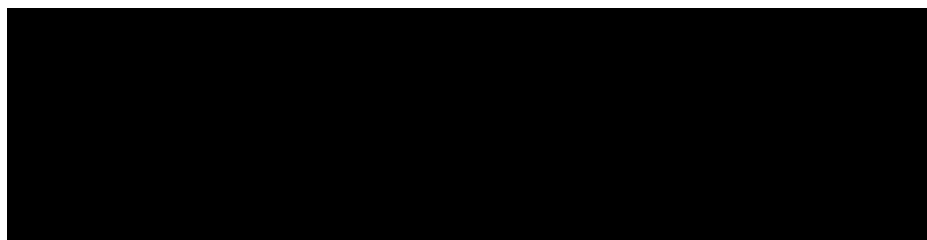
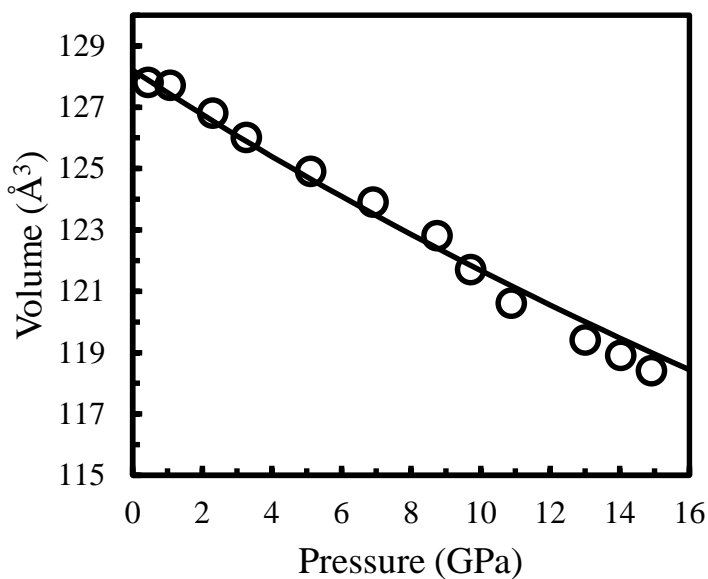


## Technetium Dioxide

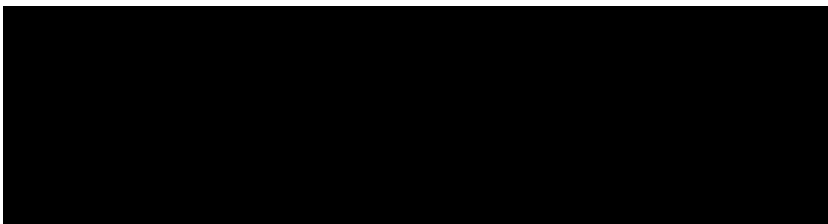
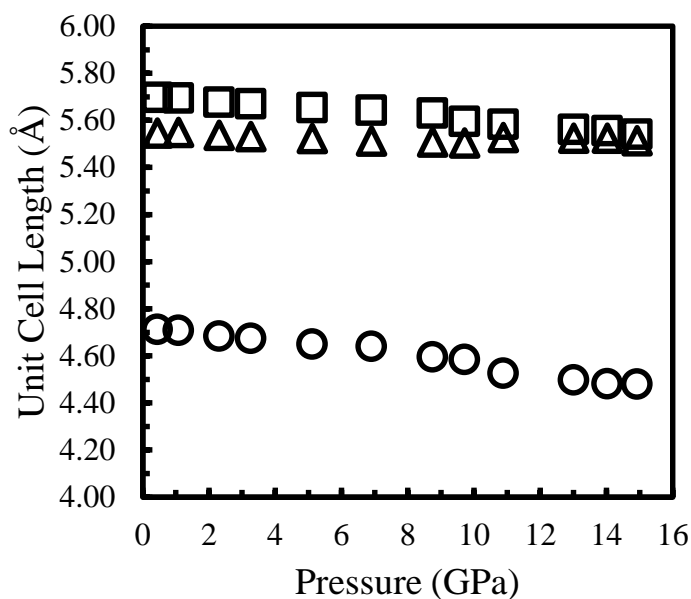
A single compression study was conducted on  $\text{TcO}_2$  to a maximum pressure of 15 GPa. Using a MeOH:EtOH pressure transmitting medium, it is expected that above the hydrostatic limit there will be significant peak broadening due to nonhydrostatic pressure. In the diffraction pattern of the monoclinic  $\text{TcO}_2$  structure, there are already peaks that are difficult to resolve under high pressure (**Figure 25**). Beyond this pressure, it was determined that the data would not be of sufficient quality to be useful. The liquid pressure medium was necessary in this experiment due to radiological concerns regarding the loading of a high-pressure gas medium.







The room temperature compression data is plotted in **Figure 26** with a 2<sup>nd</sup> order Birch-Murnaghan equation of state displayed. The bulk modulus for TcO<sub>2</sub> was determined to be  $B_0 = 172(9)$  GPa. The monoclinic structure was the only phase observed in this pressure range. As with the other monoclinic dioxides, there is anisotropic compression behavior. In the case of TcO<sub>2</sub>, it is the *c*-axis that is the least compressible, followed by the *a*-axis and then the *b*-axis. This is a similar lattice behavior to that of ReO<sub>2</sub>. The change in the lattice parameters is plotted in **Figure 27**.



## Conclusion

In this chapter, three of the monoclinic phases related to the rutile structure have been compressed. In the case of  $\text{MoO}_2$ , a multiphase region was identified at room temperature between 29 and 60 GPa. A new  $\text{MoO}_2$  phase was discovered while decompressing the sample. The  $\text{CaCl}_2$  structure type is known to be formed by  $\text{RuO}_2$  as well as four other dioxides and five halides. For  $\text{ReO}_2$  the monoclinic phase was stable up to 75 GPa. Using laser heating techniques while at 33 GPa, the monoclinic  $\text{ReO}_2$  sample was converted to the orthorhombic beta phase with the same structure as  $\alpha\text{-PbO}_2$ . The  $\beta$ -phase was then decompressed to ambient pressure. Finally,  $\text{TcO}_2$  was compressed

in a liquid medium to a maximum pressure of 15 GPa and found to be stable in the monoclinic structure up to this pressure.


When considering the volumetric compression, the monoclinic phases are all very similar with bulk moduli ranging from 172 -193 GPa. Given the structural similarities, this is not surprising. It could have been expected that the compression behaviors would follow systematic trends for the monoclinic structures. The linear bulk moduli is defined by  $B_i = \frac{-1}{x_i} \left( \frac{\partial x_i}{\partial P} \right)$  and related to the bulk modulus by  $B_o = (1/B_a + 1/B_b + 1/B_c)$ . The linear bulk moduli are useful for quantitative comparison of the compressibility of each direction of the crystal structure. A summary of the bulk moduli is compiled in **Table 13**. Of the linear bulk moduli, MoO<sub>2</sub> was found to have the most incompressible axis of the systems studied with a  $B_b = 3590$  GPa for the b-axis. In contrast, the b-axis is the most compressible for the other two systems. For ReO<sub>2</sub> and TcO<sub>2</sub>, the stiffest axis is the c-axis with linear bulk moduli of  $B_c = 1450$  GPa and  $B_c = 1100$  GPa, respectively. Based on the packing of each phase, no difference between the three metals was revealed. The chain of edge-sharing octahedra that are comprised of alternating metal-metal bonds is aligned down the a-axis.

**Table 13.** Equation of state parameter summary for monoclinic phases of the studied transition metal dioxides. The ranges used for fitting is indicated by low, high and full for individual data sets and the combined sets. Linear bulk moduli are indicated by subscripts of the respective axis.

	MoO <sub>2</sub>	ReO <sub>2</sub>	TcO <sub>2</sub>
B <sub>low</sub>	205(8)	196(3)	-
B <sub>high</sub>	180(14)	220(20)	-
B <sub>full</sub>	189(3)	193(5)	172(9)
B'	4	4.4(3)	4
B <sub>a</sub>	650	900	490
B <sub>b</sub>	3590	400	230
B <sub>c</sub>	310	1450	1100

It is reasonable to expect that the direction comprised of metal-metal bonds would be the most incompressible. The chain is paired with a short and long metal-metal distance is a series of distorted octahedral that when the longer distance compresses at a faster rate than the metal-metal bonded pair result in a lowering of the distortion present. It is along this axis that the largest degree of distortion is present in the octahedra, so it makes sense that that it is relatively compressible compared to the other directions. The *b*-axis, the most compressible axis in ReO<sub>2</sub> and TcO<sub>2</sub>, is the axis that is orthogonal to the edge sharing chains. While compression in this direction can result in a smaller unit cell volume, there is the available space for rotation of the octahedra whereas the *c*-axis is not aligned with the chains and therefore the most difficult to compress.

The transition metal dioxides observed in this study revealed that there are additional high-pressure phases within reach using diamond anvil cells. It would be greatly beneficial to attempt to recover these high-pressure phases for additional characterization at ambient conditions to determine their potential for technological applications.



# An Atomistic Understanding of the Unexpectedly Low Volatility of the Molecular Oxide $\text{Tc}_2\text{O}_7$

In this chapter the thermal expansion properties of  $\text{Tc}_2\text{O}_7$  in the solid-state are investigated by single crystal X-ray diffraction over a range of 80 – 280 K and by *ab initio* molecular dynamics (MD) from 50 – 600 K. The thermal expansion coefficient was experimentally determined to be  $248 \times 10^{-6} \text{ K}^{-1}$  at 280 K. The calculations accurately reproduce the experimental crystal structure and thermal expansion.  $\text{Tc}_2\text{O}_7$ 's high melting point and low vapor pressure appear as outliers when compared to related molecular solids. By understanding the structure and the motion of the molecules in the solid state as the temperature rises and approaches the melt, we explain these interesting properties of solid  $\text{Tc}_2\text{O}_7$ . The mechanism of melting is discussed in the context of the transverse libration motion of the bridging oxygen.

## ■ Introduction

The current long-term storage solution for recovered technetium is vitrification of  $\text{NaTcO}_4$  into borosilicate glass where the technetium is encapsulated as  $\text{TcO}_3(\text{OH})(\text{H}_2\text{O})_2$ .<sup>134</sup> One of the main challenges to safe and efficient vitrification processes is the volatility of several technetium species under typical vitrification conditions ( $>1000$  °C).<sup>135</sup> For instance,  $\text{TcO}_2$  begins to sublime at 900 °C and decomposes into solid Tc metal and gaseous  $\text{Tc}_2\text{O}_7$  above 1100 °C.<sup>54</sup>  $\text{Tc}_2\text{O}_7$  is not the sole volatile species; a red phase, for which we have recently proposed the identity of  $\text{Tc}_2\text{O}_5$ , also is known to evaporate.<sup>136,137</sup> The unwanted formation of these volatile species results in only 30-70% of the  $^{99}\text{Tc}$  being encapsulated during the glass melting process.<sup>54,135</sup> Improved approaches to technetium immobilization will require a deeper understanding of the structure and properties of all important oxide phases.

It was first noted in 1953 that, while  $\text{Tc}_2\text{O}_7$  is volatile at ambient conditions, the solid has an unexpectedly low vapor pressure for a purely molecular solid.<sup>71</sup> It was also observed that the liquid stability range of  $\text{Re}_2\text{O}_7$  spans only a 60 K range while  $\text{Tc}_2\text{O}_7$  spans a 190 K range. Thus, although rhenium chemistry is often sufficiently close to technetium chemistry in that it can be used as a non-radioactive surrogate,  $\text{Re}_2\text{O}_7$  is a poor analogue to  $\text{Tc}_2\text{O}_7$  in this context. The lack of correspondence here presents challenges for experimentally validating industrial processes where the preferable course of action is working with non-radioactive homologues and assuming analogous behavior by corresponding states.

A solid with a molecular or cluster structure can be distinguished from an extended structure by the presence of well-separated molecular units. In some instances, substances do not fit neatly into

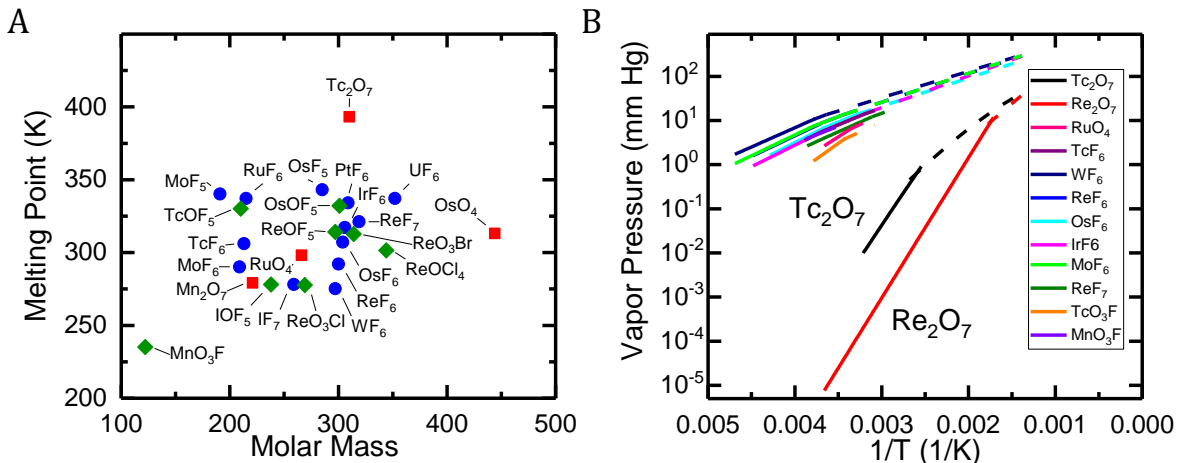
the categories of “extended” or molecular. For example, when distinctly molecular units are recognizable, close intermolecular contacts may also exist between these units where the separation is longer than a typical covalent bond, but appreciably shorter than a van der Waals contact. Here, we will define a solid as molecular when the nearest possible interaction distance between molecules is at least 40% greater than the average bond lengths found within the defined molecular species. Multiple structural determinations by X-ray diffraction unambiguously establish that  $\text{Tc}_2\text{O}_7$  is a molecular solid by this definition. Simple inspection of the crystal structure reveals a herringbone type packing of molecules with  $D_{3d}$  symmetry (linear Tc-O<sub>Bri</sub>-Tc axis) that stabilizes the linear geometry without any strong intermolecular interactions (no pseudo-extended structures/clusters/bonding).<sup>72,138</sup> Raman spectroscopy shows that the same molecular structure found in the solid persists into the liquid and gas phases, although the molecular symmetry drops to  $C_{2v}$ . Binary transition metal oxides that exist in a solid molecular structure at ambient conditions are rare and include  $\text{Mn}_2\text{O}_7$ ,<sup>139</sup>  $\text{Tc}_2\text{O}_7$ ,<sup>72</sup>  $\text{RuO}_4$ ,<sup>140</sup> and  $\text{OsO}_4$ .<sup>141</sup> The ability to study the behavior of these particular oxides is limited due to the toxicity of  $\text{OsO}_4$  and  $\text{RuO}_4$ , the explosive nature of  $\text{Mn}_2\text{O}_7$ , and radioactive nature technetium. A number of transition metal fluorides and oxyhalides of group 6, 7, 8 and 9 exist as molecular solids. The molecular structures of those species predominately have just a single metal atom in the molecule, although some form cluster structures with 2 - 4 metal atoms.

In order to relate the volatility of  $\text{Tc}_2\text{O}_7$  to that of other molecular solids, we need to select a group containing comparable types of interactions. While dispersion interactions are present in all molecular solids, stronger intermolecular interaction may also exist. In the molecular solid  $\text{ReOF}_4$ , for example, each square pyramidal molecule is aligned such that the fluorine atoms at the top of one square pyramid associate with the metal atom in an adjacent molecule through the base of the

pyramid. Such an interaction constitutes at least a significant dipole-dipole interaction, but may contain some bonding character as the intermolecular metal-fluorine distance is only ~20% longer than the average metal-fluorine distance. For systems like  $\text{ReOF}_4$ , with appreciable interactions beyond those observed in  $\text{Tc}_2\text{O}_7$ , we anticipate higher melting points and lower vapor pressures. For the molecular transition metal compounds with unambiguously molecular character and only comparable dispersive interactions, the melting point for  $\text{Tc}_2\text{O}_7$  stands out as exceptional **Figure 28a**.

While vapor pressure data is not as readily available as melting point data in the academic literature, it has been reported that  $\text{Tc}_2\text{O}_7$  has considerably lower pressure (0.37 mmHg at 100 °C)<sup>71</sup> than the other similar compounds, as seen in **Figure 28b**. Rhenium heptoxide is the sole identified compound with a lower vapor pressure than  $\text{Tc}_2\text{O}_7$ . Examination of the  $\text{Re}_2\text{O}_7$  extended structure demonstrates that there are two Re-O bonds in the rhenium octahedral which are longer than the others. These covalent interactions are all that separate  $\text{Re}_2\text{O}_7$  from being molecular and can readily be visualized as if molecular by ignoring these bonds. As a result of these stronger intermolecular interactions in  $\text{Re}_2\text{O}_7$ , the cohesive energy of the solids is twice that of  $\text{Tc}_2\text{O}_7$  based on high level calculations.<sup>142</sup>





We recently re-determined the crystal structure of  $\text{Tc}_2\text{O}_7$  at 100 K. When compared to the original room-temperature structure determination from 1969, we noted that the bond lengths reported at room temperature were shorter than those we had measured at cryogenic temperatures.<sup>10,72</sup> A quantitative understanding of the identity and behavior of the volatile technetium species is required for designing safe contamination controls and improving the retention of technetium in the glass during vitrification. Additionally, molecular metal oxides are quite uncommon and remain poorly characterized. Consequently, we have examined the behavior of a  $\text{Tc}_2\text{O}_7$  crystal as a function of temperature with a combined approach of single crystal X-ray diffraction (SC-XRD)

and *ab initio* molecular dynamics (MD) simulations. Our investigation provides a detailed atomistic picture of the structure as a function of temperature. From that atomistic picture, we propose a mechanism for melting that accounts for the observed low vapor pressure and high melting point of  $\text{Tc}_2\text{O}_7$ .

## ■ Methods

The sample for single crystal X-ray diffraction (SC-XRD) was prepared in a sealed tube by the oxidation of  $\text{TcO}_2$  with  $\text{O}_2$  at 450 °C as previously reported.<sup>138</sup> SC-XRD data were collected on a Bruker Apex II system equipped with an Oxford nitrogen cryostream. Diffraction data were collected from 80 K through 280 K at 20 K intervals. In order to minimize error, all datasets were collected on the same crystal which was initially cooled to 80K and gradually warmed as data were taken. In the APEX II suite,<sup>84</sup> data reduction was performed using SAINT, the structure was solved with SHELXT,<sup>85</sup> and an absorption correction was performed with SADABS.<sup>86</sup> Structure solutions were conducted independently at each temperature. Structure refinements against  $F^2$  were carried out using the SHELXL refinement package in OLEX2-1.2.<sup>87</sup>

Plane-wave density functional theory (PW-DFT)<sup>143,144</sup> Langevin MD<sup>145–147</sup> simulations were performed with the Vienna *ab initio* simulation package (VASP) version 5.4.1 using the generalized gradient approximation (GGA) functional of Perdew, Burke, and Ernzerhof (PBE)<sup>148</sup> with Grimme's -D3<sup>149</sup> semi-empirical dispersion correction. The projector augmented wave (PAW)<sup>111</sup> pseudo-potentials formulated for PBE GW calculations were used to represent the ionic cores with valence configurations  $4s^24p^65s^24d^5$  for Tc and  $2s^22p^4$  for O.<sup>150</sup> The  $\Gamma$ -point alone was used to represent the first Brillouin zone. The plane waves were cut off at 600 eV. The energy

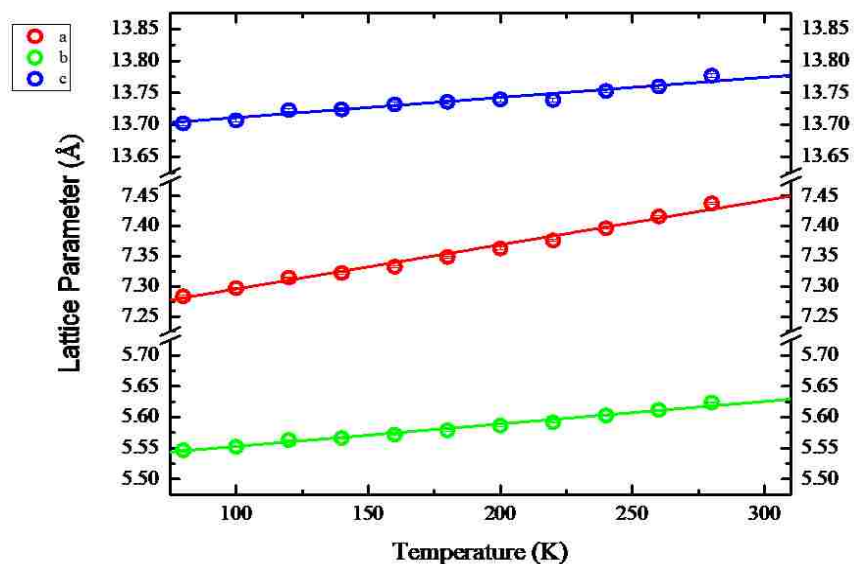
convergence criterion for an SCF cycle was set to  $10^{-5}$  eV. All lattice and atomic degrees of freedom were allowed to fluctuate in each simulation with no regard for electronic or molecular symmetry. Vibrational analysis of a single molecule of  $\text{Tc}_2\text{O}_7$  indicated that the period of the fastest mode (a  $-\text{TcO}_3$  breathing mode) is  $\sim 35$  fs,<sup>142</sup> so a time step of 2 fs was used to adequately sample all the motions of the molecules. For each temperature, the structures were thermally equilibrated with a 10 ps simulation in the isothermal-isobaric (NpT) ensemble. Using the thermally equilibrated structures and velocities, the trajectories were propagated for another 10 ps in the isoenthalpic-isobaric (NpH) ensemble. The NpH ensemble was chosen because it does not require a thermostat and thus better represents elastic momentum transfer which is important for describing the collective motions of a thermally excited molecular solid. The Langevin damping parameters were selected following literature guidelines for classical simulations:  $1 \leq \gamma \leq 10$  refined to one significant figure with several short time test trajectories.<sup>145</sup> The atoms had a friction coefficient of  $3 \text{ ps}^{-1}$  in the NpT ensemble, and by definition  $0 \text{ ps}^{-1}$  in the NpH ensemble. The lattice degrees of freedom had a friction coefficient of  $1 \text{ ps}^{-1}$  and a fictitious mass of 100 amu in every simulation. The initial structure for each trajectory was a  $2 \times 2 \times 1$  super cell (144 atoms) of the previously optimized crystal structure,<sup>142</sup> which was chosen as it was the smallest cell where thermal fluctuations were  $\leq 10\%$  of the target temperature in the short-time test calculations of the damping parameters. The initial velocities came from a randomly generated Maxwell-Boltzmann distribution around the input temperature.

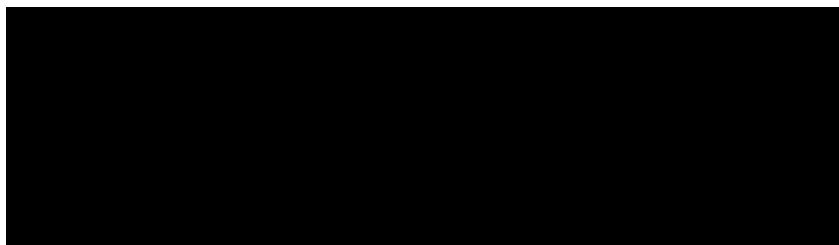
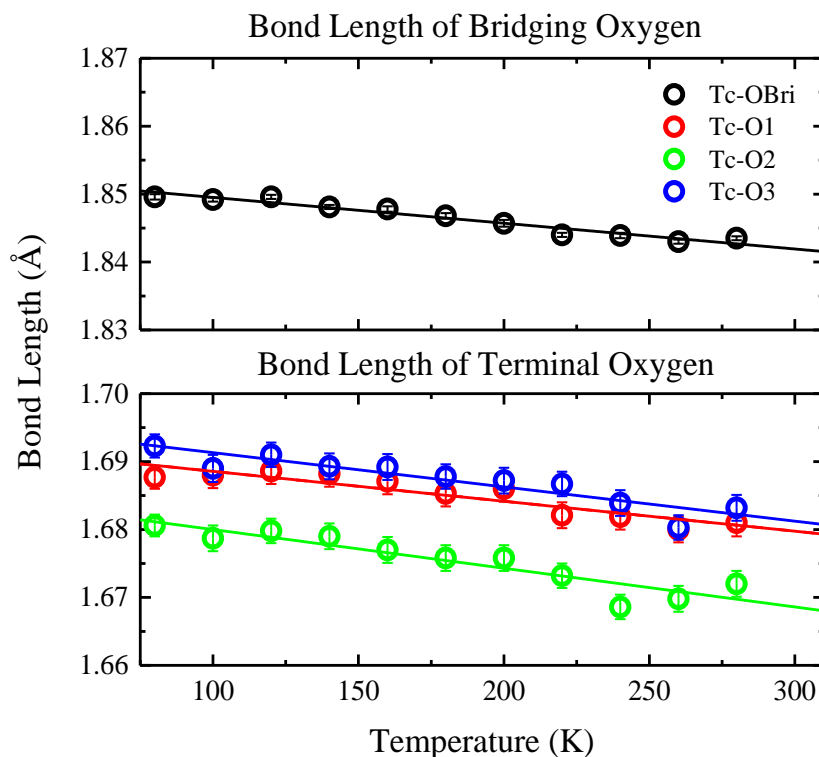
## ■ Results and Discussion

The thermal behavior of crystalline  $\text{Tc}_2\text{O}_7$  presents several characteristics warranting further investigation. As shown in the introduction, the melting point is anomalously high for a molecular solid bound only by van der Waals interactions as compared with other solids with similar molecular mass. Correspondingly, the vapor pressure is unusually low for the molecular mass. Secondly, the intramolecular bond distances appear to shorten with increasing temperature as measured by SC-XRD. The temperature-dependent properties were examined by measuring SC-XRD data over a range of steadily increasing temperatures from liquid nitrogen (80 K) to near ambient (280 K). The previously reported *Pbca* structure consistently provided the best structural model over the entire temperature range.<sup>72,138</sup> The quality of data and structure refinement did not degrade markedly as shown by the R-values which ranged from 1.74% to 2.37% with no systematic trend corresponding to the increasing temperature.

The unit cell edge lengths and volume, **Figure 29** all exhibited positive thermal expansion throughout the temperature range studied. The smooth thermal expansion observed over the entire temperature range coupled with very similar structure refinements, is consistent with the absence of any phase transitions over this temperature range. The coefficients of volumetric thermal expansion and linear thermal expansion for each cell edge length was fit with  $R^2$  – values exceeding 0.95 for all fits. The coefficients of thermal expansion are  $\alpha_v = 18.9 \times 10^{-5} \text{ K}^{-1}$ ,  $\alpha_a = 10.3 \times 10^{-5} \text{ K}^{-1}$ ,  $\alpha_b = 6.7 \times 10^{-5} \text{ K}^{-1}$ , and  $\alpha_c = 2.3 \times 10^{-5} \text{ K}^{-1}$ .

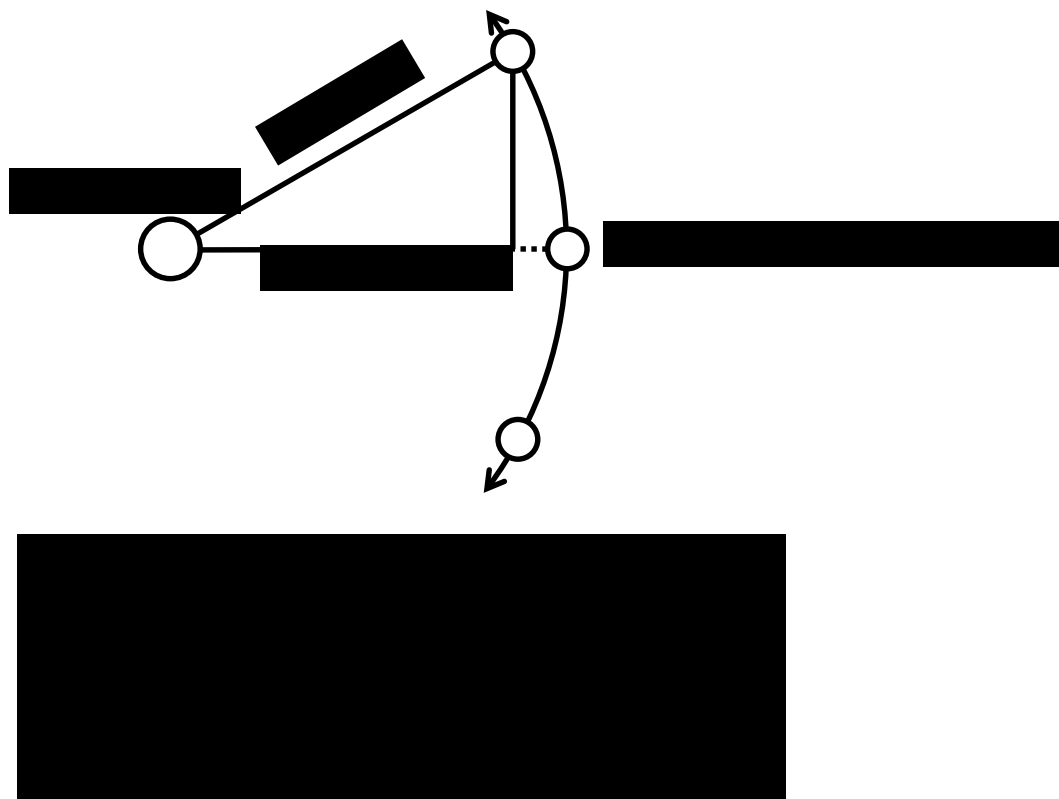
The thermal expansion of solid-state *Pbca*  $\text{Tc}_2\text{O}_7$  is significantly anisotropic with the *c* and *a* crystallographic axis expansion lower by factors of 2.9 and 4.5 respectively, compared with the *b*-crystallographic axis. This may be rationalized by considering that the linear  $\text{Tc-O}_{\text{Bri}}\text{-Tc}$  axes of the molecules lies in the 010 plane. The effect of thermal expansion along the *a*-crystallographic axis is largely increasing the empty space between the packed molecules, whereas expansion along the *b*- and *c*-crystallographic axes requires disrupting the herringbone packing configuration that restricts rotation of the tetrahedra. The central linear axis of the molecules has a greater projection onto the *c*-crystallographic axis, explaining why it is the direction most resistant to expansion. While a volumetric thermal expansion coefficient of  $189 \times 10^{-6} \text{ K}^{-1}$  is larger than typical across all solids, it is consistent with other molecular solids held together through weak van der Waals interactions. For example, the volumetric thermal expansion coefficients at 20 °C for ice, Aspirin, and Naphthalene (35 °C) are 151, 92.6, and  $422 \times 10^{-6} \text{ K}^{-1}$ , respectively.<sup>151–153</sup>





The Tc – O bond distances experimentally measured by SC–XRD are plotted in **Figure 30**. The Tc – O bond lengths clearly contract across the temperature range of the measurements. In the *Pbca* space group, the individual molecules are exactly linear and are arranged as  $(\text{O}_{\text{Ter}})_3\text{-Tc-O}_{\text{Bri}}\text{-Tc-(O}_{\text{Ter}})_3$ , with the central bridging oxygen sitting on an inversion center. The *Pbca* asymmetric cell consists of 1 Tc atom and 4 unique oxygen atoms, resulting in four unique Tc – O bonds all exhibiting slightly different bond lengths contracting at roughly consistent rates:  $-3.8$  to  $-5.7 \times 10^{-5} \text{ K}^{-1}$ . As the potential energy curves, which describe bonding are intrinsically anharmonic such that increased vibration *always* leads to longer average bond lengths, the observation of contracting Tc – O bonds appears counterintuitive.

The apparent shortening of Tc – O bonds can be accounted for by initially recalling that diffraction techniques measure average electron density distributions for crystalline solids. In this discussion, we will refer to the average position of atoms inferred by locating the maximum of the electronic density as the “apparent” positions and bond lengths. We will refer to the actual internuclear separation as the “real” or “instantaneous” bond length. Next, we must consider how increasing vibrations from higher temperatures affects the average electron density and thus the apparent bond length. Vibrations in the direction of the metal – oxygen bond will increase the real bond length as well as the apparent bond length. However, vibrations transverse to the metal – oxygen bond



vector will result in the lighter oxygen atom following an arc around the metal atom. This type of vibrational motion which is referred to as a libration, (see **Figure 31**<sup>154</sup>). The magnitude of librations increase as the temperature rises. When the electron density of the atom oscillating on

an arced path is modeled with an ellipsoid, the center of the ellipsoid (ie. the atom position) is determined to be closer than its true position. The magnitude of this phenomena is amplified at elevated temperatures when the motion is larger. It should be recalled that this shortening is in the apparent bond length;<sup>155</sup> the real (instantaneous) bond distance does not decrease at any time.

The effect of librations has been described previously for diffraction experiments<sup>154</sup> and it can be corrected for in the software package Platon using Schomaker and Trueblood's Rigid Body Motion analysis, the TLS-model.<sup>156,157</sup> When the TLS model is applied at each temperature, it significantly reduces the apparent rate of contraction, but does not yield a positive thermal bond expansion for any of the Tc-O bonds, as seen in **Figure 32**. To further test if the negative thermal bond expansion in Tc<sub>2</sub>O<sub>7</sub> is due to symmetry constraints of the space group, the TLS-model was applied to the structure as solved in the lower symmetry space group, *Pca2<sub>1</sub>*. Lowering the space group removes the inversion center on the bridging oxygen, which expands the asymmetric unit to include the full molecular unit. With the full molecule being described by independent atoms, unique Tc-O bond lengths are determined and the constraint that the Tc-O-Tc bridge equal 180° is eliminated. This results in asymmetric Tc-O<sub>Bri</sub> distances and shorter Tc-Tc distance in *Pca2<sub>1</sub>*. **Table 14** shows that for the two Tc-O<sub>Bri</sub> and Tc-Tc distances as well as the bond angle, there is no systematic trend with respect to temperatures, nor are the values within the standard uncertainty of the measurement. The values appear to be randomly fluctuating beyond what is accounted for by the error of the measurement. The overall quality of the refinements declines slightly when fit in the lower symmetry space group despite the increase in refinement parameters. In both cases, for the raw data and with the TLS correction, the *Pbca* structure model is a better fit.



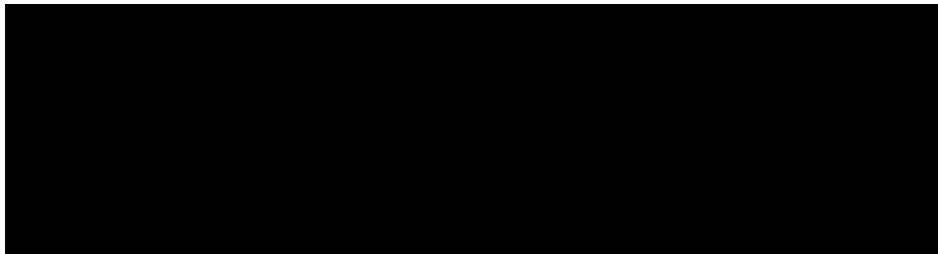
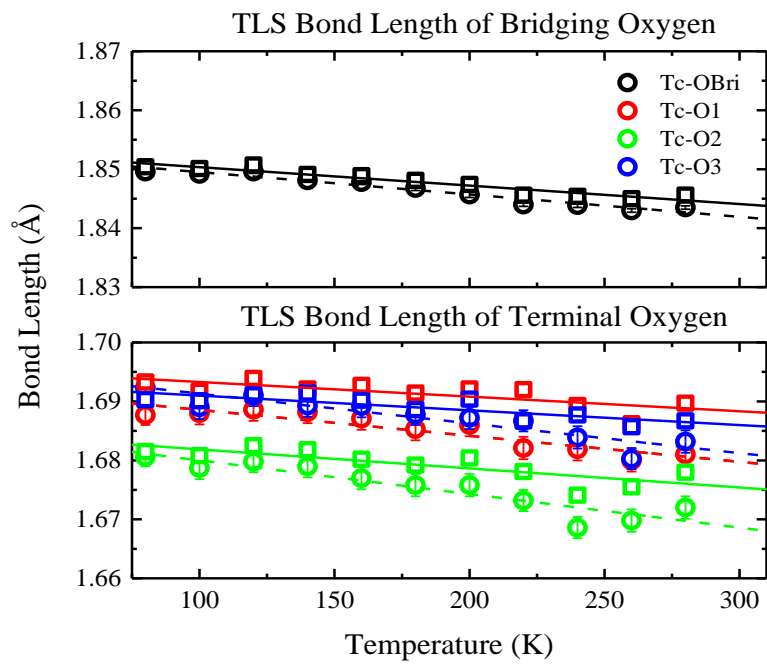


**Table 14.** Bond lengths and angles for the bridging oxygen of  $Tc_2O_7$  model in  $Pbca$  and  $Pca2_1$ . Standard uncertainties in last digit indicated by parenthesis.

Temperature (K)	<i>Pbca</i>		<i>Pca2<sub>1</sub></i>			
	Tc-O <sub>bri</sub> (Å)	Tc-Tc (Å)	Tc <sub>1</sub> -O <sub>bri</sub> (Å)	Tc <sub>2</sub> -O <sub>bri</sub> (Å)	Tc-Tc (Å)	<Tc-O-Tc (°)
80	1.8496 (4)	3.6992 (8)	1.681 (9)	1.699 (10)	3.379 (10)	177.1 (11)
100	1.8492 (3)	3.6984 (6)	1.705 (9)	1.895 (14)	3.596 (14)	174.6 (9)
120	1.8496 (3)	3.6992 (6)	1.727 (5)	1.841 (8)	3.567 (8)	177.5 (4)
140	1.8481 (3)	3.6962 (6)	1.684 (12)	1.896 (18)	3.577 (18)	175.3 (14)
160	1.8478 (4)	3.6956 (8)	1.691 (12)	1.865 (9)	3.552 (12)	174.6 (9)
180	1.8468 (4)	3.6936 (8)	1.710 (15)	1.916 (9)	3.622 (15)	174.7(10)
200	1.8457 (5)	3.6914(10)	1.651 (2)	1.860 (12)	3.508 (12)	175.3 (13)
220	1.8440 (3)	3.6880 (6)	1.639 (14)	1.814 (10)	3.450 (14)	175.4 (11)
240	1.8439 (4)	3.6878 (8)	1.685 (11)	1.713 (12)	3.394 (12)	174.6 (11)
260	1.8430 (3)	3.6860 (6)	1.692 (15)	1.900 (3)	3.592 (15)	179.0 (17)
280	1.8435 (3)	3.6870 (6)	1.674 (12)	1.817 (18)	3.488 (18)	175.0 (12)

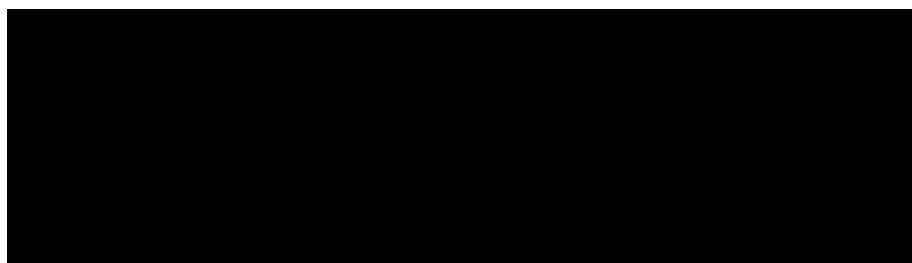
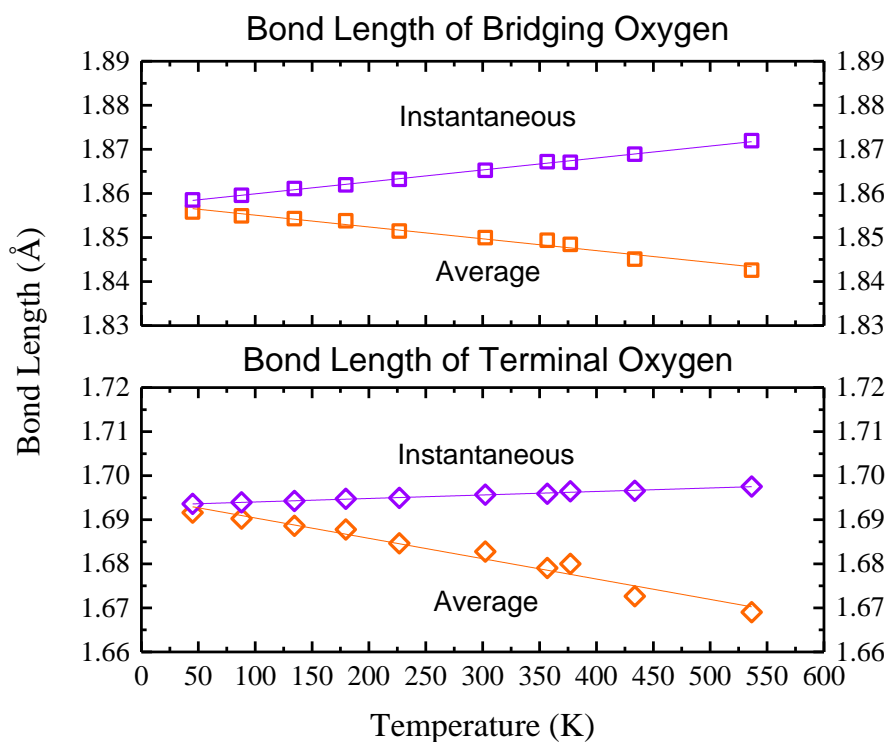
As these corrections are the current state of the art for handling rigid-body motion and librations for SC-XRD data, it must be assumed that any refinement of  $Tc_2O_7$  will exhibit negative bond thermal expansion. That being stated, there are two possibilities for the observed negative bond thermal expansion that must be considered: the negative bond thermal expansion is real, or the model (even with the corrections) is insufficient to describe the thermal behavior of solid  $Tc_2O_7$ . It would not make physical sense for the instantaneous Tc – O distances to actually contract, so we conclude that the model (even with the corrections) is insufficient, to describe the thermal behavior of solid  $Tc_2O_7$ . For the bridging oxygen, it is easy to understand why the model would be insufficient as a standard libration correction would require the oxygen to be closer to one technetium atom than the other. A more realistic description of the bridging oxygen would treat it as following a circular or elliptical path around the linear axis between the two technetium atoms. Evidence of this type of motion has been seen in extended solids and labeled as transverse librational motion.<sup>158</sup> In  $ZrW_2O_4$ , a negative thermal expansion material, it has been reported that bulk negative thermal expansion properties are linked to transverse librational motion of a 2-

coordinate oxygen atom. While both  $\text{ZrW}_2\text{O}_4$  and  $\text{Tc}_2\text{O}_7$  exhibit similar thermal motion of the bridging oxygen, the large thermal expansion between molecules in  $\text{Tc}_2\text{O}_7$  dominates the overall temperature/volume behavior.

As conventional bond distance corrections could not adequately explain the temperature dependent structures of  $\text{Tc}_2\text{O}_7$ , *ab initio* molecular dynamics (MD) simulations were employed to determine if the negative bond thermal expansion is real and to gain further insight into the thermal behavior of solid  $\text{Tc}_2\text{O}_7$ . MD trajectories with initial temperatures of 50, 100, 150, 200, 250, 300, 350, 400, 500, and 600 K and a pressure of 1 bar were run to emulate the SC-XRD experiments. The MD trajectories do confirm the measured positive volumetric thermal expansion. The optimal PW-DFT edge lengths for the *a*- and *b*-crystallographic axis is 1-2% smaller than the experimentally measured values. MD predicts a nearly identical trend for the expansion of the *a*-crystallographic axis as a function of temperature, while the *b*-crystallographic axis expands at a slightly lower rate than for the experiment. On the other hand, the optimal PW-DFT edge length for the *c*-crystallographic axis is ~1% larger than the experiment at 100 K, and MD predicts it to expand at a much lower rate than observed experimentally. We believe this is an artifact of the modest size of the simulation cell that was chosen, which will be discussed in more detail later.

Average structural information was extracted from the series of snapshots provided by the *ab initio* MD simulations using two different methods. First, the time average of each atomic position can be evaluated; distances between the average atomic positions provided from this approach provide bond lengths consistent with structural methods that provide average structures such as SC-XRD. Results from treating the MD predictions this way are plotted as an orange line labeled as “average” in **Figure 33**. These trends follow the experimental data provided by SC-XRD, as

anticipated. We note that, because rotation of the  $\text{TcO}_3$  units during an MD simulation would result in crystallographically distinct oxygen atoms switching locations. The simulation results are presented where  $\text{Tc}_2\text{O}_7$  molecules are treated as having only two chemically unique oxygen atoms; the terminal and bridging atoms, during the simulation all atoms were independent and unique. The result is that we only provide a single length calculated for the terminal oxygen atoms as opposed to the three unique oxygen bond lengths in the asymmetric  $Pbca$  cell used in the analysis of the SC-XRD data.

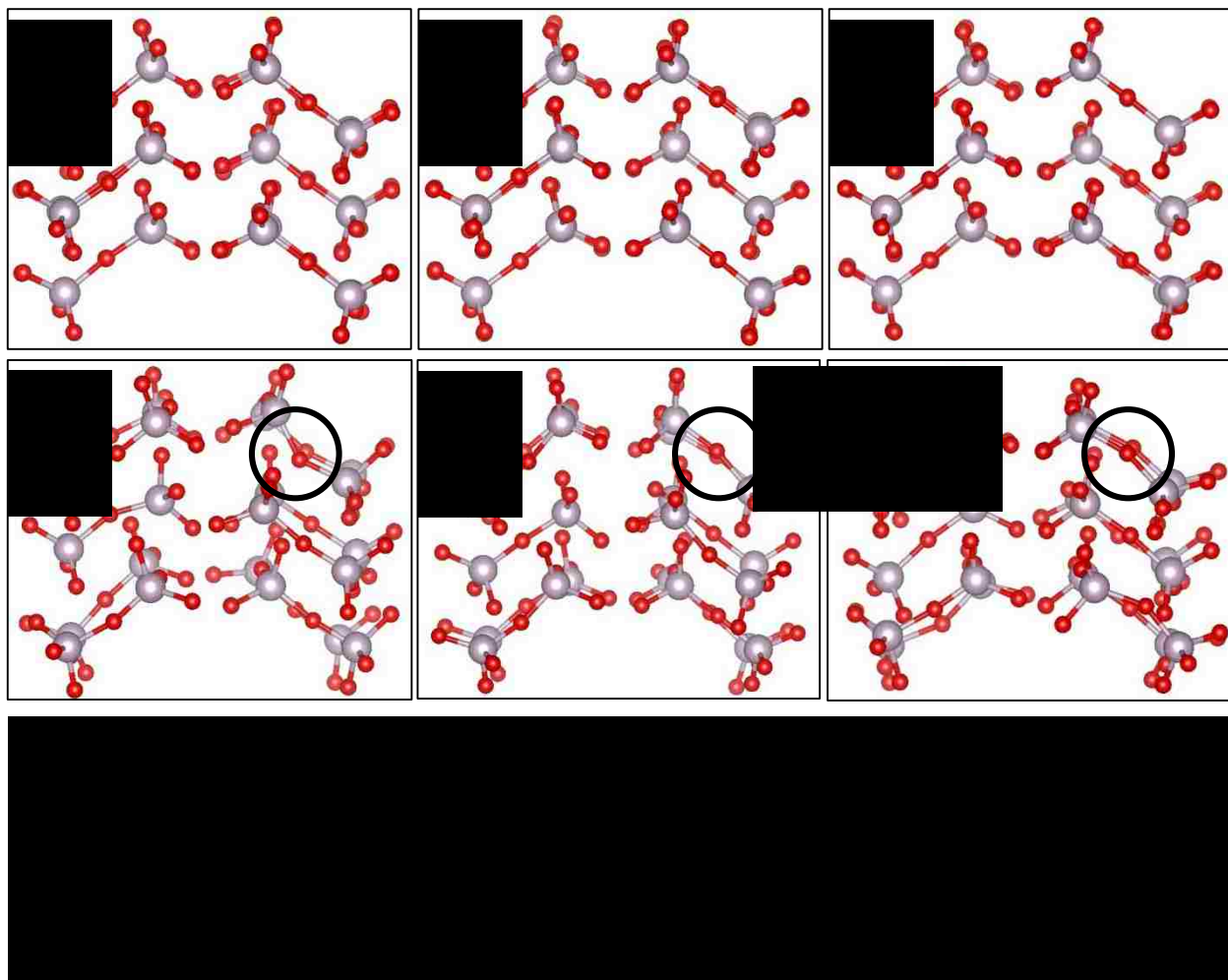


A different way to extract average bond distances from the MD simulations is to calculate the “instantaneous” atom-atom separation in each snapshot and to average those values. For a completely static structure, this is equivalent to the first method. Extraction of bond distances with this approach yields the purple curve labeled “instantaneous” in **Figure 33**. At the lowest temperature simulated (50K), overall motion is low and the “instantaneous” vs. “average” approaches provide nearly identical bond distances as expected when approaching the limit of a static structure with no thermal motion. The simulations show the “instantaneous” distances increase with increasing temperature, while the “average” bond distance decrease appreciably. The most significant difference is that purely transverse motions, which we interpret are responsible for the apparent negative thermal bond contraction present in the SC–XRD data, are no longer present, causing only positive bond length thermal expansion to be observed. The terminal oxygen atoms are undergoing the anticipated librational motion, which makes it surprising that the crystallographic libration correction was unable to capture the effect. This could be a combination of robust thermal motion and a tight electron density around the doubly bound terminal oxygen atoms causing the thermal ellipsoids in the model to be too small.

Snapshots of MD trajectories at 50 K and 600 K at 150 fs intervals are compared in **Figure 34**. By tracing the trajectory of a bridging oxygen atom at 600K it is confirmed that the bridging oxygen does exhibit a transverse librational motion in a circular path about the line of centers between the Tc atoms, which is causes its SC–XRD determined bond length to appear to shrink with temperature. The complexities of the electron density of the bridging oxygen are beyond what can accurately be described without high resolution charge density studies.<sup>159</sup> The speed of the bending vibrations coupled with a lack of directional dependence are what causes the electron density to be fit by a model with a linear Tc-O-Tc. The lack of directional dependence is reinforced by the

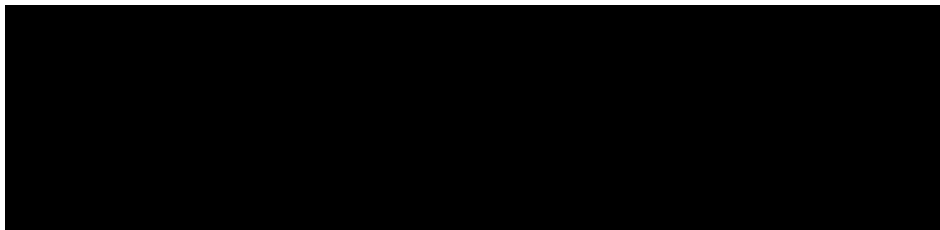
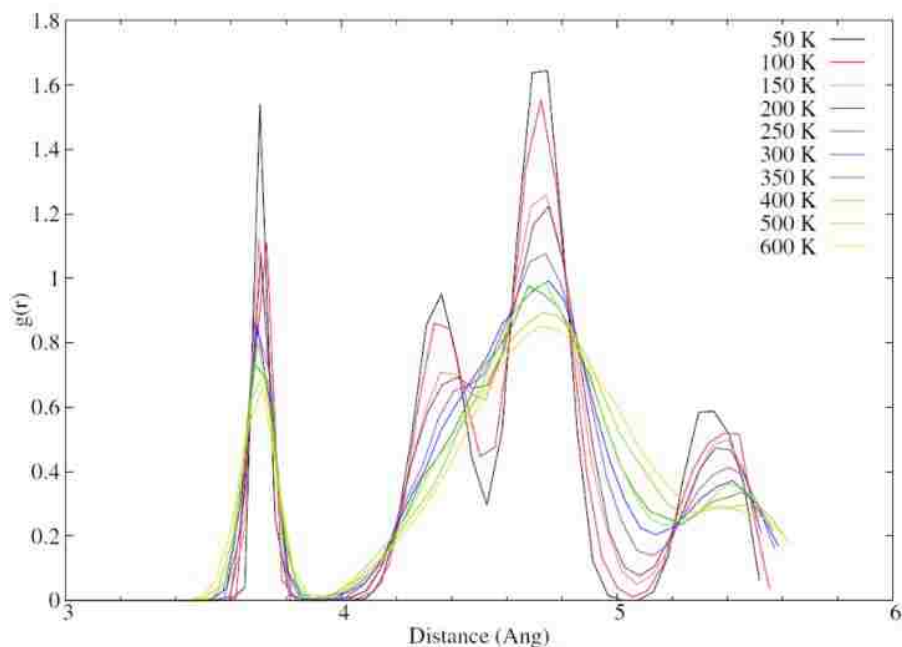
SC-XRD refinements in the alternate  $Pca2_1$  setting for solid  $Tc_2O_7$ . The  $Pca2_1$  model implies a direction preference for the oxygen atom position, and the directional independence of the thermal motion causes the  $Pca2_1$  refined structures to have even smaller deviations from linear Tc-O-Tc than the simulations.

Close inspection of the MD snapshots shows that, while the vibrational motions are becoming more pronounced with temperature, the  $-O-TcO_3$  tetrahedra exhibit virtually no rotation, and the only motions in the  $-TcO_3$  units are the vibrations/librations of the terminal oxygen. From the perspective of our previous molecular calculations, this result is not immediately intuitive as the potential energy surface for rotation of  $-TcO_3$  units in a single molecule of  $Tc_2O_7$  is essentially flat.<sup>142</sup> While an isolated molecule is expected to have nearly free rotation of  $-TcO_3$  groups, the



absence of this in the solid state must be due to steric effects from adjacent molecules. On examination of the structure, we find that the terminal oxygen atoms interlock like the teeth of the intermeshed gears along the  $a$ -crystallographic axis. This arrangement is present at all temperatures examined and there is no evidence of rigid rotor like free rotation. Correlated rotations of these groups is hindered by the herringbone packing of the molecules. The gear-like packing is not just between molecules along the same  $ab$ -planes, but also between the different layers such that correlated rotations are also limited. The terminal oxygen atoms from the molecules centered in one plane point into the centroid of the tetrahedra in the next plane over. The result is a high degree of interlocking of the molecules, higher steric energy, and the lack of rotational motion observed with MD. The tightness of this packing is evident by analyzing the Tc-Tc pair distribution function **Figure 35**. The intramolecular distance remains very sharp at all temperatures; it is not until 300 K that the first intermolecular distances begin to broaden and lose their sharp crystallinity. Even at 600 K the nearest neighbour features exhibit distinct ordering and regions of near zero atomic density before and after the first nearest neighbor peaks.

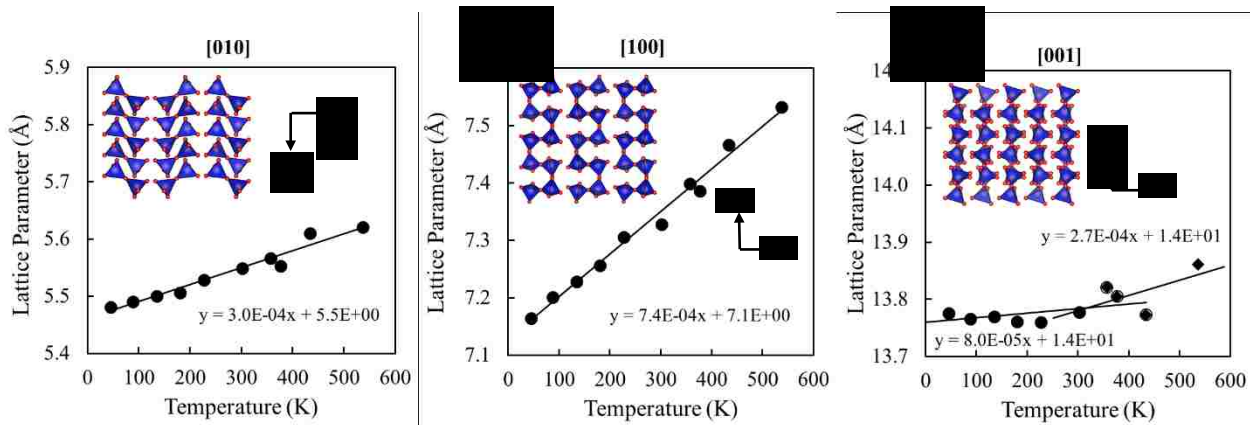
Experimentally, the linear thermal expansion in the direction of the  $c$ -axis was found to be at least a factor of two smaller than for the other crystallographic axes, which we previously attributed to the alignment of the  $\text{Tc}_2\text{O}_7$  molecules along the  $c$ -axis which contributes to this stiffness. The motion of the  $-\text{TcO}_3$  groups is restricted by steric effects of neighboring molecules. The simulated thermal expansion is smooth over the sampled temperature range along the  $a$ - and  $b$ - axis, with a linear response modeled with  $R^2$ -values greater than 0.95, as seen in **Figure 36**. In the direction of the  $c$ - axis, the lattice parameters do not change linearly over the entire range but instead can be described roughly as two linear regions meeting at 320 K, a temperature which correlates with the broadening of nearest neighbor distances in the Tc-Tc RDF. A discontinuity in the equation-of-



state function indicates a phase transition, which we presume to be either the onset of melting or an order/disorder transition with regards to the tight herringbone packing. At the transition point in the thermal expansion curve, the system has enough thermal energy to overcome the energetic barrier of the tight packing along the  $c$ - axis and begins expanding along the  $c$ - axis at a comparable rate to the other axes.

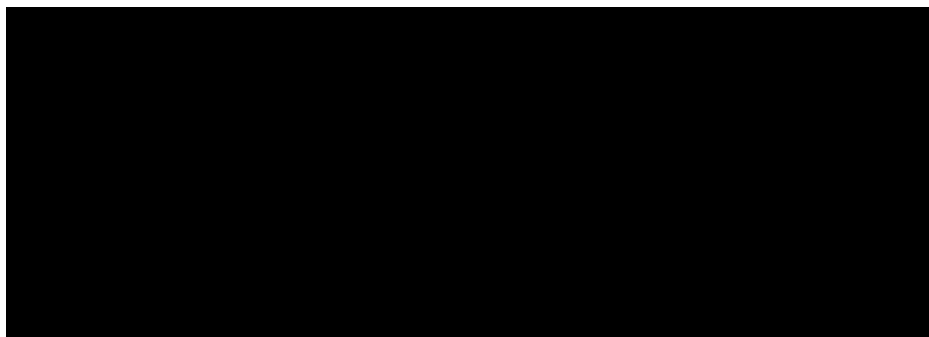
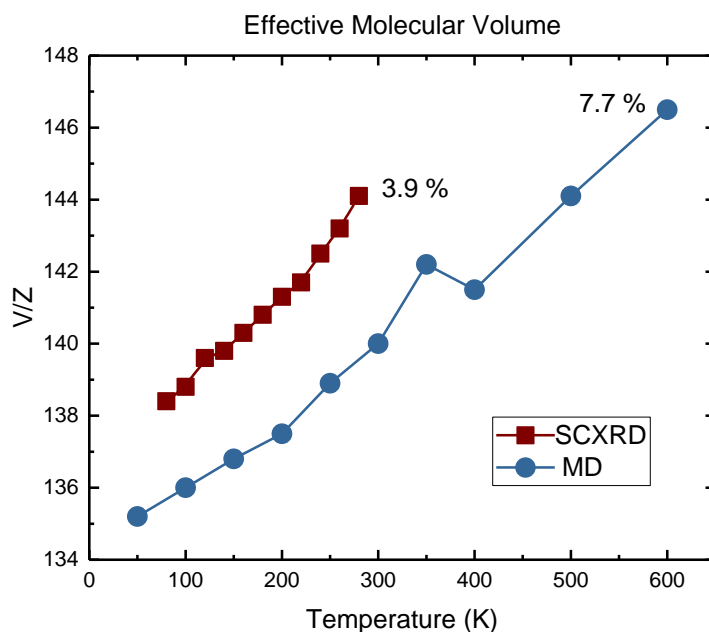
One thing to note is that the simulation cell, while large enough for *ab initio* equilibration simulations, it is much too small to observe the nucleation process of melting.<sup>160</sup> In addition, periodic boundary conditions, while necessary to simulate periodic solids, hamper nucleation events. The result is that, in the simulations, the system remains crystalline up to 600 K, although





the solid is known experimentally to boil well below that temperature. Raising the temperature to 1000 K does cause the simulation cell to exhibit a large expansion. This indicates a order-disorder transition with large hysteresis to be expected using a 1-phase approach with a small simulation volume to approximate melting.<sup>161</sup> Unfortunately, the 10 ps simulation time was insufficient to equilibrate the simulation volume. On a technical note, it should be pointed out that the NpH simulations showed a slight downward trend of the free energy vs. time plots, showing some over-damping of the lattice degrees of freedom. Additionally, the production runs typically started at a temperature below the initial target temperature indicating that there may also have been some over-damping of the atomic degrees of freedom. Each of these technical limitations prevent quantitative agreement between simulation and experiment; however, the simulations are of sufficient quality to provide qualitative agreement with experiment and an explanation for the phenomena observed.

Our investigation into the thermal behavior of  $Tc_2O_7$  shows that there is increasing molecular movement with temperature that may be rationalized to provide insight regarding what occurs in the solid as melting is approached. As molecular thermal motion (COM translation, central axis rotation, vibrations) increases, the effective volume of each molecule increases as well as the total volume of the unit cell. **Figure 37** shows the effective molecular volume increasing with rising temperature. As the molecular volume increases, the molecules are less-tightly fit into the herringbone-style packing which is less efficient at constraining rotation of the  $-TcO_3$  group. From



the simulated thermal expansion in the direction of the  $c$ - axis, some energetic barrier is overcome regarding to the packing at 320 K such that the rate of thermal expansion increases. The rate of

thermal expansion in the direction of the  $c$ - axis after this transition point is comparable to the direction of the  $b$ - axis, where steric hindrances restrict motion. For melting to occur, it is expected that there will be free rotation of the  $-\text{TcO}_3$  group observed above the melting temperature. Since the best indication of the observation in the simulation of melting is seen by the discontinuity along the direction of the  $c$ - axis, it is reasonable to conclude that increasing temperature up to the melting point will increase the distance between molecules in the  $a$ - and  $b$ - directions with less change in the  $c$ - direction due to steric effects of the favorably packed terminal oxygens. As the temperature of the crystal increases the transverse librational motion of the bridging oxygen continues to increase, and the rigid-body motion of the corner sharing tetrahedra is dominated by this libration. The extent of the libration of the bridging oxygen may also be observed by comparing the time averaged single structure's average Tc-O-Tc bond angle with time averaged instantaneous values for that angle. The single structure average Tc-O-Tc angle remains  $\sim 180^\circ$  for all the temperatures measured; however, the average of the instantaneous values drops to  $164^\circ$  at the highest simulation temperature. This is striking because in our previous study,<sup>142</sup> the minimum energy structure for a single molecule of  $\text{Tc}_2\text{O}_7$  with a  $156^\circ$  Tc-O-Tc angle was found.<sup>142</sup> Presumably once the effective molecular volume is large enough for the molecules to adopt the optimal bond angle for a single molecule, the particles will be able to freely bend and rotate and  $\text{Tc}_2\text{O}_7$  will melt.

## ■ Conclusions

In conclusion,  $\text{Tc}_2\text{O}_7$  is a molecular oxide with an unusually low vapor pressure and high melting point. Its molecular nature is corroborated with a crystallographically determined volumetric

thermal expansion coefficient that is far greater than metallic or extended inorganic solids, and is more in line with dispersion-bound organic molecular solids. The thermal expansion is anisotropic, with the relative stiffness of the axes corresponding to the degree of alignment of the central bonding and compression axis. Initial measurements indicated negative thermal bond expansion for all Tc-O bonds in the molecules. Simulations show the bonds do exhibit normal positive thermal expansion, and the apparent negative thermal expansion is due to librational motion that was not well corrected for using standard TLS-model. Development of strategies to lower the volatility of technetium oxide species require a detailed understanding of these species and their thermal behaviour. Appreciation of the structural effects that librations produce in this system aid in interpreting the temperature dependent behaviour of this solid in a quantitative manner. In  $\text{Tc}_2\text{O}_7$ , the librations not only explain the bond thermal expansion, they also can be used to explain the mechanism of melting. The low volatility results from molecules packing with a herringbone-like motif where favorable packing results in stronger van der Waals interactions than might otherwise be anticipated. Thermal expansion and increasing libration of the bridging oxygen reduces the favorability of this packing arrangement, leading to melting and volatility. While the complementary techniques of SCXRD and DFT-MD have provided valuable insight into the molecular motion of technetium heptoxide it may be of additional worth to explore the complexities of the three-centered covalent bond on the bridging oxygen atom using an experimental technique like high resolution charge density studies.

# Conclusion

To better understand the nature of technetium metal and technetium oxides, the structure response of materials to high pressure and variable temperature was explored to determine equations and state and phase diagrams.

In the first portion of this work, the equation of state of technetium was determined at high pressure for the first time. Subsequent measurements extended the pressure range to 1.5 Mbar. These compression experiments were collected at room temperature using diamond anvil cells. Multiple pressure transmitting media were used to measure the difference in response of the metal and the susceptibility to nonhydrostatic pressure. The first of these compressions was conducted in a mixture of MeOH-EtOH to a maximum pressure of 67 GPa. The bulk modulus in this media is  $B_o = 288$  GPa and  $B'_o = 5.9(2)$ . Using a neon medium, 152 GPa was reached in the second part. Fitting of this compression curve resulted in an equation of state of  $B_o = 266(4)$  GPa and  $B' = 5.3(1)$ . The thermal expansion of technetium metal was determined by X-ray diffraction measurements collected between 100 – 450 K to be  $\alpha_0 = 2.145(3) \times 10^{-5}$  1/K. In the same study, the ambient structure was determined using high resolution synchrotron diffraction. The lattice parameters are  $a = 2.74109(1)$  Å,  $c = 4.39898(3)$  Å and  $V = 28.6239(3)$  Å<sup>3</sup>.

In the second portion of this work, the phase diagram of three transition metal oxides was explored at high pressure. For molybdenum dioxide, this led to the discovery of a new phase in the CaCl<sub>2</sub> structure type. This phase is recoverable to ambient conditions. The equations of states were determined for the three monoclinic MoO<sub>2</sub> type phases in addition to the new CaCl<sub>2</sub> phase and the high temperature  $\alpha$ -PbO<sub>2</sub> type phase of ReO<sub>2</sub>. The compression behavior is the most similar

between the group 7 elements, technetium and rhenium. In MoO<sub>2</sub>, there is preferential compression along the *c*- and *a*- axis. The compression behavior of the group 7 metals dioxides can be explained by the alternating presence of metal-metal bonds in the chains of edge sharing octahedra where the larger separations are shortening quicker than compressing in the other directions due to the favorability of increasing order in the octahedra that arises from the increased rate of contraction for the nonbonded metal-metal distance.

In the final portion of this work, we continued the investigation into the structure of Tc<sub>2</sub>O<sub>7</sub>. After revisiting the structure of this molecular solid at low temperature, the thermal motion attracted interest due to an anomaly in the bond lengths. This behavior was probed using variable-temperature single crystal X-ray diffraction and Molecular Dynamics simulations. The behavior is identified as a unique form of a molecular libration. Standard TLS models were found to be unable to sufficiently correct for the motion present in Tc<sub>2</sub>O<sub>7</sub>. Librational motion in Tc<sub>2</sub>O<sub>7</sub> is present for each oxygen; the six terminal oxygen atoms and the bridging atom experience either a standard libration or a transverse librational motion. The coefficients of volumetric thermal expansion and linear thermal expansion for each cell edge length are  $\alpha_V = 18.9 \times 10^{-5} \text{ K}^{-1}$ ,  $\alpha_a = 10.3 \times 10^{-5} \text{ K}^{-1}$ ,  $\alpha_b = 6.7 \times 10^{-5} \text{ K}^{-1}$ , and  $\alpha_c = 2.3 \times 10^{-5} \text{ K}^{-1}$ . The combination of diffraction and MD provided a clear description of the motion within the crystal to show the degree of locking that the packing provided with the herringbone structure of staggered Tc<sub>2</sub>O<sub>7</sub> molecules.

The exploration into the structure response of technetium metal, technetium oxides and their neighbors has opened the door to further high pressure experiments on technetium containing species. One of the goals of this project was to provide information that can be used to aide in the further development, characterization and discovery of technetium compounds, particularly those

that can be used as waste forms. The structural information determined here is capable of supporting the ongoing experimental and theoretical work in this area. It is also possible, working from this platform of knowledge, to explore the larger phase space of pressure and temperature, not only for technetium metal but also for relevant compounds that could include technetium alloys, tertiary oxides, halides and binary compounds. Binary species of nitrogen, carbon, boron and sulfur have been synthesized in abundance with most transition metals. The landscape for high pressure synthesis is untouched and primed for exploration. In my opinion, the high pressure synthesis of binary technetium species will be the most profitable avenue of research that can be pursued when equipped with the knowledge generated in this work.

# Appendix A



**Table A.1** Technetium metal lattice parameter between 100 – 450 K. Uncertainty in are less than 0.00002 Å, 0.00003 Å, and 0.003 Å for each lattice paramete  $a$ ,  $c$ , and volume repectively.

Temp (K)	$a$ (Å)	$c$ (Å)	$V_{Tc}$ (Å <sup>3</sup> /atom)	Temp (K)	$a$ (Å)	$c$ (Å)	$V_{Tc}$ (Å <sup>3</sup> /atom)
102.5	2.73755	4.39333	14.257	104.6	2.73759	4.39339	14.257
106.7	2.73763	4.39346	14.258	108.8	2.73766	4.39352	14.258
110.9	2.73770	4.39358	14.259	113.0	2.73774	4.39365	14.260
115.1	2.73778	4.39371	14.260	117.2	2.73782	4.39377	14.261
118.4	2.73784	4.39381	14.261	121.4	2.73789	4.39390	14.262
123.5	2.73793	4.39396	14.263	125.7	2.73797	4.39403	14.263
127.8	2.73801	4.39409	14.264	129.9	2.73804	4.39416	14.265
132.0	2.73808	4.39422	14.265	134.1	2.73812	4.39428	14.266
136.2	2.73816	4.39435	14.266	138.3	2.73820	4.39441	14.267
140.4	2.73824	4.39447	14.268	142.5	2.73827	4.39454	14.268
144.6	2.73831	4.39460	14.269	146.7	2.73835	4.39466	14.269
148.8	2.73839	4.39473	14.270	150.9	2.73843	4.39479	14.271
153.0	2.73847	4.39486	14.271	155.1	2.73851	4.39492	14.272
157.2	2.73854	4.39498	14.272	159.3	2.73858	4.39505	14.273
161.4	2.73862	4.39511	14.274	163.5	2.73866	4.39517	14.274
165.6	2.73870	4.39524	14.275	167.7	2.73874	4.39530	14.275
169.8	2.73878	4.39536	14.276	171.9	2.73882	4.39543	14.277
174.0	2.73886	4.39549	14.277	176.1	2.73889	4.39556	14.278
178.2	2.73893	4.39562	14.279	180.3	2.73897	4.39568	14.279
182.4	2.73901	4.39575	14.280	184.5	2.73905	4.39581	14.280
186.7	2.73909	4.39588	14.281	188.8	2.73913	4.39594	14.282
190.9	2.73917	4.39600	14.282	193.0	2.73921	4.39607	14.283
195.1	2.73925	4.39613	14.284	197.2	2.73929	4.39620	14.284
199.3	2.73933	4.39626	14.285	201.4	2.73937	4.39632	14.285
203.5	2.73941	4.39639	14.286	205.6	2.73945	4.39645	14.287
207.7	2.73949	4.39652	14.287	209.8	2.73953	4.39658	14.288
211.9	2.73957	4.39664	14.289	214.0	2.73961	4.39671	14.289
216.1	2.73965	4.39677	14.290	218.2	2.73969	4.39683	14.290
220.3	2.73973	4.39690	14.291	222.4	2.73977	4.39696	14.292
224.6	2.73982	4.39703	14.292	226.7	2.73986	4.39709	14.293
228.8	2.73990	4.39716	14.294	229.8	2.73992	4.39719	14.294
233.0	2.73998	4.39729	14.295	235.1	2.74002	4.39735	14.295
237.2	2.74006	4.39741	14.296	239.3	2.74010	4.39748	14.297
241.4	2.74014	4.39754	14.297	243.5	2.74018	4.39761	14.298
245.6	2.74022	4.39767	14.299	247.7	2.74026	4.39773	14.299
249.8	2.74030	4.39780	14.300	251.9	2.74035	4.39786	14.301
254.0	2.74039	4.39793	14.301	256.1	2.74043	4.39799	14.302

258.2	2.74047	4.39806	14.302	260.3	2.74051	4.39812	14.303
262.4	2.74055	4.39818	14.304	264.5	2.74059	4.39825	14.304
266.6	2.74064	4.39831	14.305	268.7	2.74068	4.39838	14.306
270.8	2.74072	4.39844	14.306	272.9	2.74076	4.39851	14.307
275.0	2.74080	4.39857	14.308	277.1	2.74084	4.39863	14.308
279.3	2.74089	4.39870	14.309	281.4	2.74093	4.39877	14.310
283.5	2.74097	4.39883	14.310	285.6	2.74101	4.39889	14.311
287.7	2.74106	4.39896	14.312	289.8	2.74110	4.39902	14.312
291.9	2.74114	4.39909	14.313	294.0	2.74118	4.39915	14.313
296.1	2.74122	4.39922	14.314	298.2	2.74127	4.39928	14.315
300.3	2.74131	4.39935	14.315	302.4	2.74135	4.39941	14.316
304.5	2.74139	4.39947	14.317	306.6	2.74144	4.39954	14.317
308.7	2.74148	4.39960	14.318	310.8	2.74152	4.39967	14.319
312.9	2.74156	4.39973	14.319	315.0	2.74161	4.39980	14.320
317.1	2.74165	4.39986	14.321	319.2	2.74169	4.39993	14.321
321.3	2.74173	4.39999	14.322	323.4	2.74178	4.40006	14.323
325.5	2.74182	4.40012	14.323	327.6	2.74186	4.40018	14.324
329.7	2.74191	4.40025	14.325	331.8	2.74195	4.40031	14.325
333.9	2.74199	4.40038	14.326	336.0	2.74204	4.40044	14.327
338.1	2.74208	4.40051	14.327	340.3	2.74213	4.40058	14.328
342.4	2.74217	4.40064	14.329	344.5	2.74221	4.40071	14.329
346.6	2.74226	4.40077	14.330	348.7	2.74230	4.40083	14.331
350.8	2.74234	4.40090	14.331	352.9	2.74239	4.40096	14.332
355.0	2.74243	4.40103	14.333	357.1	2.74247	4.40109	14.333
359.2	2.74252	4.40116	14.334	361.3	2.74256	4.40122	14.335
363.4	2.74261	4.40129	14.335	365.5	2.74265	4.40135	14.336
366.6	2.74267	4.40139	14.336	369.7	2.74274	4.40148	14.337
370.8	2.74276	4.40152	14.338	370.9	2.74276	4.40152	14.338
376.0	2.74287	4.40168	14.339	378.1	2.74291	4.40174	14.340
380.2	2.74296	4.40181	14.341	382.3	2.74300	4.40187	14.341
384.4	2.74305	4.40194	14.342	386.5	2.74309	4.40200	14.343
388.6	2.74314	4.40207	14.343	390.7	2.74318	4.40213	14.344
392.8	2.74323	4.40220	14.345	394.9	2.74327	4.40226	14.345
397.0	2.74332	4.40233	14.346	399.1	2.74336	4.40239	14.347
401.2	2.74341	4.40246	14.347	403.4	2.74345	4.40253	14.348
405.5	2.74350	4.40259	14.349	407.6	2.74354	4.40266	14.350
409.7	2.74359	4.40272	14.350	411.8	2.74363	4.40279	14.351
413.9	2.74368	4.40285	14.352	416.0	2.74372	4.40292	14.352
418.1	2.74377	4.40298	14.353	419.2	2.74379	4.40302	14.353
422.3	2.74386	4.40311	14.354	424.4	2.74391	4.40318	14.355
426.5	2.74395	4.40324	14.356	428.6	2.74400	4.40331	14.356
430.7	2.74404	4.40337	14.357	432.8	2.74409	4.40344	14.358

434.9	2.74413	4.40350	14.359	437.0	2.74418	4.40357	14.359
439.1	2.74423	4.40364	14.360	441.2	2.74427	4.40370	14.361
443.3	2.74432	4.40377	14.361	445.4	2.74436	4.40383	14.362

---

**Table A.2** Technetium metal lattice parameters collected in MeOH-EtOH up to 67 GPa.

$P_{\text{Au}}$ (GPa)	$a$ (Å)	$c$ (Å)	$V$ (Å <sup>3</sup> /atom)	$a_{\text{Au}}$ (Å)
0.08	2.7404	4.3993	14.31	4.0779
0.32	2.7390	4.3984	14.29	4.0760
0.39	2.7388	4.3980	14.28	4.0755
0.47	2.7386	4.3979	14.28	4.0748
2.12	2.7355	4.3865	14.21	4.0620
2.44	2.7347	4.3841	14.20	4.0596
2.63	2.7343	4.3830	14.19	4.0582
2.89	2.7336	4.3813	14.18	4.0563
3.08	2.7334	4.3817	14.18	4.0548
3.26	2.7327	4.3804	14.16	4.0535
3.61	2.7316	4.3784	14.15	4.0510
3.94	2.7305	4.3782	14.13	4.0486
4.18	2.7301	4.3770	14.13	4.0470
4.9	2.7276	4.3743	14.09	4.0423
5.6	2.7259	4.3710	14.06	4.0370
5.8	2.7256	4.3694	14.06	4.0357
6.0	2.7254	4.3677	14.05	4.0344
6.2	2.7251	4.3667	14.04	4.0333
6.4	2.7247	4.3666	14.04	4.0318
7.4	2.7215	4.3628	13.99	4.0256
7.7	2.7213	4.3599	13.98	4.0232
8.0	2.7203	4.3598	13.97	4.0215
12.3	2.7078	4.3432	13.79	3.9957
13.1	2.7061	4.3398	13.76	3.9912
14.8	2.7030	4.3345	13.71	3.9823
16.5	2.6971	4.3231	13.62	3.9731
17.7	2.6962	4.3229	13.61	3.9672
22.2	2.6881	4.3095	13.48	3.9455
31.3	2.6692	4.2729	13.18	3.9070
32.7	2.6648	4.2711	13.13	3.9014
36.0	2.6574	4.2564	13.02	3.8891
40.1	2.6479	4.2435	12.88	3.8745
43.7	2.6436	4.2355	12.82	3.8624
46.0	2.6406	4.2280	12.77	3.8551
48.4	2.6346	4.2254	12.70	3.8474
51.8	2.6317	4.2120	12.63	3.8372
57.4	2.6214	4.1982	12.49	3.8210
62.0	2.6161	4.1868	12.41	3.8084
63.6	2.6138	4.1823	12.37	3.8041
67.1	2.6054	4.1775	12.28	3.7948

**Table A. 3** Technetium metal structure data from DFT.

$P_{\text{DFT}}$ (GPa)	$V_{\text{DFT}}$ ( $\text{\AA}^3/\text{atom}$ )
0.0	14.50
1.2	14.45
4.6	14.29
12.1	13.98
20.4	13.67
29.5	13.37
39.7	13.07
50.7	12.78
63.1	12.49
76.6	12.21
91.5	11.93
108.0	11.65
125.9	11.38
145.6	11.12
167.1	10.85
190.4	10.60
215.9	10.34
243.4	10.09
273.2	9.85

1

**Table A. 4** Technetium metal lattice parameters collected in a neon pressure transmitting medium at pressures up to 92 GPa.

$P_{\text{Au}}$ (GPa)	$a_{\text{Au}}$ (Å)	a (Å)	c (Å)	V (Å <sup>3</sup> /atom)	$P_{\text{Au}}$ (GPa)	$a_{\text{Au}}$ (Å)	a (Å)	c (Å)	V (Å <sup>3</sup> /atom)
0.3	4.0762	2.7409	4.3969	14.3	40.3	3.8749	2.6475	4.2364	12.86
0.5	4.0747	2.7406	4.3961	14.3	42.2	3.8685	2.6445	4.2298	12.81
1.1	4.0701	2.7386	4.3926	14.27	47.3	3.8522	2.6367	4.2149	12.69
3.7	4.0504	2.7305	4.3780	14.13	50.5	3.8422	2.6313	4.2052	12.61
5.0	4.0412	2.7263	4.3713	14.07	54.0	3.8321	2.6256	4.1958	12.52
8.4	4.0194	2.7149	4.3532	13.89	58.3	3.8198	2.6189	4.1847	12.43
13.0	3.9922	2.7066	4.3267	13.73	62.0	3.8099	2.6138	4.1734	12.35
14.0	3.9866	2.7038	4.3236	13.69	64.4	3.8036	2.6103	4.1667	12.29
16.3	3.9743	2.6981	4.3165	13.61	67.4	3.7960	2.6057	4.1590	12.23
17.8	3.9672	2.6937	4.3135	13.55	71.8	3.7851	2.5990	4.1483	12.13
18.2	3.9649	2.6923	4.3104	13.53	74.6	3.7784	2.5953	4.1407	12.08
20.2	3.9551	2.6867	4.3024	13.45	76.2	3.7748	2.5931	4.1360	12.04
22.7	3.9440	2.6807	4.2930	13.36	79.1	3.7680	2.5886	4.1308	11.99
24.6	3.9351	2.6766	4.2853	13.29	82.2	3.7611	2.5847	4.1226	11.93
26.6	3.9267	2.6720	4.2780	13.23	83.9	3.7574	2.5830	4.1183	11.9
28.8	3.9176	2.6679	4.2714	13.16	85.5	3.7540	2.5799	4.1153	11.86
31.9	3.9055	2.6625	4.2620	13.08	87.6	3.7495	2.5777	4.1094	11.82
33.2	3.9003	2.6602	4.2572	13.05	88.4	3.7477	2.5760	4.1081	11.80
35.3	3.8925	2.6564	4.2502	12.99	90.3	3.7439	2.5739	4.1026	11.77
37.8	3.8838	2.6519	4.2439	12.92	91.9	3.7407	2.5721	4.1001	11.75

2

**Table A. 5** Technetium metal lattice parameters collected in a neon pressure transmitting medium at pressures up to 153 GPa.

$P_{\text{Au}}$ (GPa)	$a_{\text{Au}}$ (Å)	$a$ (Å)	$c$ (Å)	$V$ (Å <sup>3</sup> /atom)	$P_{\text{Au}}$ (GPa)	$a_{\text{Au}}$ (Å)	$a$ (Å)	$c$ (Å)	$V$ (Å <sup>3</sup> /atom)
7.8	4.02282	2.7195	4.3553	13.95	88.4	3.74787	2.5686	4.1089	11.74
8.2	4.02015	2.7175	4.3539	13.92	92.1	3.74025	2.5639	4.1015	11.67
8.5	4.01815	2.7164	4.3519	13.9	95.8	3.73270	2.5592	4.0940	11.61
9.6	4.01201	2.7135	4.347	13.86	98.7	3.72711	2.5555	4.0883	11.56
11.5	4.00071	2.7065	4.3361	13.75	102.6	3.71966	2.5518	4.0807	11.51
15.2	3.98047	2.6991	4.3095	13.59	105.6	3.71395	2.5476	4.0749	11.45
30.8	3.90962	2.6627	4.2562	13.07	107.6	3.71029	2.5449	4.0686	11.41
31.6	3.90665	2.6584	4.258	13.03	110.9	3.70438	2.5417	4.0627	11.36
33.3	3.90002	2.6548	4.2483	12.97	114.2	3.69849	2.5378	4.0565	11.31
36.7	3.88765	2.6489	4.2365	12.87	116.9	3.69391	2.535	4.0506	11.27
41.5	3.87091	2.6398	4.2227	12.74	119.9	3.68877	2.5317	4.0469	11.23
43.9	3.86300	2.6357	4.2133	12.67	122.5	3.68435	2.5285	4.0416	11.19
48.6	3.84812	2.6284	4.1988	12.56	128.4	3.67475	2.5228	4.0311	11.11
54.6	3.83025	2.6163	4.1831	12.40	133.3	3.66699	2.5175	4.0232	11.04
56.9	3.82377	2.6123	4.1786	12.35	138.1	3.65966	2.5124	4.0154	10.97
61.2	3.81195	2.6069	4.1647	12.26	143.0	3.65231	2.5077	4.0068	10.91
64.5	3.80341	2.6021	4.1566	12.19	143.7	3.65134	2.5072	4.0054	10.90
65.1	3.80189	2.6009	4.1549	12.17	148.4	3.64438	2.5029	3.9981	10.85
72.4	3.78365	2.5904	4.1393	12.03	151.6	3.63982	2.5015	3.994	10.82
76.0	3.77516	2.585	4.1333	11.96	151.7	3.63971	2.4999	3.992	10.80
81.3	3.76313	2.578	4.123	11.87	152.9	3.63802	2.4989	3.9908	10.79
84.7	3.75564	2.5733	4.1165	11.80	153.0	3.63785	2.5003	3.9861	10.79

**Table A. 6** Lattice parameters of  $\alpha$ -MoO<sub>2</sub> from Run 2.

$P_{\text{Au}}$ (GPa)	a (Å)	b (Å)	c (Å)	$\beta$ (°)	V (Å <sup>3</sup> /atom)
5.2	5.576	4.836	5.581	121.04	129.0
9.5	5.549	4.830	5.531	121.18	126.8
12.4	5.531	4.827	5.493	121.31	125.3
15.6	5.507	4.830	5.436	121.59	123.2
16.8	5.498	4.831	5.418	121.64	122.5
18.5	5.487	4.828	5.397	121.75	121.6
19.5	5.480	4.829	5.381	121.82	121.0
20.4	5.474	4.827	5.370	121.87	120.5
21.6	5.466	4.825	5.355	121.92	119.9
22.4	5.462	4.822	5.348	121.94	119.5
23.3	5.455	4.821	5.335	121.98	119.0
24.5	5.446	4.821	5.321	122.02	118.4
25.7	5.440	4.815	5.310	122.09	117.9
27.0	5.431	4.811	5.299	122.12	117.3
27.8	5.426	4.809	5.291	122.12	116.9
28.7	5.419	4.799	5.290	122.15	116.5
29.6	5.416	4.801	5.276	122.16	116.1
31.0	5.405	4.804	5.261	122.23	115.5
32.4	5.401	4.810	5.242	122.27	115.2



**Table A. 7** Lattice parameters of  $\alpha$ -MoO<sub>2</sub> from Run 3.

P <sub>Au</sub> (GPa)	a (Å)	b (Å)	c (Å)	$\beta$ (°)	V (Å <sup>3</sup> /atom)
17.2	5.496	4.847	5.384	121.90	121.8
15.2	5.507	4.848	5.410	121.78	122.8
14.2	5.514	4.850	5.423	121.71	123.4
13.3	5.520	4.850	5.437	121.68	123.9
12.5	5.525	4.850	5.449	121.62	124.3
12.1	5.529	4.849	5.456	121.58	124.6
12.0	5.529	4.850	5.459	121.57	124.7
12.1	5.529	4.850	5.458	121.58	124.7
11.9	5.527	4.851	5.455	121.55	124.6
12.3	5.528	4.850	5.455	121.59	124.6
12.5	5.527	4.852	5.451	121.62	124.5
12.6	5.526	4.851	5.450	121.64	124.4
13.9	5.518	4.852	5.430	121.71	123.7
14.6	5.514	4.854	5.421	121.76	123.4
15.0	5.511	4.853	5.414	121.77	123.1
15.3	5.510	4.853	5.410	121.79	122.9
16.4	5.501	4.853	5.394	121.84	122.3
18.5	5.492	4.854	5.371	121.99	121.4
22.5	5.467	4.848	5.326	122.13	119.5
24.1	5.459	4.839	5.312	122.19	118.8
23.8	5.461	4.841	5.315	122.18	118.9
22.2	5.466	4.841	5.330	122.05	119.6
22.0	5.470	4.842	5.332	122.08	119.7

6

7

**Table A. 8** Lattice parameters of  $\alpha$ -MoO<sub>2</sub> from Run 1.

$P_{\text{Au}}$ (GPa)	a (Å)	b (Å)	c (Å)	$\beta$ (°)	V (Å <sup>3</sup> /atom)
1.0	5.599	4.854	5.617	120.78	131.2
1.8	5.595	4.852	5.611	120.80	130.8
3.0	5.584	4.848	5.601	120.81	130.2
4.1	5.579	4.845	5.592	120.89	129.7
5.2	5.565	4.845	5.580	120.92	129.1
6.2	5.570	4.842	5.570	120.95	128.8
7.3	5.548	4.841	5.556	120.97	128.0
8.6	5.537	4.840	5.538	121.02	127.2
10.1	5.523	4.841	5.516	121.09	126.3
12.5	5.506	4.845	5.471	121.25	124.8
13.6	5.498	4.845	5.453	121.28	124.1
16.2	5.484	4.843	5.417	121.52	122.6
17.8	5.475	4.842	5.398	121.64	121.8

8

**Table A. 9** Lattice parameters of MoO<sub>2</sub> CaCl<sub>2</sub> phase.

P <sub>Au</sub> (GPa)	a (Å)	b (Å)	c (Å)	V (Å <sup>3</sup> /atom)
0.0	4.882	4.804	2.809	131.8
4.7	4.900	4.746	2.805	130.4
4.8	4.903	4.743	2.805	130.5
5.7	4.907	4.733	2.805	130.3
6.3	4.908	4.727	2.805	130.1
6.8	4.907	4.724	2.805	130.0
7.4	4.902	4.722	2.805	129.8
8.0	4.903	4.716	2.804	129.7
8.6	4.903	4.710	2.803	129.5
9.5	4.898	4.705	2.802	129.2
10.3	4.898	4.696	2.800	128.8
13.9	4.883	4.669	2.795	127.5
14.3	4.881	4.666	2.795	127.3
15.0	4.879	4.666	2.796	127.3
15.8	4.877	4.659	2.794	127.0
16.7	4.873	4.651	2.793	126.6
17.4	4.880	4.640	2.791	126.4
18.2	4.878	4.632	2.790	126.1
18.7	4.876	4.628	2.790	125.9
19.1	4.875	4.624	2.787	125.7
19.5	4.875	4.619	2.785	125.4
20.0	4.873	4.614	2.786	125.3
20.4	4.874	4.609	2.785	125.1
21.4	4.870	4.593	2.778	124.3
21.7	4.868	4.589	2.780	124.2
22.1	4.867	4.586	2.778	124.0
22.6	4.869	4.580	2.778	123.9
23.1	4.869	4.573	2.776	123.6
23.6	4.868	4.567	2.776	123.5
24.4	4.866	4.561	2.773	123.1
26.1	4.859	4.550	2.771	122.5

**Table A. 10** Lattice parameters of  $\alpha$ -ReO<sub>2</sub> from Run 1.

$P_{\text{Au}}$ (GPa)	a (Å)	b (Å)	c (Å)	$\beta$ (°)	V (Å <sup>3</sup> /atom)
0.0	5.607	4.818	5.543	120.47	129.2
1.1	5.595	4.814	5.538	120.63	128.4
3.0	5.586	4.806	5.502	120.21	127.6
3.9	5.583	4.795	5.475	120.18	126.8
5.0	5.571	4.790	5.515	120.73	126.4
7.1	5.555	4.788	5.456	120.14	125.6
9.1	5.534	4.785	5.431	120.22	124.4
10.7	5.522	4.785	5.405	120.24	123.2
11.6	5.515	4.785	5.393	120.28	122.8
12.6	5.507	4.785	5.379	120.30	122.4
13.0	5.500	4.783	5.367	120.30	122.0
14.4	5.492	4.780	5.353	120.35	121.2
14.9	5.489	4.780	5.344	120.36	120.8
15.9	5.482	4.778	5.330	120.37	120.4
16.9	5.474	4.775	5.316	120.39	120.0
17.7	5.467	4.775	5.303	120.40	119.6
19.0	5.461	4.773	5.287	120.43	118.8
20.2	5.453	4.772	5.267	120.45	118.0
21.5	5.452	4.764	5.259	120.49	117.6
22.3	5.444	4.764	5.246	120.46	117.2
23.0	5.443	4.758	5.246	120.48	117.2
24.1	5.431	4.753	5.231	120.45	116.4
25.0	5.429	4.748	5.224	120.49	116.0
25.8	5.424	4.746	5.216	120.47	115.6
27.8	5.411	4.742	5.191	120.49	114.8
29.1	5.405	4.737	5.180	120.50	114.4
33.2	5.380	4.732	5.131	120.55	112.4
30.3	5.394	4.736	5.163	120.52	113.6
25.0	5.440	4.765	5.223	120.65	116.4
20.2	5.461	4.760	5.270	120.56	118.0
14.9	5.490	4.770	5.340	120.49	120.4
6.4	5.500	4.850	5.470	121.7	124.0

10

**Table A. 11** Lattice parameters of  $\beta$ -ReO<sub>2</sub>.

11

12

$P_{\text{Au}}$ (GPa)	a (Å)	b (Å)	c (Å)	$\beta$ (°)	V (Å <sup>3</sup> /atom)
30.3	4.585	5.528	4.490	-	113.6
25.0	4.616	5.548	4.527	-	116.0
20.2	4.636	5.573	4.538	-	117.2
14.9	4.672	5.595	4.556	-	119.2
6.4	4.729	5.629	4.602	-	122.4
1.6	4.764	5.650	4.629	-	124.8
0.0	4.809	5.643	4.601	-	124.8

13

**Table A. 12** Lattice parameters of  $\alpha$ -ReO<sub>2</sub> from Run 2.

14

15

$P_{\text{Au}}$ (GPa)	a ( $\text{\AA}$ )	b ( $\text{\AA}$ )	c ( $\text{\AA}$ )	$\beta$ ( $^\circ$ )	V ( $\text{\AA}^3/\text{atom}$ )
35.4	5.396	4.706	5.164	120.68	113.2
35.4	5.398	4.703	5.170	120.75	113.2
35.5	5.398	4.700	5.166	120.68	113.2
48.6	5.326	4.680	5.059	120.64	109.2
50.2	5.326	4.672	5.057	120.70	109.2
50.7	5.322	4.675	5.048	120.67	108.8
51.7	5.323	4.670	5.048	120.75	108.8
57.0	5.313	4.651	5.040	121.12	107.2
59.2	5.307	4.645	5.030	121.19	106.8
64.4	5.292	4.630	5.000	121.23	105.2
67.5	5.286	4.611	4.994	121.34	104.8
68.7	5.282	4.609	4.992	121.44	104.4
70.0	5.281	4.600	4.985	121.39	104.0
71.3	5.276	4.601	4.983	121.54	103.6
72.4	5.275	4.592	4.977	121.46	103.6
73.7	5.272	4.589	4.966	121.44	103.2
75.1	5.272	4.583	4.968	121.59	102.8

16  
17  
18  
19  
20  
21  
22  
23  
24  
25  
26  
27  
28

**Table A. 13** Lattice parameters of TcO<sub>2</sub> from Run 1.

$P_{\text{Au}}$ (GPa)	a (Å)	b (Å)	c (Å)	$\beta$ (°)	V (Å <sup>3</sup> /atom)
0.45	5.6966	4.7116	5.5454	120.9	127.8
1.08	5.6939	4.7081	5.5483	120.8	127.7
2.31	5.6766	4.6831	5.5370	120.8	126.8
3.27	5.6704	4.6736	5.5316	120.8	126.0
5.12	5.6537	4.6495	5.5233	120.7	124.9
6.91	5.6423	4.6399	5.5120	120.6	123.9
8.75	5.6308	4.5944	5.5078	120.5	122.8
9.72	5.5956	4.5839	5.5041	120.4	121.7
10.89	5.5828	4.5259	5.5276	120.3	120.6
13.01	5.5612	4.4972	5.5250	120.2	119.4
14.03	5.5560	4.4804	5.5250	120.2	118.9
14.92	5.5400	4.4788	5.5140	120.1	118.4

29 Figure 1 reprinted from Journal of Applied Radiation and Isotopes, 63, 1, Zeev B. Alfassi, Flavia  
30 Groppi, Mauro L. Bonardi, Jeroen J.M. de Goeij, On the “artificial” nature of Tc and the “carrier-  
31 free” nature of  $^{99m}\text{Tc}$  from  $^{99}\text{Mo}/^{99m}\text{Tc}$  generators, 1, Copyright (2005), with permission from  
32 Elsevier.

33 Figure 2 reprinted from Reports on Progress in Physics, 80, Guoyin Shen and Ho Kwang Mao,  
34 High-pressure studies with x-rays using diamond anvil cells, 3, Copyright (2016), with permission  
35 from IOP Publishing.

36 Chapter 4 reprinted from the Journal of Physics and Chemistry of Solids, 95, Mast, D. S., Kim, E.,  
37 Siska, E. M., Poineau, F., Czerwinski, K. R., Lavina, B., and Forster, P. M., Equation of state for  
38 technetium from X-ray diffraction and first principle calculations. 6-11, Copyright (2016)



# References

- (1) Hayward, A. T. J. Compressibility Equations for Liquids: Comparative Study. *Br. J. Appl. Phys.* **1967**, *18*, 965–977.
- (2) Mendeleev, D. No Titl. *Zeitschrift fur Chemie* **1869**, *12*, 405–406.
- (3) Perrier, C.; Segrè, E. Some Chemical Properties of Element 43. I. *J. Chem. Phys.* **1937**, *5* (3), 712.
- (4) Perrier, C.; Segrè, E. Some Chemical Properties of Element 43. II. *J. Chem. Phys.* **1939**, *7* (3), 155.
- (5) Perrier, C.; Segrè, E. Technetium: The Element of Atomic Number 43. *Nature*. 1947, pp 24–24.
- (6) Laboratory, B. N. Chart of Nuclides.
- (7) Nuclear Energy Agency [www.nea.org](http://www.nea.org).
- (8) Icenhower, J.; Martin, W.; Qafoku, N.; Zachara, J. *The Geochemistry of Technetium: A Summary of the Behavior of an Artificial Element in the Natural Environment*; 2008.
- (9) Cotton, F. A.; Wilkinson, G. *Advanced Inorganic Chemistry: A Comprehensive Text*; 1972.
- (10) Childs, B. C.; Braband, H.; Lawler, K.; Mast, D. S.; Bigler, L.; Stalder, U.; Forster, P. M.; Czerwinski, K. R.; Alberto, R.; Sattelberger, A. P.; Poineau, F. Ditechnetium Heptoxide Revisited: Solid-State, Gas-Phase, and Theoretical Studies. *Inorg. Chem.* **2016**, *55* (20), 10445–10452.
- (11) MacDiarmid, A. G.; Herrell, A. Y.; Busey, R. H.; Gayer, K. H.; Schowochau, K.; Gutzeit, S. Technetium(VII) Oxides. In *Inorganic Syntheses*; 1977.
- (12) Gibson, J. K. High-Temperature Oxides and Hydroxide Vapor Species of Technetium. *Radiochim. Acta* **1993**, *60* (2–3), 121.
- (13) Rard, J. A. Current Status of the Thermodynamic Data for Technetium and Its Compounds and Aqueous Species. *J. Nucl. Radiochem. Sci.* **2005**, *6* (3), 197–204.
- (14) Liu, L.-G.; Takahashi, T.; Bassett, W. A. Effect of Pressure and Temperature on the Lattice Parameters of Rhenium. *J. Phys. Chem. Solids* **1970**, *31*, 1345–1351.
- (15) Bridgman, P. Miscellaneous Effects of Pressure on Miscellaneous Substances. *Proc. Am.*

- Acad. Arts Sci.* **1955**, 84 (1), 111–129.
- (16) Dubrovinsky, L.; Dubrovinskaia, N.; Prakapenka, V. B.; Abakumov, A. M. Implementation of Micro-Ball Nanodiamond Anvils for High-Pressure Studies above 6 Mbar. *Nat. Commun.* **2012**, 3, 1163.
  - (17) Yang, L.; Karandikar, A.; Boehler, R. Flash Heating in the Diamond Cell: Melting Curve of Rhenium. *Rev. Sci. Instrum.* **2012**, 83 (6), 1–6.
  - (18) Vohra, Y. K.; Duclos, S. J.; Ruoff, A. L. High-Pressure x-Ray Diffraction Studies on Rhenium up to 216 GPa (2.16 Mbar). *Phys. Rev. B* **1987**, 36 (18), 9790–9792.
  - (19) Singh, P.; Verma, M. P. Equation of State of Rhenium. *Proc. Natl. Acad. Sci. India* **1994**, 64 (1), 123–134.
  - (20) Jeanloz, R.; Godwal, B. K.; Meade, C. Static Strength and Equation of State of Rhenium at Ultra-High. *Nature* **1991**, 349, 687–689.
  - (21) Sikka, S. K.; Vijayakumar, V. Theoretical Isothermal Equation of State of Rhenium. *Phys. Rev. B* **1988**, 38 (15), 10926–10928.
  - (22) Zha, C.-S.; Bassett, W. A.; Shim, S.-H. Rhenium, an in Situ Pressure Calibrant for Internally Heated Diamond Anvil Cells. *Rev. Sci. Instrum.* **2004**, 75, 2409.
  - (23) Anzellini, S.; Dewaele, A.; Occelli, F.; Loubeyre, P.; Mezouar, M. Equation of State of Rhenium and Application for Ultra High Pressure Calibration. *J. Appl. Phys.* **2014**, 115 (4), 043511.
  - (24) Walzer, U. Elastic and Bonding Properties of Transition Metals. *Phys. Status Solidi* **1984**, 55 (125), 55–64.
  - (25) Guillermet, A.; Grimvall, G.; Guillermet, A.; Grimvall, G. Thermodynamic Properties of Technetium. *J. Less Common Met.* **1989**, 147, 195–211.
  - (26) Wojciechowski, K. F. Bulk Properties of the Stabilized Uniform “metallic” Electron Gas in Transition Metals. *Phys. B* **1996**, 229 (1), 55–62.
  - (27) Weck, P. F.; Kim, E.; Czerwinski, K. R. Interplay between Structure, Stoichiometry and Properties of Technetium Nitrides. *Dalt. Trans.* **2011**, 40 (25), 6738–6744.
  - (28) Love, G. R.; Koch, C. C.; Whaley, H. L.; McNutt, Z. R. Elastic Moduli and Debye Temperature of Polycrystalline Technetium by Ultrasonic Velocity Measurements. *J. Less Common Met.* **1970**, 20, 73–75.
  - (29) Sekula, S. T.; Kernohan, R. H.; Love, G. R. Superconducting Properties of Technetium. *Phys. Rev.* **1967**, 155 (2), 364–369.

- (30) Shelton, R. N.; Smith, T. F.; Koch, C. C.; Gardner, W. E. Tc and Its Pressure Dependence for Technetium-Based h.c.p. Solid Solution Alloys. *J. Phys. F Met. Phys.* **1975**, *5*, 1916–1930.
- (31) Alekseyevskiy, N. Y.; Balakhovskiy, O. A.; Kirillov, I. V. Concerning the Superconductivity of Technetium and Some of Its Alloys. *Phys. Met. Metallogr.* **1975**, *40* (1), 38–42.
- (32) Chu, C. W.; Gardner, W. E.; Smith, T. F.  $\partial T_c/\partial P$  for Technetium and a Comment on Its Sign in Relation to the Other Transition Metal Superconductors. *Phys. Lett.* **1968**, *26A* (12), 627–628.
- (33) Chu, C. W.; Smith, T. F.; Gardner, W. E. Superconductivity of Rhenium and Some Rhenium-Osmium Alloys at High Pressure. *Phys. Rev. Lett.* **1968**, *20* (5), 198.
- (34) Porter, R. A.; McMillan, W. G. Effect of Compression on the Decay Rate of Tc99m Metal. *Phys. Rev.* **1960**, *117* (3), 795–800.
- (35) Gono, Y. Change of Nuclear Decay Constant under Ultra-High Pressure. *Koatsuryoku no Kagaku to Gijutsu* **2001**, *11* (4), 311–314.
- (36) Mazaki, H.; Nagatomo, T.; Shimizu, S. Effect of Pressure on the Decay Constant of 99m-Tc. *Phys. Rev. C* **1972**, *5* (5), 1718–1724.
- (37) Gonschorek, W.; Feld, R. Neutron Diffraction Study of the Thermal and Oxygen Position Parameters in Rutile. *Zeitschrift Fur Krist. - Cryst. Mater.* **1982**, *161* (1–2), 1.
- (38) Romanov, D. P.; Skrobot, V. N. Distortions of Octahedra in Rutile-Type Structures of Transition Element Dioxides. *Glas. Phys. Chem.* **2009**, *35* (5), 518–524.
- (39) Magneli, A.; Andersson, G. On the MoO<sub>2</sub> Structure Type. *Acta Chem. Scand.* **1955**, 1378–1381.
- (40) Marinder, B.; Magneli, A. Metal-Metal Bonding in Some Transition Metal Dioxides. *Acta Chem. Scand* **1957**, *11*, 1635–1640.
- (41) Chisholm, M. H.; Macintosh, A. M. No Title. *Chem. Rev.* **2005**, *105*, 2949–2976.
- (42) Andersson, G. Studies on Vanadium Oxides. *Acta Chem. scandinavica* **1956**, *10*, 623–628.
- (43) Magneli, A.; Andersson, G. Identification of Molybdenum and Tungsten Oxides by X-Ray Powder Patterns. *Anal. Chem.* **1952**, *24* (12), 1998–2000.
- (44) Rodriguez, E. E.; Poineau, F.; Llobet, A.; Sattelberger, A. P.; Bhattacharjee, J.; Waghmare, U. V.; Hartmann, T.; Cheetham, A. K. Structural Studies of TcO<sub>2</sub> by Neutron Powder Diffraction and First-Principles Calculations. *J. Am. Chem. Soc.* **2007**, *129* (33), 10244–

10248.

- (45) Corrêa, H. P. S.; Cavalcante, I. P.; Martinez, L. G.; Orlando, C. G. P.; Orlando, M. T. D. Refinement of Monoclinic ReO<sub>2</sub> Structure from XRD by Rietveld Method Rietveld. *Brazilian J. Phys.* **2004**, *34* (3B), 1208–1210.
- (46) Seisenbaeva, G. A.; Sundberg, M.; Nygren, M.; Dubrovinsky, L.; Kessler, V. G. Thermal Decomposition of the Methoxide Complexes MoO(OMe)<sub>4</sub>, Re<sub>4</sub>O<sub>6</sub>(OMe)<sub>12</sub> and (Re<sub>1-x</sub>Mo<sub>x</sub>)O<sub>6</sub>(OMe)<sub>12</sub> ( $0.24 \leq x \leq 0.55$ ). *Mater. Chem. Phys.* **2004**, *87* (1), 142–148.
- (47) Becker, N.; Dronskowski, R. A First-Principles Study on New High-Pressure Metastable Polymorphs of MoO<sub>2</sub>. *J. Solid State Chem.* **2016**, *237*, 404–410.
- (48) Lüdtke, T.; Wiedemann, D.; Efthimiopoulos, I.; Becker, N.; Seidel, S.; Janka, O.; Pöttgen, R.; Dronskowski, R.; Koch-Müller, M.; Lerch, M. HP-MoO<sub>2</sub>: A High-Pressure Polymorph of Molybdenum Dioxide. *Inorg. Chem.* **2017**, *56* (4), 2321–2327.
- (49) Zhang, C.; Zou, X.; Du, Z.; Gu, J.; Li, S.; Li, B.; Yang, S. Atomic Layers of MoO<sub>2</sub> with Exposed High-Energy (010) Facets for Efficient Oxygen Reduction. *Small* **2018**, *1703960* (Ldmd), 1703960.
- (50) Xia, C.; Zhou, Y.; Velusamy, D. B.; Farah, A. A.; Li, P.; Jiang, Q.; Odeh, I. N.; Wang, Z.; Zhang, X.; Alshareef, H. N. Anomalous Li Storage Capability in Atomically Thin Two-Dimensional Sheets of Nonlayered MoO<sub>2</sub>. *Nano Lett.* **2018**, *acs.nanolett.7b05298*.
- (51) Liu, W.; Li, X.; Li, W.; Zhang, Q.; Bai, H.; Li, J.; Xi, G. Highly Stable Molybdenum Dioxide Nanoparticles with Strong Plasmon Resonance Are Promising in Photothermal Cancer Therapy. *Biomaterials* **2018**, *163*, 43–54.
- (52) Sa, B.; Miao, N.; Sun, Z.; Wu, B. Polyhedral Transformation and Phase Transition in TcO<sub>2</sub>. *RSC Adv.* **2015**, *5* (3), 1690–1696.
- (53) Sa, B.; Yang, H.; Miao, N.; Hu, K.; Zhou, J.; Wu, B.; Sun, Z. Pressure-Induced Destabilization and Anomalous Lattice Distortion in TcO<sub>2</sub>. *Inorg. Chem.* **2017**, *56* (16), 9973–9978.
- (54) Darab, J. G.; Smith, P. A. Chemistry of Technetium and Rhenium Species during Low-Level Radioactive Waste Vitrification. *Chem. Mater.* **1996**, *8* (5), 1004–1021.
- (55) Taylor, C. D. Oxidation of Technetium Metal as Simulated by First Principles. *J. Phys. Chem. C* **2014**, *118*, 10017–10023.
- (56) Kuo, E. Y.; Qin, M. J.; Thorogood, G. J.; Whittle, K. R.; Lumpkin, G. R.; Middleburgh, S. C. Technetium and Ruthenium Incorporation into Rutile TiO<sub>2</sub>. *J. Nucl. Mater.* **2013**, *441* (1–3), 380–389.

- (57) Johnstone, E. V.; Poineau, F.; Forster, P. M.; Ma, L.; Hartmann, T.; Cornelius, A.; Antonio, D.; Sattelberger, A. P.; Czerwinski, K. R. Technetium Tetrachloride Revisited: A Precursor to Lower-Valent Binary Technetium Chlorides. *Inorg. Chem.* **2012**, *51* (15), 8462–8467.
- (58) Sterks, M.; Gill, S.; Sterns, M. The Preparation and Properties of Pertechnetyl Fluoride, TcO<sub>3</sub>F. **1970**, *525* (1869), 1619–1625.
- (59) Magnéli, A. Studies on Rhenium Oxides. *Acta Chem. Scand.* **1957**, *11*, 28–33.
- (60) Ivanovskii, a. L.; Chupakhina, T. I.; Zubkov, V. G.; Tyutyunnik, A. P.; Krasilnikov, V. N.; Bazuev, G. V.; Okatov, S. V.; Lichtenstein, A. I. Structure and Electronic Properties of New Rutile-like Rhenium (IV) Dioxide ReO<sub>2</sub>. *Phys. Lett. A* **2005**, *348* (1–2), 66–70.
- (61) Yan-Ling, L.; Zhi, Z. Structural , Elastic and Electronic Properties of ReO<sub>2</sub>. *Chinese Phys. Lett.* **2008**, *25* (11), 4086.
- (62) Shiyong, G. Glass Powder for Solar Cell Back Silver Paste and Preparation Method Thereof. CN 106946463, 2017.
- (63) Yi, J.; Miller, J. T.; Zemlyanov, D. Y.; Zhang, R.; Dietrich, P. J.; Ribeiro, F. H.; Suslov, S.; Abu-Omar, M. M. A Reusable Unsupported Rhenium Nanocrystalline Catalyst for Acceptorless Dehydrogenation of Alcohols through  $\gamma$ -C-H Activation. *Angew. Chemie - Int. Ed.* **2014**, *53* (3), 833–836.
- (64) Yasuhiro, I.; Youzhu, Y.; Takafumi, S. Selective Oxidation Catalysts Containing Rhenium Oxide and Preparation of Partially Oxideized Lower Alcohols and Nitriles Usin Them. JP 2001353443, 2007.
- (65) Orlando, M. T. D.; Cunha, A. G.; Bud'ko, S. L.; Sin, A.; Martinez, L. G.; Vanoni, W.; Belich, H.; Obradors, X.; Emmerich, F. G.; Baggio-Saitovitch, E. Hg(0.95)Re(0.05)Ba(2)Ca(2)Cu(3)O(8+ $\delta$ ) Superconductor: Sample Preparation and Transport Properties under Hydrostatic Pressure. *Supercond. Sci. Technol.* **2000**, *13* (2), 140–147.
- (66) Yakinci, M. E.; Aksan, M. A.; Balci, Y. Fabrication and Properties of (Hg<sub>0.8</sub>Re<sub>0.2</sub>)Ba<sub>2</sub>Ca<sub>2</sub>Cu<sub>3</sub>O<sub>x</sub> Superconducting Thick Films. *Supercond. Sci. Technol.* **2005**, *18* (4), 494–502.
- (67) Wendel, J. Thermodynamics and Kinetics of Tungsten Oxidation and Tungsten Oxide Sublimation in the Temperature Interval 200°–1100°C. *Diploma Work* **2014**, No. October.
- (68) Shu, W. Y.; Ellis, B.; Doumerc, J.-P.; Pouchard, M.; Hagenmuller, P. Synthesis and X-Ray Characterization of Double Oxides of the Formula Cr<sub>1</sub>-XW<sub>1+x</sub>O<sub>4</sub>. *Z. Anorg. Allg. Chem* **1989**, *569*, 153–157.
- (69) Nobuaki, T. Group-IIIA-Nitride Semiconductor Devices. US 6043514, 2000.

- (70) Boyd, G. E.; Cobble, J. W.; Nelson, C. M.; Jr, W. T. S.; Boyd, G. E.; Cobble, J. W.; Nelson, C. M.; Smith, W. T., J.; Boyd, G. E.; Cobble, J. W.; Boyd, G. E.; Cobble, J. W.; Nelson, C. M.; Smith, W. T., J. Chemistry of Technetium. I. Preparation of Technetium Heptoxide. *J. Am. Chem. Soc.* **1952**, *74*, 556–557.
- (71) Smith, W. T.; Cobble, J. W.; Boyd, G. E. Thermodynamic Properties of Technetium and Rhenium Compounds. I. Vapor Pressures of Technetium Heptoxide, Pertechnic Acid and Aqueous Solutions of Pertechnic Acid. *J. Am. Chem. Soc.* **1953**, *75* (23), 5773–5776.
- (72) Krebs, B. Technetium (VII) Oxide: A Transition Metal Oxide with a Molecular Structure in the Solid State. *Angew. Chemie Int. Ed.* **1969**, *8* (5), 381–382.
- (73) Ke, J.; Qiang, W.; Hua-Yun, G.; Ling-Cang, C.; Fu-Qian, J. A Revised Ruby Pressure Scale up to 160 GPa. *Chinese J. High Press. Phys.* **2012**, *26* (6).
- (74) Jenei, Z.; Cynn, H.; Visbeck, K.; Evans, W. J. High-Temperature Experiments Using a Resistively Heated High-Pressure Membrane Diamond Anvil Cell. *Rev. Sci. Instrum.* **2013**, *84*, 0–6.
- (75) Kantor, I.; Prakapenka, V.; Kantor, A.; Dera, P.; Kurnosov, A.; Sinogeikin, S.; Dubrovinskaia, N.; Dubrovinsky, L. BX90: A New Diamond Anvil Cell Design for X-Ray Diffraction and Optical Measurements. *Rev. Sci. Instrum.* **2012**, *83*, 125102.
- (76) Boehler, R.; De Hantsetters, K. New Anvil Designs in Diamond-Cells. *High Press. Res.* **2004**, *24* (3), 391–396.
- (77) Holzapfel, W. B. Physics of Solids under Strong Compression. *Rep. Prog. Phys.* **1996**, *59*, 29–90.
- (78) Vinet, P.; Smith, J. R.; Ferrante, J.; Rose, J. H. Temperature Effects on the Universal Equation of State of Solids. *Phys. Rev. B* **1987**, *35* (4), 1945–1953.
- (79) Birch, F. Finite Elastic Strain of Cubic Crystals. *Phys. Rev.* **1947**, *71* (11), 809–824.
- (80) Murnaghan, F. D. The Compressibility of Media under Extreme Pressures. *Proc. N. A. S.* **1944**, *30*, 244–247.
- (81) Dubrovinskaia, N.; Dubrovinsky, L.; Solopova, N. A.; Abakumov, A.; Turner, S.; Hanfland, M.; Bykova, E.; Bykov, M.; Prescher, C.; Prakapenka, V. B.; Petitgirard, S.; Chuvashova, I.; Gasharova, B.; Mathis, Y.; Ershov, P.; Snigireva, I.; Snigirev, A. Terapascal Static Pressure Generation with Ultrahigh Yield Strength Nanodiamond. *Mater. Sci.* **2016**, *2* (7), e1600341.
- (82) Hammersley, A. P.; Svensson, S. O.; Hanfland, M.; Fitch, A. N.; Hausermann, D. Two-Dimensional Detector Software: From Real Detector to Idealised Image or Two-Theta Scan. *High Press. Res.* **1996**, *14*, 235–248.

- (83) Angel, R. J.; Alvaro, M.; Gonzalez-Platas, J. EosFit7c and a Fortran Module (Library) for Equation of State Calculations. *Zeitschrift für Krist. - Cryst. Mater.* **2014**, *229* (5), 405–419.
- (84) Bruker. APEX2. Bruker AXS Inc: Madison, Wisconsin, USA 2012.
- (85) Sheldrick, G. M. A Short History of SHELX. *Acta Crystallogr. Sect. A Found. Crystallogr.* **2008**, *64* (1), 112–122.
- (86) Bruker. SADABS. Bruker AXS Inc.: Madison, Wisconsin, USA 2001.
- (87) Dolomanov, O. V.; Bourhis, L. J.; Gildea, R. J.; Howard, J. A. K.; Puschmann, H. OLEX2: A Complete Structure Solution, Refinement and Analysis Program. *J. Appl. Crystallogr.* **2009**, *42* (2), 339–341.
- (88) Mooney, R. C. L. The Crystal Structure of Element 43. *Acta Crystallogr.* **1948**, *1*, 161–162.
- (89) Marples, J. A. C. A Low Temperature X-Ray Investigation of Technetium and the Tc-Mo A-15 Compound. *Phys. Lett.* **1972**, *41A* (4), 307–308.
- (90) Weck, P. F.; Kim, E. Thermodynamics of Technetium: Reconciling Theory and Experiment Using Density Functional Perturbation Analysis. *Dalt. Trans.* **2015**, *44* (28), 12735–12742.
- (91) Lam, D.; Darby, J.; Downey, J.; Norton, L.  $\alpha$ -Manganese Phases Containing Technetium-99. *Nature* **1961**, *192*, 744.
- (92) Muller, O.; White, W.; Roy, R. Crystal Chemistry of Some Technetium-Containing Oxides. *J. Inorg. Nucl. Chem.* **1964**, *26* (1962), 2075–2086.
- (93) Baker, D. E. The Thermal Conductivity of Technetium. *J. Less Common Met.* **1965**, *8* (6), 435–436.
- (94) Trzebiatowski, W.; Rudzinski, J. The Composition and Structure of Technetium Nitride and Technetium Borides. *J. Less Common Met.* **1964**, *6* (3), 244–245.
- (95) Koch, C. C.; Love, G. R. An Investigation of the Vanadium-Technetium Alloy System. *J. less-common Met.* **1968**, *15*.
- (96) Spitsyn, V. I.; Ponyatovskii, E. G.; Antonov, V. E.; Belash, I. T.; Balakhovskii, O. A. Phase Transformations in the Technetium-Hydrogen System at High Pressure. *Dokl. Akad. Nauk SSSR* **1979**.
- (97) Giorgi, A. L.; Szklarz, E. G. Superconductivity of Technetium and Technetium Carbide. *J. Less Common Met.* **1966**, *11*, 455–456.
- (98) Haines, H. R.; Potter, P. E.; Rand, M. H. *Thermodynamics of Nuclear Materials*; IAEA: Vienna, 1980; Vol. 1.

- (99) Rard, J. A.; Rand, M. H.; Anderegg, G.; Wanner, H. *Chemical Thermodynamics of Technetium*; Sandino, M. C. A., Osthols, E., Eds.; Elsevier: Amsterdam, North-Holland, 1999; Vol. 3.
- (100) Shirasu, Y.; Minato, K. Thermal Expansions of Technetium-Ruthenium Alloys. *J. Alloys Compd.* **2002**, *335* (1–2), 224–227.
- (101) Lee, P. L.; Shu, D.; Ramanathan, M.; Preissner, C.; Wang, J.; Beno, M. A.; Von Dreele, R. B.; Ribaud, L.; Kurtz, C.; Antao, S. M.; Jiao, X.; Toby, B. H. A Twelve-Analyzer Detector System for High-Resolution Powder Diffraction. *J. Synchrotron Radiat.* **2008**, *15* (5), 427–432.
- (102) Schiebold, E. The Crystal Structure of Periclase. *Zeitschrift Für Krist.* **1921**, *56*, 430.
- (103) Mast, D. S.; Kim, E.; Siska, E. M.; Poineau, F.; Czerwinski, K. R.; Lavina, B.; Forster, P. M. Equation of State for Technetium from X-Ray Diffraction and First-Principle Calculations. *J. Phys. Chem. Solids* **2016**, *95*, 6–11.
- (104) Baria, J. K.; Gajjar, P. N.; Jani, A. R. Equation of State, Binding Energies, Bulk Modulus and Gruneisen Constants of 3d, 4d, and 5d Transition Metals. *Fiz. B* **2003**, *1* (12), 23–40.
- (105) Silva, G. W. C.; Poineau, F.; Ma, L.; Czerwinski, K. R. Application of Electron Microscopy in the Observation of Technetium and Technetium Dioxide Nanostructures. *Inorg. Chem.* **2008**, *47* (24), 11738–11744.
- (106) Angel, R. J.; Bujak, M.; Zhao, J.; Gatta, G. D.; Jacobsen, S. D. Effective Hydrostatic Limits of Pressure Media for High-Pressure Crystallographic Studies. *J. Appl. Crystallogr.* **2007**, *40* (1), 26–32.
- (107) Kresse, G.; Furthmuller, J. Efficient Iterative Schemes for Ab Initio Total-Energy Calculations Using a Plane-Wave Basis Set. *Phys. Rev. B* **1996**, *54* (16), 11169–11186.
- (108) Perdew, J. P.; Chevary, J. A.; Vosko, S. H.; Jackson, K. A.; Pederson, M. R.; Singh, D. J.; Fiolhais, C. Atoms, Molecules, Solids, and Surfaces: Applications of the Generalized Gradient Approximation for Exchange and Correlation. *Phys. Rev. B* **1992**, *46* (11), 6671–6687.
- (109) Perdew, J. P.; Wang, Y. Accurate and Simple Analytic Representation of the Electron-Gas Correlation Energy. *Phys. Rev. B* **1992**, *45* (23), 13244–13249.
- (110) Weck, P. F.; Kim, E.; Czerwinski, K. R.; Tomanek, D. Structural and Magnetic Properties of Tcn@C60 Endohedral Metalofullerenes: First-Principles Predictions. *Phys. Rev. B* **2010**, *81* (12), 125448.
- (111) Blöchl, P. E. Projector Augmented-Wave Method. *Phys. Rev. B* **1994**, *50* (24), 17953–17979.



- (112) Kresse, G.; Joubert, D. From Ultrasoft Pseudopotentials to the Projector Augmented-Wave Method. *Phys. Rev. B* **1999**, *59* (3), 1758–1774.
- (113) Methfessel, M.; Paxton, A. T. High-Precision Sampling for Brillouin-Zone Integration in Metals. *Phys. Rev. B* **1989**, *40* (6), 3616–3621.
- (114) Monkhorst, H. J.; Pack, J. D. Special Points for Brillouin-Zone Integrations\*. *Phys. Rev. B* **1976**, *13* (12), 5188–5192.
- (115) Takemura, K.; Dewaele, A. Isothermal Equation of State for Gold with a He-Pressure Medium. *Phys. Rev. B* **2008**, *78* (10), 104119.
- (116) Dewaele, A.; Torrent, M.; Loubeyre, P.; Mezouar, M. Compression Curves of Transition Metals in the Mbar Range: Experiments and Projector Augmented-Wave Calculations. *Phys. Rev. B* **2008**, *78* (10), 104102.
- (117) Klotz, S.; Chervin, J.-C.; Munsch, P.; Le Marchand, G. Hydrostatic Limits of 11 Pressure Transmitting Media. *J. Phys. D. Appl. Phys.* **2009**, *42* (7), 075413.
- (118) Overton, W. C. Relation between Ultrasonically Measured Properties and the Coefficients in the Solid Equation of State. *J. Chem. Phys.* **1962**, *37* (1), 116.
- (119) Dubrovinsky, L.; Glazyrin, K.; McCammon, C.; Narygina, O.; Greenberg, E.; Übelhack, S.; Chumakov, A. I.; Pascarelli, S.; Prakapenka, V.; Bock, J.; Dubrovinskaia, N. Portable Laser-Heating System for Diamond Anvil Cells. *J. Synchrotron Radiat.* **2009**, *16* (6), 737–741.
- (120) Manghnani, M. H.; Katahara, K.; Fisher, E. S. Ultrasonic Equation of State of Rhenium. *Phys. Rev. B* **1974**, *9* (4), 1421–1431.
- (121) McQueen, R. G.; Marsh, S. P.; Taylor, J. W.; Fritz, J. N.; Carter, W. J. The Equation of State of Solids from Shock Wave Studies. In *High Velocity Impact Phenomena*; Kinslow, R., Ed.; Academic Press: New York, 1970; pp 293–417.
- (122) de Jong, M.; Olmsted, D. L.; van de Walle, A.; Asta, M. First-Principles Study of the Structural and Elastic Properties of Rhenium-Based Transition-Metal Alloys. *Phys. Rev. B* **2012**, *86* (22), 224101.
- (123) Sokolova, T. S.; Dorogokupets, P. I.; Litasov, K. D. Self-Consistent Pressure Scales Based on the Equations of State for Ruby, Diamond, MgO, B2-NaCl, as Well as Au, Pt, and Other Metals to 4 Mbar and 3000 K. *Russ. Geol. Geophys.* **2013**, *54* (2), 181–199.
- (124) Syassen, K. Ruby under Pressure. *High Press. Res.* **2008**, *28* (April 2014), 75–126.
- (125) Takemura, K.; Dewaele, A. Isothermal Equation of State for Gold with a He-Pressure Medium. *Phys. Rev. B* **2008**, *78*, 104119.

- (126) Yokoo, M.; Kawai, N.; Nakamura, K. G.; Kondo, K. I.; Tange, Y.; Tsuchiya, T. Ultrahigh-Pressure Scales for Gold and Platinum at Pressures up to 550 GPa. *Phys. Rev. B - Condens. Matter Mater. Phys.* **2009**, *80*, 1–9.
- (127) Duffy, T.; Shen, G.; Heinz, D.; Shu, J.; Ma, Y.; Mao, H.-K.; Hemley, R.; Singh, A. Lattice Strains in Gold and Rhenium under Nonhydrostatic Compression to 37 GPa. *Phys. Rev. B* **1999**, *60* (22), 15063–15073.
- (128) Peterson, J. H.; Honnell, K. G.; Greeff, C.; Johnson, J. D.; Boettger, J.; Crockett, S. Global Equation of State for Copper. *AIP* **2012**, *1426*, 763.
- (129) Greeff, C. W.; Graf, M. J.; Boettger, J. C.; Johnson, J. D. High Accuracy Equations of State for Standards. *AIP Conf. Proceedingse* **2006**, *845*, 89.
- (130) Zhao, Z. L.; Bao, K.; Duan, D. F.; Jin, X. L.; Tian, F. B.; Li, D.; Liu, B. B.; Cui, T. Ideal Stoichiometric Technetium Nitrides under Pressure: A First-Principles Study. *J. Superhard Mater.* **2014**, *36* (4), 288–295.
- (131) Liang, Y.; Li, C.; Guo, W.; Zhang, W. First-Principles Investigation of Technetium Carbides and Nitrides. *Phys. Rev. B - Condens. Matter Mater. Phys.* **2009**, *79*, 1–5.
- (132) Zhao, Y.-R.; Zhang, G.-T.; Yan, H.-Y.; Bai, T.-T.; Zheng, B.-B.; Yuan, Y.-Q. First-Principles Investigations of the Structure and Physical Properties for New TcN Crystal Structure. *Mol. Phys.* **2016**, *8976* (April), 1–8.
- (133) Rivers, M.; Prakapenka, V.; Kubo, A.; Pullins, C.; Holl, C.; Jacobsen, S. The COMPRES/GSECARS Gas-Loading System for Diamond Anvil Cells at the Advanced Photon Source. *High Press. Res.* **2008**, *28* (3), 273–292.
- (134) Childs, B. C.; Poineau, F.; Czerwinski, K. R.; Sattelberger, A. P. The Nature of the Volatile Technetium Species Formed during Vitrification of Borosilicate Glass. *J. Radioanal. Nucl. Chem.* **2015**, *306* (2), 417–421.
- (135) Westsik Jr., J. H.; Cantrell, K. J.; Serne, R. J.; Qafoku, N. P. *Technetium Immobilization Forms Literature Survey*; 2014.
- (136) Childs, B. C.; Lawler, K. V.; Braband, H.; Mast, D. S.; Bigler, L.; Stalder, U.; Peterson, D. R.; Jansen, A.; Forster, P. M.; Czerwinski, K. R.; Alberto, R.; Sattelberger, A. P.; Poineau, F. The Nature of the Technetium Species Formed During the Oxidation of Technetium Dioxide with Oxygen and Water. *Eur. J. Inorg. Chem.* **2018**, *2018* (9), 1137–1144.
- (137) Lawler, K. V.; Childs, B. C.; Czerwinski, K. R.; Sattelberger, A. P.; Poineau, F.; Forster, P. M. Unraveling the Mystery of “Tech Red” – a Volatile Technetium Oxide. *Chem. Commun.* **2018**, *54* (10), 1261–1264.
- (138) Childs, B. C.; Braband, H.; Lawler, K. V.; Mast, D. S.; Bigler, L.; Stadler, U.; Forster, P.

- M.; Czerwinski, K. R.; Alberto, R.; Sattelberger, A. P.; Poineau, F. Ditechnetium Heptoxide Revisited: Solid-State, Gas-Phase, and Theoretical Studies. *Inorg. Chem.* **2016**.
- (139) Simon, A.; Dronskowski, R.; Krebs, B.; Hettich, B. The Crystal Structure of Mn<sub>2</sub>O<sub>7</sub>. *Angew. Chem. Int. Ed. Engl.* **1987**, *26* (2), 139–140.
- (140) Pley, M.; Wickleder, M. S. Two Crystalline Modifications of RuO<sub>4</sub>. *J. Solid State Chem.* **2005**, *178* (10), 3206–3209.
- (141) Ruff, O.; Tschirch, F. W. Über Die Fluoride Des Osmiums. *Berichte der Dtsch. Chem. Gesellschaft* **1913**, *46* (1), 929–949.
- (142) Lawler, K. V.; Childs, B. C.; Mast, D. S.; Czerwinski, K. R.; Sattelberger, A. P.; Poineau, F.; Forster, P. M. Molecular and Electronic Structures of M<sub>2</sub>O<sub>7</sub> (M=Mn, Tc, Re). *Inorg. Chem.* **2017**, *56* (5), 2448–2458.
- (143) Hohenberg, P.; Kohn, W. Inhomogeneous Electron Gas. *Phys. Rev. B* **1964**, *136* (3B), 864–871.
- (144) Kohn, W.; Sham, L. J. Self-Consistent Equations Including Exchange and Correlation Effects\*. *Phys. Rev. A* **1965**, *140* (4A), 1133–1138.
- (145) Allen, M. P.; Tildesley, D. J. *Computer Simulation of Liquids*; Oxford University Press: New York, 1991.
- (146) Parrinello, M.; Rahman, A. Crystal Structure and Pair Potentials: A Molecular-Dynamics Study. *Phys. Rev. Lett.* **1980**, *45* (14), 1196–1199.
- (147) Parrinello, M.; Rahman, A. Polymorphic Transitions in Single Crystals: A New Molecular Dynamics Method. *J. Appl. Phys.* **1981**, *52* (12), 7182–7190.
- (148) Perdew, J. P.; Burke, K.; Ernzerhof, M. Generalized Gradient Approximation Made Simple. *Phys. Rev. Lett.* **1996**, *77* (18), 3865–3868.
- (149) Grimme, S.; Antony, J.; Ehrlich, S.; Krieg, H. A Consistent and Accurate Ab Initio Parametrization of Density Functional Dispersion Correction (DFT-D) for the 94 Elements H-Pu. *J. Chem. Phys.* **2010**, *132*, 1–19.
- (150) Lejaeghere, K.; Bihlmayer, G.; Björkman, T.; Blaha, P.; Blügel, S.; Blum, V.; Caliste, D.; Castelli, I. E.; Clark, S. J.; Dal Corso, A.; de Gironcoli, S.; Deutsch, T.; Dewhurst, J. K.; Di Marco, I.; Draxl, C.; Dułak, M.; Eriksson, O.; Flores-Livas, J. A.; Garrity, K. F.; Genovese, L.; Giannozzi, P.; Giantomassi, M.; Goedecker, S.; Gonze, X.; Grånäs, O.; Gross, E. K. U.; Gulans, A.; Gygi, F.; Hamann, D. R.; Hasnip, P. J.; Holzwarth, N. A. W.; Iuşan, D.; Jochym, D. B.; Jollet, F.; Jones, D.; Kresse, G.; Koepernik, K.; Küçükbenli, E.; Kvashnin, Y. O.; Loch, I. L. M.; Lubeck, S.; Marsman, M.; Marzari, N.; Nitzsche, U.; Nordström, L.; Ozaki, T.; Paulatto, L.; Pickard, C. J.; Poelmans, W.; Probert, M. I. J.; Refson, K.; Richter, M.;

Rignanese, G.-M.; Saha, S.; Scheffler, M.; Schlipf, M.; Schwarz, K.; Sharma, S.; Tavazza, F.; Thunström, P.; Tkatchenko, A.; Torrent, M.; Vanderbilt, D.; van Setten, M. J.; Van Speybroeck, V.; Wills, J. M.; Yates, J. R.; Zhang, G.-X.; Cottenier, S.; Gunsteren, W. F. van; Miller, G.; Vihinen, M.; Ince, D. C.; Hatton, L.; Graham-Cumming, J.; Hohenberg, P.; Kohn, W.; Kohn, W.; Sham, L. J.; Jones, R. O.; Curtarolo, S.; Setyawan, W.; Hart, G. L. W.; Jahnatek, M.; Chepulskii, R. V.; Taylor, R. H.; Wang, S.; Xue, J.; Yang, K.; Levy, O.; Mehl, M. J.; Stokes, H. T.; Demchenko, D. O.; Morgan, D.; Jain, A.; Ong, S. P.; Hautier, G.; Chen, W.; Richards, W. D.; Dacek, S.; Cholia, S.; Gunter, D.; Skinner, D.; Ceder, G.; Persson, K. A.; Fu, C.-C.; Torre, J. D.; Willaime, F.; Bocquet, J.-L.; Barbu, A.; Friák, M.; Hickel, T.; Grabowski, B.; Lymperakis, L.; Udyansky, A.; Dick, A.; Ma, D.; Roters, F.; Zhu, L.-F.; Schlieter, A.; Kühn, U.; Ebrahimi, Z.; Lebensohn, R. A.; Holec, D.; Eckert, J.; Emmerich, H.; Raabe, D.; Neugebauer, J.; Kurth, S.; Perdew, J. P.; Blaha, P.; Staroverov, V. N.; Scuseria, G. E.; Tao, J.; Perdew, J. P.; Haas, P.; Tran, F.; Blaha, P.; Csonka, G. I.; Perdew, J. P.; Ruzsinszky, A.; Philippen, P. H. T.; Lebègue, S.; Paier, J.; Vydrov, O. A.; Ángyán, J. G.; Pernot, P.; Civalleri, B.; Presti, D.; Savin, A.; Curtiss, L. A.; Raghavachari, K.; Redfern, P. C.; Pople, J. A.; Paier, J.; Hirschl, R.; Marsman, M.; Kresse, G.; Zhao, Y.; Truhlar, D. G.; Goerigk, L.; Grimme, S.; Kiejna, A.; Kresse, G.; Rogal, J.; Sarkar, A. De; Reuter, K.; Scheffler, M.; Grabowski, B.; Hickel, T.; Neugebauer, J.; Lejaeghere, K.; Speybroeck, V. Van; Oost, G. Van; Cottenier, S.; Jollet, F.; Torrent, M.; Holzwarth, N.; Küçükbenli, E.; Monni, M.; Adetunji, B. I.; Adebayo, G. A.; Marzari, N.; Gironcoli, S. de; Corso, A. D.; Poncé, S.; Antonius, G.; Boulanger, P.; Cannuccia, E.; Marini, A.; Côté, M.; Gonze, X.; Hamann, D. R.; Schlüter, M.; Chiang, C.; Kleinman, L.; Bylander, D. M.; Vanderbilt, D.; Blöchl, P. E.; Kresse, G.; Joubert, D.; Slater, J. C.; Andersen, O. K.; Sjöstedt, E.; Nordström, L.; Singh, D. J.; Madsen, G. K. H.; Blaha, P.; Schwarz, K.; Sjöstedt, E.; Nordström, L.; Koepernik, K.; Eschrig, H.; Blum, V.; Gehrke, R.; Hanke, F.; Havu, P.; Havu, V.; Ren, X.; Reuter, K.; Scheffler, M.; Perdew, J. P.; Burke, K.; Ernzerhof, M.; Yuan, G.; Gygi, F.; Bahn, S. R.; Jacobsen, K. W.; Pizzi, G.; Cepellotti, A.; Sabatini, R.; Marzari, N.; Kozinsky, B.; Holzapfel, W. B.; Hartwig, M.; Sievers, W.; Grosshans, W. A.; Holzapfel, W. B.; Dyllal, K. G.; Lenthe, E. van; Koelling, D. D.; Harmon, B. N.; Lenthe, E. van; Baerends, E.; Snijders, J.; Lee, I.-H.; Martin, R. M.; Miyake, T.; Ogitsu, T.; Tsuneyuki, S.; Windl, W.; Bunea, M. M.; Stumpf, R.; Dunham, S. T.; Masquelier, M. P.; Vitos, L.; Johansson, B.; Kollár, J.; Skriver, H.; Miotto, R.; Srivastava, G. P.; Ferraz, A. C.; Ramos, L. E.; Teles, L. K.; Scalfaro, L. M. R.; Castineira, J. L. P.; Rosa, A. L.; Leite, J. R.; Assali, L. V. C.; Machado, W. V. M.; Justo, J. F.; Heyd, J.; Peralta, J. E.; Scuseria, G. E.; Martin, R. L.; Paier, J.; Marsman, M.; Hummer, K.; Kresse, G.; Gerber, I. C.; Angyán, J. G.; Tran, F.; Laskowski, R.; Blaha, P.; Schwarz, K.; Birch, F.; Gulans, A.; Kontur, S.; Meisenbichler, C.; Nabok, D.; Pavone, P.; Rigamonti, S.; Sagmeister, S.; Werner, U.; Draxl, C.; Zhang, I. Y.; Ren, X.; Rinke, P.; Blum, V.; Scheffler, M.; Lehmann, G.; Taut, M.; Froyen, S.; Gonze, X.; Beuken, J.-M.; Caracas, R.; Detraux, F.; Fuchs, M.; Rignanese, G.-M.; Sindic, L.; Verstraete, M.; Zerah, G.; Jollet, F.; Torrent, M.; Roy, A.; Mikami, M.; Ghosez, P.; Raty, J.-Y.; Allan, D. C.; Gonze, X.; Amadon, B.; Anglade, P.-M.; Beuken, J.-M.; Bottin, F.; Boulanger, P.; Bruneval, F.; Caliste, D.; Caracas, R.; Côté, M.; Deutsch, T.; Genovese, L.; Ghosez, P.; Giantomassi, M.; Goedecker, S.; Hamann, D. R.; Hermet, P.; Jollet, F.; Jomard, G.; Leroux, S.; Mancini, M.; Mazevet, S.; Oliveira, M. J. T.; Onida, G.; Pouillon, Y.; Rangel, T.; Rignanese, G.-M.; Sangalli, D.; Shaltaf, R.; Torrent, M.; Verstraete, M. J.; Zerah, G.; Zwanziger, J. W.; Torrent, M.; Jollet, F.; Bottin, F.; Zérah, G.; Gonze, X.;

- Garrity, K. F.; Bennett, J. W.; Rabe, K. M.; Vanderbilt, D.; Mortensen, J. J.; Hansen, L. B.; Jacobsen, K. W.; Enkovaara, J.; Rostgaard, C.; Mortensen, J. J.; Chen, J.; Duřak, M.; Ferrighi, L.; Gavnholt, J.; Glinsvad, C.; Haikola, V.; Hansen, H. A.; Kristoffersen, H. H.; Kuisma, M.; Larsen, A. H.; Lehtovaara, L.; Ljungberg, M.; Lopez-Acevedo, O.; Moses, P. G.; Ojanen, J.; Olsen, T.; Petzold, V.; Romero, N. A.; Stausholm-Møller, J.; Strange, M.; Tritsarlis, G. A.; Vanin, M.; Walter, M.; Hammer, B.; Häkkinen, H.; Madsen, G. K.; Nieminen, R. M.; Nørskov, J. K.; Puska, M.; Rantala, T. T.; Schiøtz, J.; Thygesen, K. S.; Jacobsen, K. W.; Giannozzi, P.; Baroni, S.; Bonini, N.; Calandra, M.; Car, R.; Cavazzoni, C.; Ceresoli, D.; Chiarotti, G. L.; Cococcioni, M.; Dabo, I.; Corso, A. D.; Gironcoli, S. de; Fabris, S.; Fratesi, G.; Gebauer, R.; Gerstmann, U.; Gougoussis, C.; Kokalj, A.; Lazzeri, M.; Martin-Samos, L.; Marzari, N.; Mauri, F.; Mazzarello, R.; Paolini, S.; Pasquarello, A.; Paulatto, L.; Sbraccia, C.; Scandolo, S.; Sclauzero, G.; Seitsonen, A. P.; Smogunov, A.; Umari, P.; Wentzcovitch, R. M.; Corso, A. D.; Marzari, N.; Vanderbilt, D.; Vita, A. De; Payne, M. C.; Corso, A. D.; Kresse, G.; Furthmüller, J.; Hafner, J.; Blöchl, P. E.; Jepsen, O.; Andersen, O. K.; Clark, S. J.; Segall, M. D.; Pickard, C. J.; Hasnip, P. J.; Probert, M. I. J.; Refson, K.; Payne, M. C.; Hamann, D. R.; Schlipf, M.; Gygi, F.; Fuchs, M.; Scheffler, M.; Goedecker, S.; Teter, M.; Hutter, J.; Hartwigsen, C.; Goedecker, S.; Hutter, J.; Krack, M.; Genovese, L.; Neelov, A.; Goedecker, S.; Deutsch, T.; Ghasemi, S. A.; Willand, A.; Caliste, D.; Zilberberg, O.; Rayson, M.; Bergman, A.; Schneider, R.; Mohr, S.; Ratcliff, L. E.; Boulanger, P.; Genovese, L.; Caliste, D.; Deutsch, T.; Goedecker, S.; Willand, A.; Kvashnin, Y. O.; Genovese, L.; Vázquez-Mayagoitia, Á.; Deb, A. K.; Sadeghi, A.; Deutsch, T.; Goedecker, S.; Ozaki, T.; Ozaki, T.; Kino, H.; Ozaki, T.; Kino, H.; Morrison, I.; Bylander, D. M.; Kleinman, L.; Hamann, D. R. Reproducibility in Density Functional Theory Calculations of Solids. *Science* (80-. ). **2016**, *351* (6280), 1415.
- (151) Butkovich, T. R. Thermal Expansion of Ice. *J. Appl. Phys.* **1959**, *30* (3), 350–353.
- (152) Bauer, J. D.; Haussühl, E.; Winkler, B.; Arbeck, D.; Milman, V.; Robertson, S. Elastic Properties, Thermal Expansion, and Polymorphism of Acetylsalicylic Acid. *Cryst. Growth Des.* **2010**, *10*, 3132–3140.
- (153) Krishnan, R. S.; Srinivasan, R.; Devanarayanan, S. Copyright. In *Thermal Expansion of Crystals*; Elsevier: Oxford, 1979; p iv.
- (154) Jones, P. G. Crystal Structure Determination: A Critical View. *Chem. Soc. Rev.* **1984**, *13* (2), 157–172.
- (155) Evans, J. S. O.; David, W. I. F.; Sleight, A. W. Structural Investigation of the Negative-Thermal-Expansion Material ZrW<sub>2</sub>O<sub>8</sub>. *Acta Crystallogr. Sect. B Struct. Sci.* **1999**, *55* (3), 333–340.
- (156) Spek, A. L. Structure Validation in Chemical Crystallography. *Acta Crystallogr. Sect. D Biol. Crystallogr.* **2009**, *65* (2), 148–155.
- (157) Schomaker, V.; Trueblood, K. N. On the Rigid-Body Motion of Molecules in Crystals. *Acta Crystallogr. Sect. B Struct. Crystallogr. Cryst. Chem.* **1968**, *24* (1), 63–76.

- (158) Evans, J. S. O.; Mary, T. A.; Vogt, T.; Subramanian, M. A.; Sleight, A. W. Negative Thermal Expansion in ZrW<sub>2</sub>O<sub>8</sub> and HfW<sub>2</sub>O<sub>8</sub>. *Chem. Mater.* **1996**, *8* (12), 2809–2823.
- (159) Dominiak, P. M.; Coppens, P. Finding Optimal Radial-Function Parameters for S Atoms in the Hansen-Coppens Multipole Model through Refinement of Theoretical Densities. *Acta Crystallogr. Sect. A Found. Crystallogr.* **2006**, *62* (3), 224–227.
- (160) Khaliullin, R. Z.; Eshet, H.; Kuhne, T. D.; Behler, J.; Parrinello, M. Nucleation Mechanism for the Direct Graphite-to-Diamond Phase Transition. *Nat. Mater.* **2011**, *10* (9), 693–697.
- (161) Zhang, W.; Peng, Y.; Liu, Z. Molecular Dynamics Simulations of the Melting Curve of NiAl Alloy under Pressure. *AIP Adv.* **2014**, *4* (5).
- (162) Alfassi, Z. B.; Groppi, F.; Bonardi, M. L.; Goeij, J. J. M. de. On the “Artificial” Nature of Tc and the “Carrier-Free” Nature of <sup>99m</sup>Tc from <sup>99</sup>Mo/<sup>99m</sup>Tc Generators. *Appl. Radiat. Isot.* **2005**, *63* (1), 37–40.
- (163) Shen, G.; Mao, H. K. High-Pressure Studies with x-Rays Using Diamond Anvil Cells. *Reports Prog. Phys.* **2017**, *80* (1).
- (164) Weck, P. F.; Kim, E. Thermodynamics of Technetium: Reconciling Theory and Experiment Using Density Functional Perturbation Analysis. *Dalt. Trans.* **2015**, *44* (28), 12735–12742.
- (165) Smith Jr, W. T.; Line Jr, L. E.; Bell, W. A. The Vapor Pressures of Rhenium Heptoxide and Perrhenic Acid. *J. Am. Chem. Soc.* **1952**, *74* (19), 4964.
- (166) Nikol'skii, A. B. Vapor Pressure of Ruthenium Tetroxide. *Zhurnal Neorg. Khimii* **1963**, *8*, 1045–1048.
- (167) Selig, H.; Malm, J. G. The Preparation and Properties of Pertechnetyl Fluoride, TcO<sub>3</sub>F. *J. Inorg. Nucl. Chem.* **1963**, *25*, 349.
- (168) Engelbrecht, A.; Grosse, A. V. Fluorides of Permanganic and Perrhenic Acids. **1953**, *76*, 2042.
- (169) Selig, H.; Malm, J. G. The Vapour-Pressure and Transition Points of TcF<sub>6</sub>. *J. Inorg. Nucl. Chem.* **1962**, *24*, 641.
- (170) Malm, J. G.; Selig, H. The Vapour-Pressures and Other Properties of ReF<sub>6</sub> and ReF<sub>7</sub>. *J. Inorg. Nucl. Chem.* **1961**, *20* (3–4), 189–197.
- (171) Bartlett, N.; Levchuk, L. E. Proceedings of the Chemical Society. November 1963. *Proc. Chem. Soc.* **1963**, No. November, 325.
- (172) Bartlett, N.; Jha, N. K. The Preparation and Some Physical Properties of Osmium Oxide Pentafluoride, OsOF<sub>5</sub>. *J. Chem. Soc. A Inorganic, Phys. Theor.* **1968**, *2*, 536.

- (173) Miller, F. A.; Carlson, G. L. Vibrational Spectra of  $\text{ReO}_3\text{Cl}$  and  $\text{ReO}_3\text{Br}$ . *Spectrochim. Acta* **1960**, *16*, 1148–1154.
- (174) Edwards, A. J. Crystal Structure of Rhenium Oxide Tetrachloride. *J. Chem. Soc. Dalt. Trans.* **1972**, 582.
- (175) Siegel, S.; Northrop, D. A. X-Ray Diffraction Studies of Some Transition Metal Hexafluorides. *Inorg. Chem.* **1966**, *5* (12), 2187-.
- (176) Cady, G. H.; Hargreaves, G. B. The Vapour Pressures of Some Heavy Transition-Metal Hexafluorides. *J. Chem. Soc.* **1961**, 1563.
- (177) Perry, D. L. *Handbook of Inorganic Compounds*; CRC Press, 1995.
- (178) Schack, C. J.; Pilipovich, D.; Cohz, S. N.; Sheehan, D. F. Mass Spectra and Sublimation Pressures of  $\text{IF}_7$  and  $\text{IOF}_5$ . **1968**, *72* (2), 4697.
- (179) Nikol'skii, A. B. Existence of Two Modifications of Ruthenium Tetroxide. *Zhurnal Neorg. Khimii* **1963**, *8* (5), 1289.
- (180) Leblond, N.; Schrobilgen, G. J. Synthesis of a New Volatile Technetium(VI) Oxofluoride,  $\text{TcOF}_5$ . *Chem. Commun.* **1996**, *6*, 2479–2480.
- (181) Cady, G. H.; Hargreaves, G. B. Vapour Pressures of Some Fluorides and Oxyfluorides of Molybdenum, Tungsten, Rhenium, and Osmium. *J. Chem. Soc.* **1961**, *0*, 1568.

# Curriculum Vita

**Daniel Steven Mast**

Email: [Daniel.Mast@unlv.edu](mailto:Daniel.Mast@unlv.edu)

## **EDUCATION**

---

### **University of Nevada, Las Vegas, Las Vegas, NV**

Degree: *Doctor of Philosophy (Ph.D.) in Radiochemistry*; May 2018 (anticipated)

Specialized Coursework in X-ray and Neutron Crystallography

Dissertation Committee Chair: Paul M. Forster, PhD,

Dissertation Committee: Frederic Poineau, PhD, Dan Kourey, PhD, Pamela Burnley, PhD, Barbara Lavina, PhD

### **Saint Martin's University, Lacey, WA**

Degree: *Bachelor of Arts (B.A.) in Mathematics*; May 2013

Degree: *Bachelor of Science (B.S.) in Chemistry*; May 2013

Summa Cum Laude

Mentor: Arwyn Smalley, PhD

## **ACADEMIC POSITIONS**

---

2013 – Present      Doctoral Graduate Research and Teaching Assistant,  
Department of Chemistry and Biochemistry, University of Nevada, Las Vegas, NV  
Advisor: Dr. Paul Forster (2013 – Present)

## **RELEVANT PROFESSIONAL EXPERIENCES**

---

2016                  Graduate Student Intern, Idaho National Laboratory, Idaho Falls, ID

2014                  Condensed Matter and Materials Division Graduate Intern, Lawrence Livermore National  
Laboratory, Livermore, CA



2012	Peer Mentor for First Year Seminar, Saint Martin's University, Lacey, WA Co-taught with Dr. George Christoph
2012 – 2013	Lead Tutor, Academic Success Center, Saint Martin's University, Lacey, WA
2012	Assistant Aquatics Director, Camp Merriweather, Cape Lookout, OR
2011 – 2013	Student Assistant, Disability Support Services, Saint Martin's University, Lacey, WA
2011 – 2013	Laboratory Assistant and Teaching Assistant, Department of Chemistry, Saint Martin's University, Lacey, WA
2010 – 2013	Math/Physics/Chemistry Tutor, Academic Success Center, Saint Martin's University, Lacey, WA
2009– 2013	Assistant Swim Coach, YMCA, Olympia, WA

## TEACHING

## EXPERIENCE

### University of Nevada, Las Vegas, Department of Chemistry & Biochemistry

CHEM 122L General Chemistry Lab II (Spring 2017)

CHEM 312 Introduction to Radiochemistry (Summer 2015)

### Saint Martin's University

UNI 101 First Year Seminar, Cotaught as Peer Mentor (Fall 2012)

## FUNDING

### Funded Grant Proposals

1. **Mast, D.S.**, (2014-17) Nuclear Energy Universities Program-Nuclear Engineering Fellowship \$155,000  
**Role: Principle Investigator**
2. **Mast, D.S.**, (2013-15) Malcolm F. Nicol's Graduate Scholars Fellowship \$70,000 **Role: Principle Investigator**
3. **Mast, D.S.**, (2016) Student Travel Grant, American Crystallographic Society \$599.00, **Role: Presenter.**
4. **Mast, D.S.**, (Fall 2016) Student Travel Scholarship, UNLV GPSA \$950.00, **Role: Presenter.**
5. **Mast, D.S.**, (Fall 2015) Student Travel Scholarship, UNLV GPSA \$930.00, **Role: Principal Investigator.**
6. **Mast, D.S.**, (2015) Student Travel Grant, International Union of Crystallography \$600.00, **Role: Presenter.**
7. **Mast, D.S.**, (Spring 2015) Student Travel Scholarship, UNLV GPSA \$950.00, **Role: Presenter.**

### Grant Proposals Submitted

1. **Mast, D.S.**, (2018). Summer Doctoral Research Fellowship, UNLV Graduate College, University of Nevada, Las Vegas, \$7,000. **Role: Principle Investigator**

## RESEARCH

---

### Published or In Press Manuscripts

1. **Mast, D.S.**, Kim, E. Siska, E., Poineau, F., Czerwinski, K.R., Lavina, B., and Forster, P. M. Equation of state for technetium from X-ray diffraction and first-principle calculations, *Journal of Physics and Chemistry of Solids*, 95 August 2016, 6-11, ISSN 0022-3697, <http://dx.doi.org/10.1016/j.jpcs.2016.03.007>.
2. Shrestha, K., Antonio, D., Jaime, M., Harrison, N., **Mast, D. S.**, Safarik, D., Durakiewicz, T., Griveau J.-C., and Gofryk, K., Tricritical point from high-field magnetoelastic and metamagnetic effects in UN, *Scientific Reports* 2017
3. Childs, B.C., Braband, H., Lawler, K.V., **Mast, D.S.**, Bigler, L., Stalder, U., Forster, P.M., Czerwinski, K.R., Alberto, R., Sattelberger, A.P., and Poineau, F., Ditechnetium Heptoxide Revisited: Solid-State, Gas-Phase, and Theoretical Studies. *Inorganic Chemistry* 2016 55 (20), 10445-10452 DOI: 10.1021/acs.inorgchem.6b01683
1. Lawler, K.V., Childs, B.C., **Mast, D.S.**, Czerwinski, K.R., Sattelberger, A.P., Poineau, F., and Forster, P.M., Electronic and Molecular Structure of  $M_2O_7$  ( $M = Mn, Tc, Re$ ). *Inorganic Chemistry* 2017 56 (5), 2448-2458 DOI: 10.1021/acs.inorgchem.6b02503
2. Childs, B.C., Lawler, K.V., Henrik, B., **Mast, D.S.**, Bigler, L., Stalder, U., Peterson, D.R., Jansen, A., Forster, P.M., Czerwinski, K.R., Alberto, R., Sattelberger, A.P., and Poineau, F. The Nature of the Technetium Species Formed During the Oxidation of Technetium Dioxide with Oxygen and Water. *Eur. J. Inorg. Chem.* 2018, 1137–1144 DOI: 10.1002/ejic.201701199

### Manuscripts in Preparation

1. **Mast, D.S.**, Lawler, K.V., Childs, B.C., Czerwinski, K.R., Sattelberger, A.P., Poineau, F., and Forster, P.M. (In preparation) An Atomistic Understanding of the Unexpectedly Low Volatility of the Molecular Oxide  $Tc_2O_7$  Target Journal: *Inorganic Chemistry*
2. **Mast, D.S.**, Lavina, B., Siska, E.M., Lawler, K.V., Poineau, F., and Forster, P.M. (In preparation) Equation of state for technetium metal up to 1.5 Mbar, Target Journal:
3. **Mast, D.S.**, Lapidus, S., Lavina, B., Siska, E.M., Lawler, K.V., Poineau, F., and Forster, P.M. (In preparation) Thermal expansion of technetium metal, Target Journal: *Journal of Nuclear Materials*
4. **Mast, D.S.**, Lavina, B., Siska, E.M., Lawler, K.V., and Forster, P.M. (In preparation) Discovery of high pressure phase of  $MoO_2$ , Target Journal:
5. **Mast, D.S.**, Lavina, B., Siska, E.M., Lawler, K.V., Poineau, F., and Forster, P.M. (In preparation) High pressure behavior of transition metal oxides,  $MoO_2$ ,  $ReO_2$ , and  $TcO_2$ , Target Journal:

### Invited Presentations

1. **Mast, D.S.**, Lawler, K.V., Childs, B.C., Czerwinski K.R., Sattelberger, A.P., Poineau, F., and Forster, P.M. Thermal motion in technetium heptoxide, American Nuclear Society Winter Meeting, Las Vegas, NV November 2016

### Conference Presentations

1. **Mast, D.S.**, Lawler, K.V., Childs, B.C., Czerwinski K.R., Sattelberger, A.P., Poineau, F., and Forster, P.M. (2017) Thermal Motion in ditechnetium heptoxide. Oral Presentation, 67<sup>th</sup> American Crystallographic Association Annual Meeting, New Orleans, LA, May 2017

2. **Mast, D. S.**, Kim, E., Siska, E., Poineau, F., Czerwinski, K.R., Lavina, B., Forster, P.M. (2016) Equation of state for technetium up to 1.5 Mbar. Oral Presentation, American Nuclear Society Winter Meeting, Las Vegas, NV, November 2016
3. **Mast, D.S.**, Lavina, B., Siska, E., Forster, P.M. (2016) Pressure-Induced Phase Transition in the Mo<sub>2</sub> system, M = Re, Mo, Tc. Oral Presentation, 54<sup>th</sup> European High-Pressure Research Group International Meeting on High Pressure Science and Technology, Bayreuth, Germany, September 2016
4. **Mast, D.S.**, Childs, B.C., Lawler, K.V., Braband, H., Poineau, F., Czerwinski, K.R., Sattelberger, A.P., Forster, P.M. (2016) Revisiting the structure and synthesis of technetium heptoxide. Poster Presentation, 30<sup>th</sup> European Crystallographic Meeting, Basel, Switzerland, August 2016
5. **Mast, D.S.**, Shrestha, K., Antonio, D., Gofryk, K. (2016) Heat Capacity of Uranium Fuels: UO<sub>2</sub> and UN. Poster Presentation, Intern Expo, Idaho National Laboratory, Idaho Falls, ID, August 2016
6. **Mast, D.S.**, Lavina, B., Siska, E., Forster, P.M. (2016) Pressure-Induced Phase Transition in the Mo<sub>2</sub> system, M = Re, Mo, Tc. Oral Presentation, 66<sup>th</sup> American Crystallographic Association Annual Meeting, Denver, CO, July 2016
7. **Mast, D.S.**, Childs, B.C., Lawler, K.V., Braband, H., Poineau, F., Czerwinski, K.R., Sattelberger, A.P., Forster, P.M. (2016) Revisiting the structure and synthesis of technetium heptoxide. Poster Presentation, Stewardship Science Academic Programs Symposium, National Nuclear Security Administration, Bethesda, MD, February 2016
8. **Mast, D.S.**, Kim, E., Siska, E.M., Poineau, F., Czerwinski, K.R., Lavina, B., Forster, P.M. (2015) Equation of State for Technetium. Poster Presentation, High Pressure Workshop, International Union of Crystallography, Brazilian Synchrotron Light Laboratory, Center of Research in Energy and Materials, Campinas, Brazil, September 2015
9. **Mast, D. S.**, Kim, E., Siska, E., Poineau, F., Czerwinski, K.R., Lavina, B., Forster, P.M. (2015) Powder Diffraction of Technetium at Non-Ambient Conditions. Oral Presentation, 65<sup>th</sup> American Crystallographic Association Annual Meeting, Philadelphia, PA, July 2015
10. **Mast, D. S.**, Siska, E., Lavina, B., Poineau, F., Czerwinski, K.R., Forster, P.M. (2014) Equation of State for Technetium by X-ray Diffraction. Poster Presentation, 8<sup>th</sup> International Symposium on Technetium and Rhenium: Science and Utilization, Pornichet-La Baule, France, October 2014
11. **Mast, D. S.**, Siska, E., Lavina, B., Cynn, H., Poineau, F., Evans, W.J., Czerwinski, K.R., Forster, P.M. (2014) MoO<sub>2</sub>-type transition metal oxides under extreme conditions. Poster Presentation, 2<sup>nd</sup> Joint Conference of the Italian Crystallographic Association and Italian Synchrotron Radiation Society, Florence, Italy, September 2014
12. **Mast, D. S.**, Siska, E., Lavina, B., Cynn, H., Poineau, F., Evans, W.J., Czerwinski, K.R., Forster, P.M. (2014) MoO<sub>2</sub>-type transition metal oxides under extreme conditions. Poster Presentation, 52<sup>nd</sup> European High-Pressure Research Group International Meeting, Lyon, France, September 2014
13. **Mast, D.S.**, Lavina, B., Cynn, H., Evans, W.J., Forster, P.M. (2014) High Pressure Investigation of transition Metal Oxides. Poster Presentation, Annual Summer Student Symposium, Lawrence Livermore National Laboratory, Livermore, CA, August 2014
14. **Mast, D. S.**, Siska, E., Lavina, B., Poineau, F., Czerwinski, K.R., Forster, P.M. (2014) Equation of State for Technetium by X-ray Diffraction. Research at High Pressure, Poster Presentation, Gordon Research Conference/Seminar, Biddeford, ME, July 2014

15. **Mast, D. S.**, Siska, E., Lavina, B., Poineau, F., Czerwinski, K.R., Forster, P.M. (2014) Equation of State for Technetium by X-ray Diffraction. Poster Presentation, School of Synchrotron Crystallography, ChemMatCars, Advanced Photon Source, Argonne National Laboratory, Argonne, IL, December 2014
16. **Mast, D.S.**, Kim, E. Siska, E., Poineau, F., Czerwinski, K.R., Lavina, B., and Forster, P. M. (2014) First Equation of State for Technetium by X-ray Diffraction and DFT. Poster Presentation International School on Fundamental Crystallography, International Union of Crystallography, Universidad Nacional de La Plata, Argentina, May 2014
17. **Mast, D.S.**, Smalley, A., (2013) Speciation of Arsenic in well-water. Poster Presentation, American Chemical Society, Northwestern Regional Undergraduate Research Symposium, Seattle Pacific University, Seattle, WA February **2013**
18. **Mast, D.S.**, Smalley, A., (2013) Speciation of Arsenic in well-water. Poster Presentation, 245<sup>th</sup> American Chemical Society Spring Meeting, New Orleans, LA, March 2013

#### University Conferences

1. **Mast, D.S.**, Lawler, K.V., Childs, B.C., Czerwinski K.R., Sattelberger, A.P., Poineau, F., and Forster, P.M. (2017) Thermal Motion in  $Tc_2O_7$ . Poster Presentation, Extreme Crystals Weekend, High Pressure Science and Engineering Center, University of Nevada, Las Vegas, Las Vegas, NV, October 2017.
2. **Mast, D.S.**, Lawler, K.V., Childs, B.C., Czerwinski K.R., Sattelberger, A.P., Poineau, F., and Forster, P.M. (2017) Negative Thermal Bond Expansion of a Molecular Solid  $Tc_2O_7$ . Oral presentation, Annual Graduate College & GPSA Research Forum, University of Nevada, Las Vegas, Las Vegas, NV, April 2017
3. **Mast, D.S.**, Lawler, K.V., Childs, B.C., Czerwinski K.R., Sattelberger, A.P., Poineau, F., and Forster, P.M. (2017) Thermal motion in technetium heptoxide. Poster Presentation, Stewardship Science Academic Programs Annual Review Symposium, National Nuclear Security Administration, Office of Research, Development, Test and Evaluation, Naperville, IL, March 2017
4. **Mast, D. S.**, Siska, E., Lavina, B., Cynn, H., Poineau, F., Evans, W.J., Czerwinski, K.R., Forster, P.M. (2016) High Pressure Phase Diagram of Molybdenum Dioxide. Poster presentation, Annual Graduate College & GPSA Research Forum, University of Nevada, Las Vegas, Las Vegas, NV, March 2016
5. **Mast, D.S.**, Cynn, H. Siska, E., Poineau, F., Evans, W.J., Czerwinski, K.R., Lavina, B., and Forster, P. M. (2016) Crystallography of Technetium Metal Non-Ambient Conditions. Poster Presentation, Extreme Crystals Weekend, High Pressure Science and Engineering Center, University of Nevada, Las Vegas, Las Vegas, NV, October 2016.
6. **Mast, D.S.**, Cynn, H. Siska, E., Poineau, F., Evans, W.J., Czerwinski, K.R., Lavina, B., and Forster, P. M. (2016) High Pressure Equation of State for Technetium Metal. Oral Presentation, Extreme Crystals weekend, High Pressure Science and Engineering Center, University of Nevada, Las Vegas, Las Vegas, NV, April 2016.
7. **Mast, D.S.** (2016). Crystallography: The science of structures. Oral Presentation, Inspiration, Innovation, Impact: A Celebration of Graduate Student Research, Graduate College, University of Nevada, Las Vegas, Las Vegas, NV, March 2016
8. **Mast, D.S.**, Cynn, H. Siska, E., Poineau, F., Evans, W.J., Czerwinski, K.R., Lavina, B., and Forster, P. M. (2016) High Pressure Behavior of Technetium Compounds. Poster Presentation, Stewardship Science Academic Programs Annual Review Symposium, National Nuclear Security Administration, Office of Research, Development, Test and Evaluation, Bethesda, MD, February 2016
9. **Mast, D.S.**, Lawler, K.V., Childs, B.C., Czerwinski K.R., Sattelberger, A.P., Poineau, F., and Forster, P.M. (2015) What happens when you squeeze it? High Pressure behavior of Technetium Oxides. Podium

Presentation, Grad Rebel Slam: 3-Minute Thesis Competition, University of Nevada, Las Vegas, Las Vegas, NV, November 2016. Finalist

10. **Mast, D.S.**, Kim, E. Siska, E., Poineau, F., Czerwinski, K.R., Lavina, B., and Forster, P. M. (2015) High Pressure Equation of State for Technetium Metal. Poster presentation, Annual Graduate College & GPSA Research Forum, University of Nevada, Las Vegas, Las Vegas, NV, March 2015
11. **Mast, D. S.**, Siska, E., Lavina, B., Poineau, F., Evans, W.J., Forster, P.M. (2015) High Pressure Phase Diagram of Transition Metal Oxides. Oral Presentation, National Nuclear Security Administration Annual Review, High Pressure Science and Engineering Center, University of Nevada, Las Vegas, Las Vegas, NV, February 2015
12. **Mast, D. S.**, Siska, E., Lavina, B., Cynn, H., Poineau, F., Evans, W.J., Czerwinski, K.R., Forster, P.M. (2014) High Pressure Behavior of Technetium Compounds, Poster Presentation, National Nuclear Security Administration Annual Review, High Pressure Science and Engineering Center, University of Nevada, Las Vegas, Las Vegas, NV, January 2014
13. **Mast, D.S.**, Kim, E. Siska, E., Poineau, F., Czerwinski, K.R., Lavina, B., and Forster, P.M. (2014) What happens when you squeeze it? High Pressure behavior of Technetium Metal. Podium Presentation, Grad Rebel Slam: 3-Minute Thesis Competition, University of Nevada, Las Vegas, Las Vegas, NV, November 2015. Finalist

#### General User Proposals

1. **Mast, D.S.**, Lavina, B., Forster, P.M. (2015-1) Pressure induced phase transitions in transition metal oxides. 9 shifts, 12.2.2, Advanced Light Source, Lawrence Berkley National Laboratory, GUP ID: 07000
2. **Mast, D.S.**, Siska, E.M., Forster, P.M., (2014-3) Thermal expansion of technetium metal from 100 – 450 K, 6 shifts, 11 – BM Advanced Photon Source, Argonne National Laboratory GUP ID: 40660
3. Forster, P.M., Page, K., **Mast, D.S.**, Olds, D. (2015-2) Alteration of cation local structure through gas uptake in zeolites, 6 shifts, BL-1B NOMAD, Spallation Neutron Source, Oak Ridge National Laboratory, IPTS-14546

#### Member User Proposals

1. Lavina, B., Bai, L., **Mast, D.S.**, Kothapalli, K. (2013-2) Single Crystal and powder compressibility of  $\text{Fe}_4\text{O}_5$ ,  $\text{ReCl}_3$ ,  $\text{ReBr}_3$ ,  $\text{ReI}_3$ . 6 shifts, 16-IDB, Advanced Photon Source, Argonne National Laboratory, Experiment ID: 105950
2. Lavina, B., **Mast, D.S.**, Siska, E.M., Forster, P.M. (2013-3) Compressibility of Tc metal and sodalite gas insertion. 6 shifts, 16-IDB, Advanced Photon Source, Argonne National Laboratory, Experiment ID 110584
3. Lavina, B., **Mast, D.S.**, Wang, Y., Siska, E.M., Forster, P.M. (2014-1) Tc metal compression. 4 shifts, 16-BMD, Advanced Photon Source, Argonne National Laboratory, Experiment ID: 113507
4. Cynn, H., **Mast, D.S.**, Evans, W.J. (2014-2) High pressure and high temperature X-ray diffraction of  $\text{ReO}_2$  and  $\text{MoO}_2$ . 9 shifts, 16-BMD, Advanced Photon Source, Argonne National Laboratory, Experiment ID: 118229
5. Klepseis, J.H., **Mast, D.S.**, Park, C., Baer, B., Evans, W.J., Lipp, M., Cynn, H. (2014-2) EOS studies of 5f metal compounds. 9 shifts, 16-BMD, Advanced Photon Source, Argonne National Laboratory, Experiment ID:119587

6. Lavina, B., **Mast, D.S.**, Evans, W.J., Forster, P.M., Cynn, H. (2014-2) EOS studies of transition metal compounds. 7 shifts, 16-IDB, Advanced Photon Source, Argonne National Laboratory, Experiment ID: 119739
7. Lavina, B., **Mast, D.S.**, Forster, P.M. (2015-1) EOS studies of transition metal compounds. 6 shifts, 16-IDB, Advanced Photon Source, Argonne National Laboratory, Experiment ID: 127977
8. Lavina, B., **Mast, D.S.**, Rowland, R., Forster, P.M. (2015-2) EOS studies of transition metal compounds. 6 shifts, 16-BMD, Advanced Photon Source, Argonne National Laboratory, Experiment ID: 128004
9. (2015-3) Crystallographic analysis of high PT phases obtained in the LH DAC, Single crystal and powder diffraction. 6 shifts, 16-IDB, Advanced Photon Source, Argonne National Laboratory, Experiment ID: 139389
10. Lavina, B., **Mast, D.S.**, Siska, E.M. Low temperature compression of uranium compounds. (2016-1) 6 shifts, 16-IDB, Advanced Photon Source, Argonne National Laboratory, Experiment ID:
11. Lavina, B., **Mast, D.S.**, Siska, E.M., Lee, S., Krzysztow, G., Antonio, D. (2016-3) Compressibility of  $TcO_2$ ,  $MBe_{13}$  ( $M = Yb, Ce, La$ ),  $MgFe_2$ ,  $FeO$  at ambient temperature and high PT behavior of BP and  $Mg_2SiO_4$ . 6 shifts, 16-IDB, Advanced Photon Source, Argonne National Laboratory, Experiment ID: 158869
12. Lavina, B., **Mast, D.S.**, Antonia, D., Gofryk, K. (2016-3) Crystallographic analysis of  $UO_2$ , UN,  $CeBe_{13}$ ,  $YBe_{13}$  at ambient, low temperature, and high pressure in a DAC. 6 shifts, 16-BMD, Advanced Photon Source, Argonne National Laboratory, Experiment ID: 155710

## **SCHOLARLY AWARDS & HONORS**

---

1. Graduate College and Graduate & Professional Student Association Annual Research Forum, Honorable Mention: Negative Thermal Bond Expansion of a Molecular Solid  $Tc_2O_7$  (**Mast**, Lawler, Childs, Czerwinski, Sattelberger, Poineau, and Forster) 2017.
2. Innovations in Fuel Cycle Research Award, 1<sup>st</sup> Place recipient in Nuclear Science and Engineering for the Paper: Equation of state for technetium from X-ray diffraction and first-principle calculations, (**Mast**, Kim, Siska, Poineau, Czerwinski, Lavina, and Forster) 2016
3. Margaret C. Etter Student Lecturer Award, Materials Special Interest Group, American Crystallographic Society, Pressure-Induced Phase Transition in the  $Mo_2$  system,  $M = Re, Mo, Tc$ . (**Mast**, Lavina, Siska, Forster) 2016
4. Margaret C. Etter Student Lecturer Award, Powder Special Interest Group, ACA, Equation of state for technetium from X-ray diffraction and first-principle calculations, (**Mast**, Kim, Siska, Poineau, Czerwinski, Lavina, and Forster) 2015
5. UNLV Radiochemistry Campus Involvement Award 2015
6. American Chemical Society Student Leadership Award, 2012
7. Eagle Scout, Boy Scouts of America, 2008

## **Academic Workshops & Short Courses**

---

1. Modern Methods of Rietveld Refinement for Structural Analysis, Oak Ridge National Laboratory, Oak Ridge, TN 2017

2. High-Pressure Multigrain Crystallography Workshop, High Pressure Collaborative Access Team, Advanced Photon Source, Argonne National Laboratory, Argonne, IL 2016
3. 11<sup>th</sup> LANSCE School on Neutron Scattering, Lujan Center, Los Alamos National Laboratory, Los Alamos, NM 2015
4. High Pressure Workshop, International Union of Crystallography, Brazilian Synchrotron Light Laboratory, Center of Research in Energy and Materials, Campinas, Brazil 2015
5. School of Synchrotron Crystallography, ChemMatCARS, Advanced Photon Source, Argonne National Laboratory, Argonne, IL 2014
6. International School on Fundamental Crystallography, International Union of Crystallography, Universidad Nacional de La Plata, Argentina 2014
7. Paris-Edinburgh Cell Workshop, High Pressure Collaborative Access Team, Advanced Photon Source, Argonne National Laboratory, Argonne, IL 2013
8. Nuclear Chemistry Summer School, American Chemical Society, Brookhaven National Laboratory, Shirley, NY 2012
9. National Leadership Institute, American Chemical Society, Houston, TX 2012

## **PROFESSIONAL SERVICE**

---

### Department, College/School, University

2018	Panelist, New Graduate Student Orientation
2016	Panelist, GPSA/Graduate College workshop on 3MT Presentation, UNLV
2016	Panelist, GPSA/Graduate College workshop on Obtaining External Funding, UNLV
2015 – 2018	Ambassador, Graduate College, UNLV
2015	Panelist, GPSA/Graduate College workshop on Grad School Life, UNLV
2014 – 2018	Presenter/Organizer, Nuclear Science Workshop, American Nuclear Society, UNLV
2012 – 2013	Presenter, Academic Success Workshop: How to study for math test, SMU
2012 – 2013	Presenter, Academic Success Workshop: Utilizing Graphing Calculators, SMU

### Non-University

2017	Volunteer, Clean Energy Project Summit
2017	Session Chair, American Crystallographic Association Annual Meeting
2015 – Present	Manuscript Reviewer, Dalton Transactions, Royal Society of Chemistry
2012 – 2013	Presenter, Fusion Science Theater, American Chemical Society
2011 – 2013	President (12-13), Vice President (11-12), American Chemical Society

2012 Judge, Science Fair, Aspire Middle School, American Chemical Society

### Professional Memberships

---

2010 – Present American Chemical Society, Student Member

2013 – Present American Crystallographic Association, Student Member

2013 – Present International Union of Crystallography, Student Member

2013 – Present American Nuclear Society, Student Member

### Certifications

---

2013 – Present Radiation Worker II, Department of Energy

2017 ASHI CPR, AED, and Basic First Aid

2017 ASHI Emergency Oxygen Administration

### References

---

Dr. Paul Forster, Associate Professor  
Department of Chemistry and Biochemistry  
University of Nevada, Las Vegas  
4505 South Maryland Parkway, Box 454003  
Las Vegas, NV 89151-4003  
Office: (702) 895-3753  
[Paul.forster@unlv.edu](mailto:Paul.forster@unlv.edu)

Dr. Kate Korgan, Dean of the Graduate College  
University of Nevada, Las Vegas  
4505 South Maryland Parkway, Box 454003  
Las Vegas, NV 89151-1017  
Office: (702) 895-0446  
[Kate.korgan@unlv.edu](mailto:Kate.korgan@unlv.edu)

Dr. Kenneth Czerwinski, Professor  
Department of Chemistry and Biochemistry  
University of Nevada, Las Vegas  
4505 South Maryland Parkway, Box 454003  
Las Vegas, NV 89151-4003  
Cell: (702) 281-0465  
[ken.czerwinski@unlv.edu](mailto:ken.czerwinski@unlv.edu)



